Water-Borne Geophysics for Murray River Salt-Load Detection

Brian Edward Barrett

Department of Geology and Geophysics
Adelaide University, South Australia

February, 2003

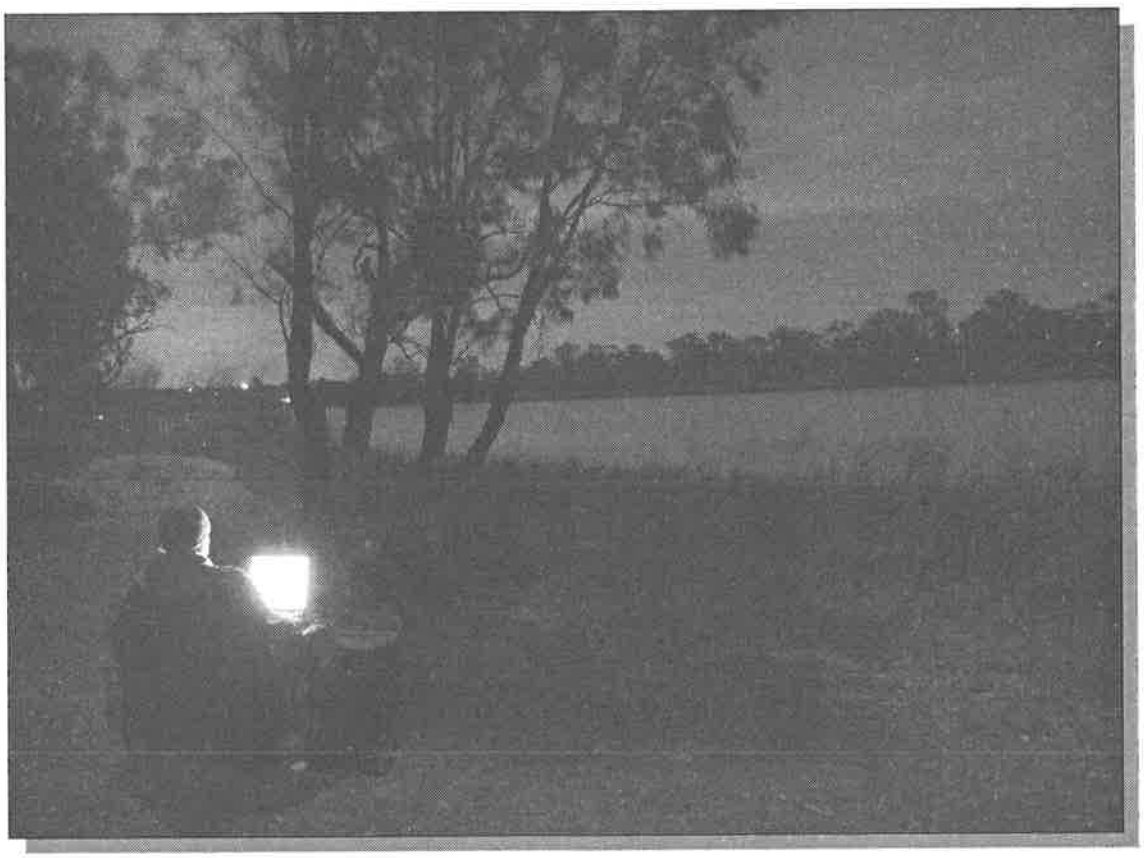

Above: The author at work on the Murray River

Contents

List of Figures

List of Tables

Abstract

Towed DC Resistivity and Transient Electromagnetic (TEM) arrays have been trialed for suitability in monitoring salt-loads on the Murray River at Waikerie, South Australia. A fast and effective technique is required to locate small-scale salt-load hot-spots and to monitor the efficiency of mitigation programs such as Salt Interception Schemes. Geophysical techniques will achieve this by imaging the resistivity structure of the alluvial sediments beneath the Murray River. The TEM array is an aquatic deployment of the Zonge Engineering NanoTEM system (a fast time-sampling method), and was found to be logistically simpler to tow than the DC Resistivity array.

The survey area consisted of two river stretches; one pumped by the Waikerie Salt Interception Scheme, the other not pumped by an interception scheme. Approximately 40 km of data were recorded at 3-5 km/hr with a horizontal resolution of about 4 m and an effective signal penetration to 25 m depth. The survey path was tracked using a GPS, enabling three dimensional presentation of the survey lines. Surface-water resistivity and water depth were recorded during the survey and were used to assist interpretations of the data.

Waikerie Salt Interception Scheme production bore locations correlated with resistive features in the top 5 m of alluvium, consistent with fresh river water being drawn through the sediments due to production bore pumping. This suggested that hydrology is at least as significant as geology in determining the sub-surface resistivity structure. Conductive anomalies identified with the TEM technique have been interpreted as salt-load hot-spots and have been correlated with run-of-river determined salt-loads. The towed NanoTEM array is recommended as a useful tool for identifying small scale (50 m) salt-load hot-spots.

This work contains no material which has been accepted for the award of any other degree or diploma in any university or other tertiary institution and, to the best of my knowledge and belief, contains no material previously published or written by another person, except where due reference has been made in the text.

I give consent to this copy of my thesis, when deposited in the University Library, being available for Loan and photocopying.

21/5/03

Brian Edward Barrett

Acknowledgements

I would like to thank my supervisor, Dr Graham Heinson for his commitment and dedication to my work. I gave myself a tight deadline for the completion of my degree, and Graham was relentless in his efforts to help me meet this deadline. I extend this vote of thanks to my external supervisors, Michael Hatch of Zonge Engineering and Andrew Telfer of Australian Water Environments. Thank you also to Barry Porter and David Allen for assistance and collaboration in data acquisition and to Noel Merrick for providing information on the Sandburg inversion code.

Thanks to every one who reviewed my work, including Graham Heinson, Michael Hatch, Andrew Telfer, Stewart Greenhalgh, Linda Deer, Hashim Carey, Ian Lau, Hazel Hayward and Sean Mahoney. Your comments and suggestions have been well received and extremely helpful.

The assistance provided by all the staff at Australian Water Environments and Zonge Engineering has also been very much appreciated. In particular, thank you to Marion Santich, Geoff White and Michael Wall.

Finally, thank you to all my family and friends for being there when I needed them, and tolerating me when tired and stressed.

This project was conducted under the auspice of the Cooperative Research Centre for Landscapes Environment and Mineral Exploration (CRC LEME).

Chapter 1

Introduction

1.1 Preamble

Salinity is an expensive nationwide problem in Australia. According to the Government's National Action Plan for Salinity and Water Quality (NAP, 2003), more than $130 million of agricultural production is lost annually due to salinity, more than $6 million are spent each year on building maintenance related to salinity in South Australia and $9 million damage is caused to roads and highways in New South Wales. Furthermore, the problem is increasing. Estimates show that within 20 years, Adelaide's drinking water will exceed World Health Organisation standards for desirable drinking water on two out of every five days, due to the increasing salinisation of the Murray River (NAP, 2003).

Salinity problems in Australia are generally caused when an imbalance occurs between the volume of water reaching the ground (by rainfall and irrigation) and that leaving the ground (by such processes as evaporation, transpiration or plant use, aquifer recharge and surface run-off). The major causes of this imbalance are excess irrigation and reduced transpiration (due to the clearing of deep rooted plants). An excess of groundwater builds up when this imbalance exists, dissolving and mobilising sediment-stored salts. Once mobilised, these salts may cause salinity problems as saline groundwater rises to the near surface or is migrated laterally to cause a salinity problem at a different location (e.g. *break-of-slope* salinity and salinisation of rivers and channels). One such problem is the salinisation of the Murray River.

The increasing salinisation of the Murray River is an environmental and social problem. The effect of high salt-loads along the length of the river is to lower the water quality for all users (particularly those at the South Australian end of the system). The environmental consequences of lower water-quality are potential flora and fauna extinctions due to intolerances of saline water supplies. Social problems arise from our various uses of Murray River water. Saline water can reduce crop yield when used for irrigation, increase rates of corrosion in industry applications and residential hot-water systems and can be

undesirable as drinking water. The end result of each of these problems is increased expense for the public.

Salt-load monitoring techniques are required along the Murray River to determine locations where saline water accession is high. This information might be used to design a mitigation system such as a Salt Interception Scheme (SIS) or assess the efficiency of an existing mitigation system. Such monitoring techniques need to locate salt-load "hot-spots" to a scale of approximately 50m. Furthermore, the technique needs to be fast and affordable so that the survey can be repeated for regular monitoring.

1.2 Regional Geology

1.2.1 Geology

The Murray Basin is a shallow epi-cratonic sedimentary basin covering approximately 300,000 km^2 of south-eastern Australia (Figure 1.1). It contains rocks and unconsolidated sediments of Cainozoic age (Brown and Stephenson, 1991).

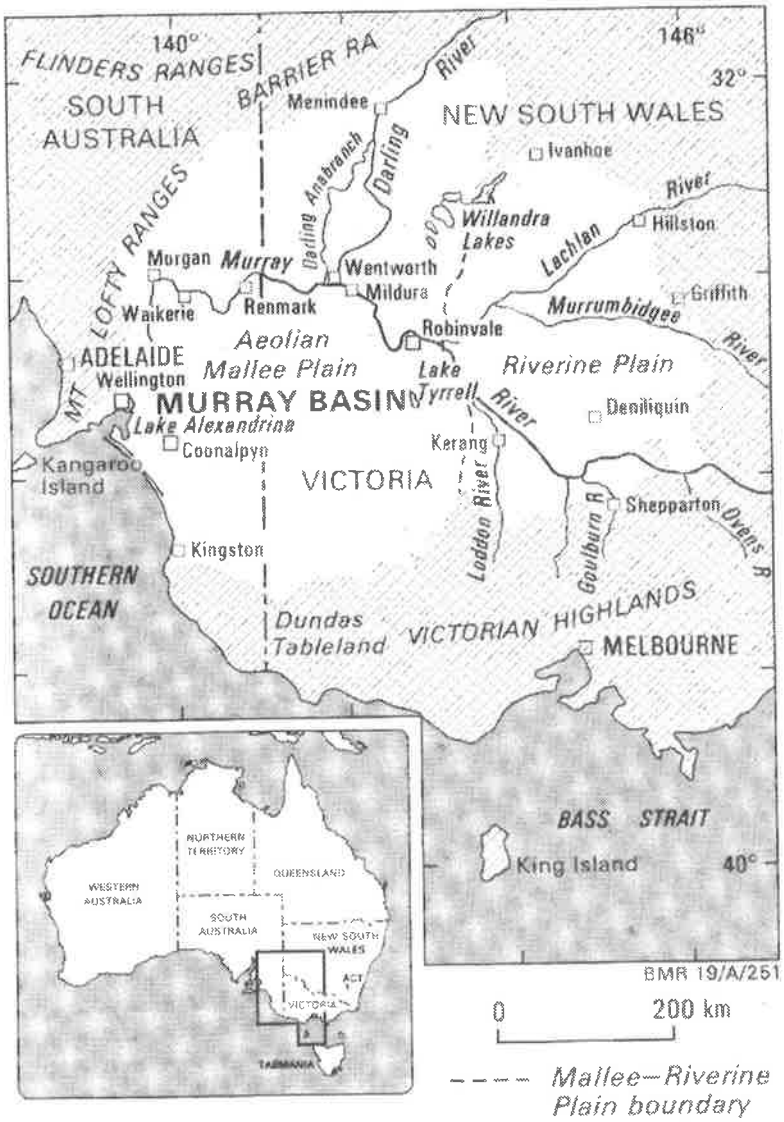

Figure 1.1: Location map of the Murray Basin (after Brown and Radke, 1989)

Murray Basin sediments have a total thickness of approximately 600m at the basin's deepest point, with an average thickness of about 250-300m across the basin. The Basin contains three major groups as shown in Figure 1.2. The oldest group is a widely

distributed group of mostly terrestrial (fluvial and lacustrine) sediments ranging from 60 Ma (Paleocene) to 10 Ma (Middle Miocene), called the Renmark Group (Brown, 1989).

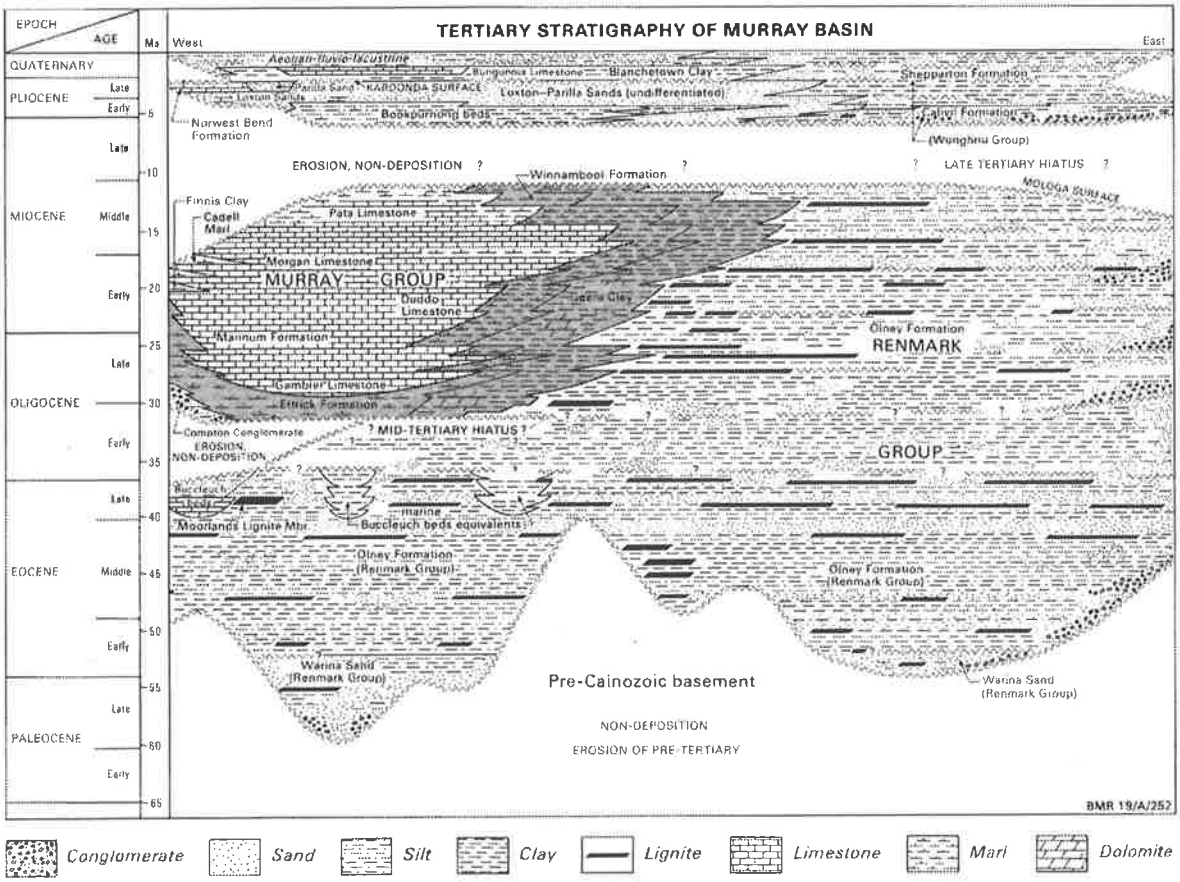

Figure 1.2: Chrono-stratigraphic diagram of the Murray Basin showing the main geological groups (after Brown and Radke, 1989).

Following a Mid-Tertiary (approx 32 Ma) marine intrusion from the western margin of the basin, the Murray Group was deposited (Brown, 1989). The Murray Group covers approximately 120,000 km^2 of the western region of the Murray Basin and has a maximum thickness of 150m. It contains Oligo-Miocene sediments from an open to restricted shallow marine setting. The terrestrial sediments of the Renmark Group continued to be deposited in the east, adjacent the inland sea. Lukasik and James (1998) provide a detailed review of the units and members of the Murray Group based on geographic and biolithological variations. In this review the term Murray Supergroup was coined, replacing the term Murray Group.

Following a period of erosion, a series of marine transgression-regression cycles occurred during the Pliocene and Pleistocene (last 5 or 6 million years), depositing the most recent

major Murray Basin Group (Brown and Stephenson, 1991). The most recent transgression was followed by uplift of the Pinnaroo Block on the south-western margin of the basin (approx 2.5 Ma). This created the shallow fresh-water Lake Bungunnia over the western portion of the basin (Brown and Stephenson, 1991; Klingner, 2000; White, 2000). The drying of Lake Bungunnia corresponds with the onset of aridity in South Australia, which produced the aeolian sands that cap most of the Murray Basin (Stephenson, 1986; Wall, 2001).

Ludbrook (1957; 1961) initially developed the Tertiary stratigraphy of the Murray Basin in South Australia as part of hydrological investigations. Brown (1989) provides an overview of the evolution of the Murray Basin and a stratigraphic framework for the groundwater occurrences in the basin. Other important works include Giles (1972), Carter (1985) and Brown and Stephenson (1991) who have studied depositional environments of the Murray Basin as well as Lindsay and Barnett (1989), McGowran et al. (1997), Lukasik & James (1998) and Wall (2001) who have undertaken biostratigraphic investigations.

1.2.2 Hydrology

Low-permeability layers exist between the major geological groups and act as confining layers for groundwater systems. The hydrology of the Murray Basin can therefore be divided into three major aquifer systems that correspond to the division of major sedimentary groups discussed above (Figure 1.3).

The Renmark Group Aquifer System is the basal confined aquifer of the Murray Basin (Brown, 1989). In the southwest of the basin it is confined from above by the Ettrick Formation of the Murray Group. The Ettrick formation is also the lower confining layer of the Murray Group Aquifer (MGA) as labelled in Figure 1.3. In the north and east of the basin, the upper boundary of the Renmark Group Aquifer System is the base of the Pliocene-Pleistocene sedimentary group. The Renmark Group Aquifer System is often sub-divided into upper, middle and lower aquifer units, based on lithology, water quality, water pressure and palynological criteria (Kellet, 1989; Macphail and Truswell, 1989). The lower Renmark Group Aquifer extends across the entire Murray Basin (Evans and Kellet, 1989). The middle and upper Renmark Group Aquifers are bounded to the west by the mid-Tertiary low-permeability barrier as shown in Figure 1.3.

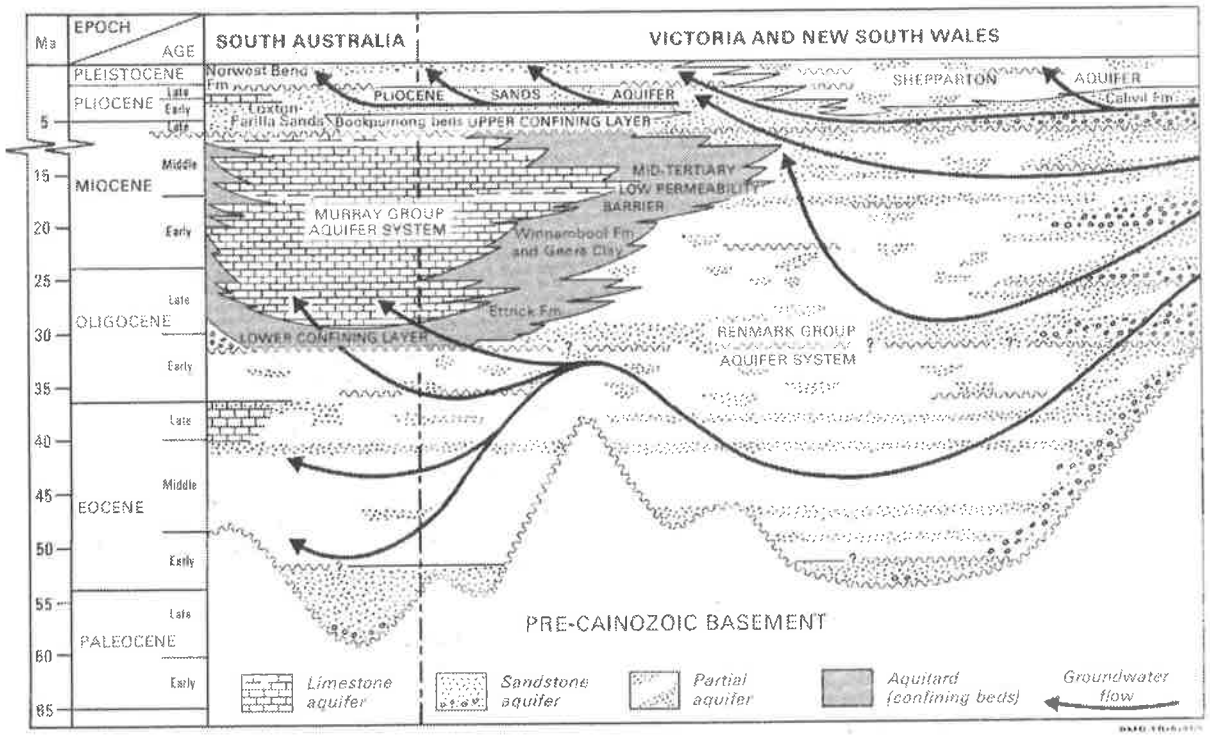

Figure 1.3: Chrono-stratigraphic diagram of the Murray Basin showing the major aquifer systems and their dominant groundwater flow direction (after Brown and Radke, 1989).

The MGA (Figure 1.3) is the most intensively exploited regional aquifer in the Murray Basin (Evans and Kellet, 1989). It exists in the limestone units of the Murray Group, which were deposited during a series of marine transgressions. It is confined at its base by the Ettrick formation (lower confining layer) and to the east by the mid-tertiary low-permeability barrier, which represents the inland extent of the shallow marine environment (Evans and Kellet, 1989). Finally, an upper confining layer exists over the north and east of the Murray Group, in the Bookpurnong beds. The aquifer is relatively unconfined in the southwest (Brown, 1989).

The Pliocene-Pleistocene sediments contain the Pliocene Sands Aquifer and the Shepparton Partial Aquifer System (Evans and Kellet, 1989). The Pliocene Sands Aquifer sits over the upper confining layer of the MGA (the Bookpurnong Beds) and is capped by the Blanchetown Clay in the middle of the Murray Basin. In the east it is only partially confined between the Upper Renmark Group Aquifer and the Shepparton Partial Aquifer System. In the west however, the aquifer is unconfined (Figure 1.3).

1.3 Salt

Major sources of salt in the sediments of the Murray Basin are remnant salt particles in the pores of marine derived sediments, accumulated salt (from sea spray and evaporation of meteoric water) and salts produced through the weathering of original sediment particles by meteoric water (Jones, 1994; Telfer et al., 2000; White, 2000). Particularly important ions for groundwater salinity are reported in Table 1.1

Cations		Anions	
Sodium + Potassium	$Na^+ + K^+$	Bicarbonate + Carbonate	$HCO_3^- + CO_3^-$
Calcium	Ca^{2+}	Sulphate	SO_4^{2-}
Magnesium	Mg^{2+}	Chloride	Cl^-

Table 1.1: Major ions contained in groundwater in the Murray Basin (after Telfer et al., 2000)

Meteoric water containing carbon dioxide (CO_2) causes weathering of limestone and dolomite, which produces the bicarbonate anion (HCO_3^-) in abundance in the MGA. The most significant cation in these waters is sodium (Na^+) which originates from the weathering of clay minerals and feldspars. Finally, the solution of evaporites during wet periods provides a significant input of both sodium cations and chloride anions (Cl^-).

The MGA is dominated by Na^+ and Cl^- ion concentrations and ranges from water with less than 1500 mg/L Total Dissolved Salts (TDS) to saline water with more than 30,000 mg/L TDS (for comparison, sea water has approximately 35,000 mg/L TDS) (Evans and Kellet, 1989).

1.3.1 Hydrogeology of the Waikerie Region, South Australia

This project focuses on the hydrogeology associated with the Waikerie irrigation area (Figure 1.4). In this area, groundwater averages approximately 20,000 mg/L TDS. Stratigraphy of the survey region is shown in Figure 1.5 and important formations and hydrology features are described.

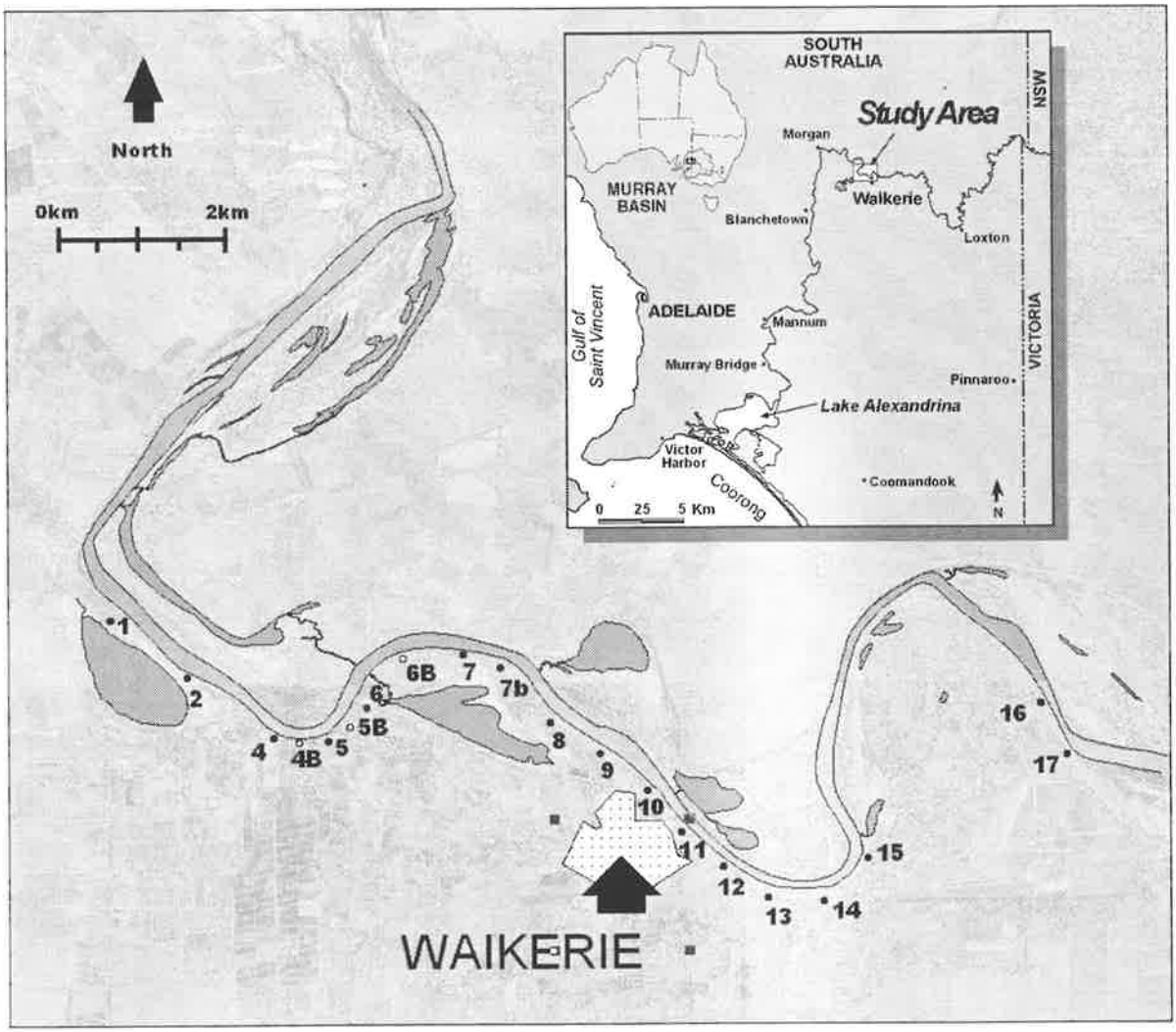

Figure 1.4: Location map for the Waikerie irrigation area. Production bores of the Waikerie Phase I SIS are labelled. Open symbols represent production bores that had not commenced operation at the time of the survey.

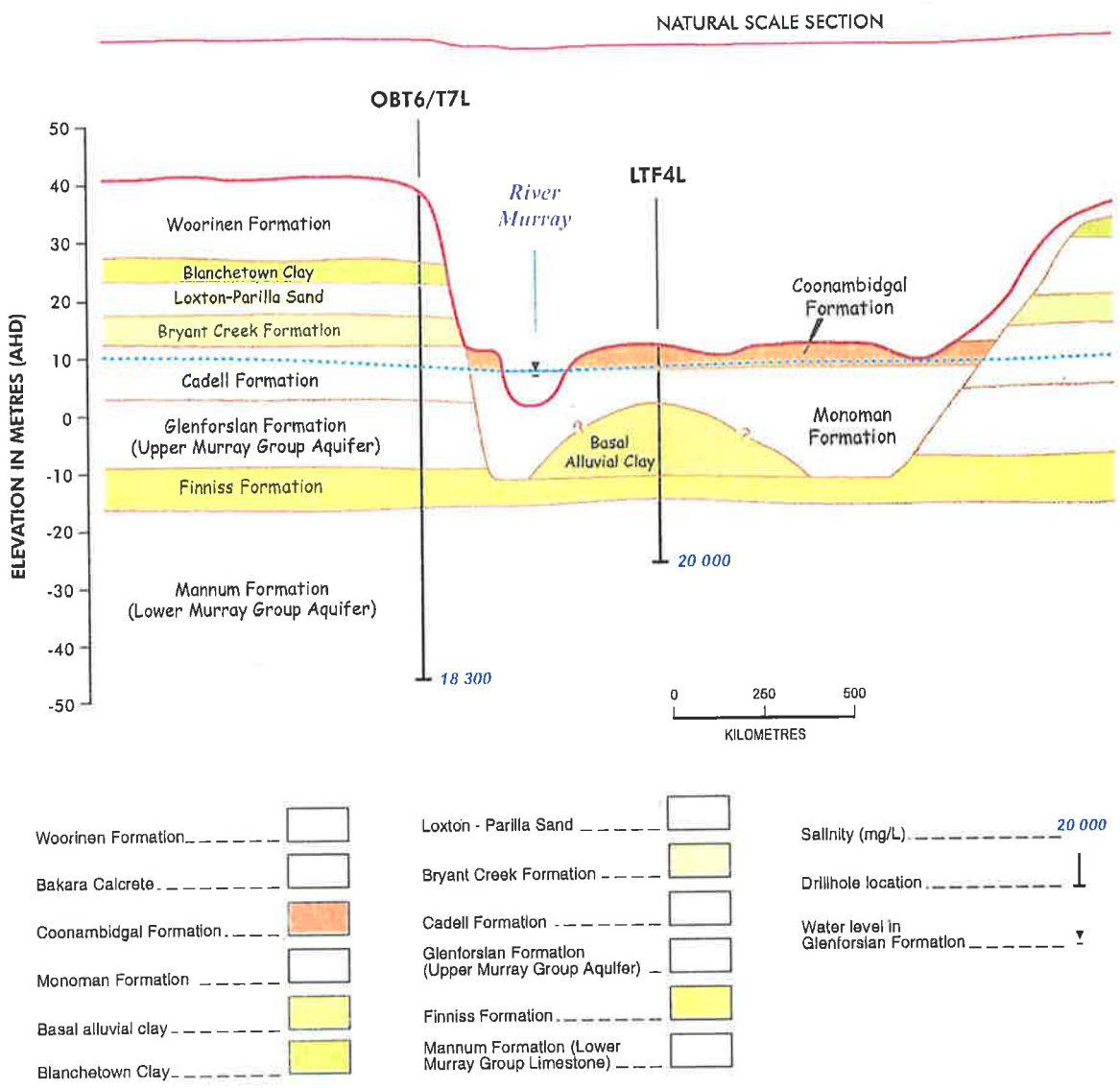

Figure 1.5: Typical Cross section from the Waikerie area showing lithological formations and their associated hydrology. Figure provided by Australian Water Environments.

Mannum Formation and the Lower Murray Group Aquifer: The Mannum Formation is a highly fossiliferous limestone of the Late Oligocene and the Early Miocene that was deposited in a warm shallow-marine to littoral environment (Ludbrook, 1961; Brown and Stephenson, 1991). The Mannum Formation is host to the Lower MGA, which is recognized as a major source of saline water accessions to the Murray River (Telfer and Watkins, 1991).

Finniss Formation: Due to clay content, the Finniss Formation is relatively impermeable but is an inconsistently distributed formation. The Finniss acts as a confining layer for the Lower MGA, resisting groundwater flow into the overlying Monoman Formation (Telfer

and Watkins, 1991). Variability in distribution of this formation is an important aspect in understanding saline water accession volumes to the Murray River.

Glenforslan Formation and the Upper Murray Group Aquifer: Glenforslan Formation is a sublithified to unlithified limestone of consistent 13-15 m thickness (Lukasik and James, 1998) containing the Upper MGA. Due to fluctuations in the regional groundwater table and weathering from meteoric water, the Glenforslan exhibits secondary porosity, resulting in much higher permeability than in the Lower MGA (Telfer and Watkins, 1991).

Cadell Formation: The Cadell Formation predominantly consists of calcareous clay deposited in a restricted marine to lagoonal environment in the Lower Miocene, possibly during the 17 Ma global fall in sea level (Brown and Stephenson, 1991). The Cadell is a confining layer for the Upper MGA.

Basal Alluvial Clay: Black organic alluvial clays are part of the Monoman Formation, but their occurrence is variable (Telfer and Watkins, 1991). Such clays will have significant implications to the pattern of saline water accession from the Lower MGA.

Monoman Formation: The Monoman is a Late Pleistocene to Early Holocene coarse-grained sand and gravel formation (Brown and Stephenson, 1991) that was deposited in the Murray River flood-plain valley, which is approximately 1000 m wide. The Monoman Formation is a mostly permeable conduit for saline water flowing from the Lower MGA into the Murray River.

1.3.2 Salt-load Development

Before human intervention, the Upper and Lower MGA behaved as a single aquifer despite the aquitard unit between them (Finniss Formation). As a single aquifer, the MGA was a saline system (30,000 mg/L) that contributed to natural salt-loads on the river.

The development of increasingly high salt-loads on the Murray River in the Riverland area of South Australia is a response to clearing of vegetation by early European settlers and, more significantly, irrigation activities that were introduced in the late 19th Century (Telfer and Watkins, 1991). Effective crop irrigation usually results in excess near-surface water. When drainage of excess water is prohibited by impermeable layers or aquitards (often

clay), *groundwater mounds* or *perched water tables* are formed (Telfer et al., 2000; Barrett et al., 2002). In the Waikerie area of the Murray Basin (Figure 1.4) the Blanchetown clay and the Cadell Marl (Figure 1.5) act as aquitards allowing perched water tables to form. When the perched water table reaches the root zone or the ground surface, water logging problems are encountered and crop quality is threatened.

An established local-scale treatment for water logging involves the drilling of drainage bores (Telfer and Watkins, 1991). These bores penetrate the aquitard units into the Upper MGA (Figure 1.5) allowing perched water tables to drain away. This method has been successful in locally treating water logging of farm-land. A regional impact can also be achieved with a high density of drainage bores across an area (Telfer and Watkins, 1991). In the Waikerie irrigation area approximately 280 drainage bores have been drilled since the 1920's (Telfer and Watkins, 1991). Water draining through irrigation drainage bores in the Waikerie area have flushed and pressurised the Upper MGA, which in turn manifests high pressures in the Lower MGA. These high pressures increase upward leakage of saline water through the Finniss aquitard, into the Monoman Formation and ultimately into the Murray River. This salt-load mechanism is illustrated in Figure 1.6a.

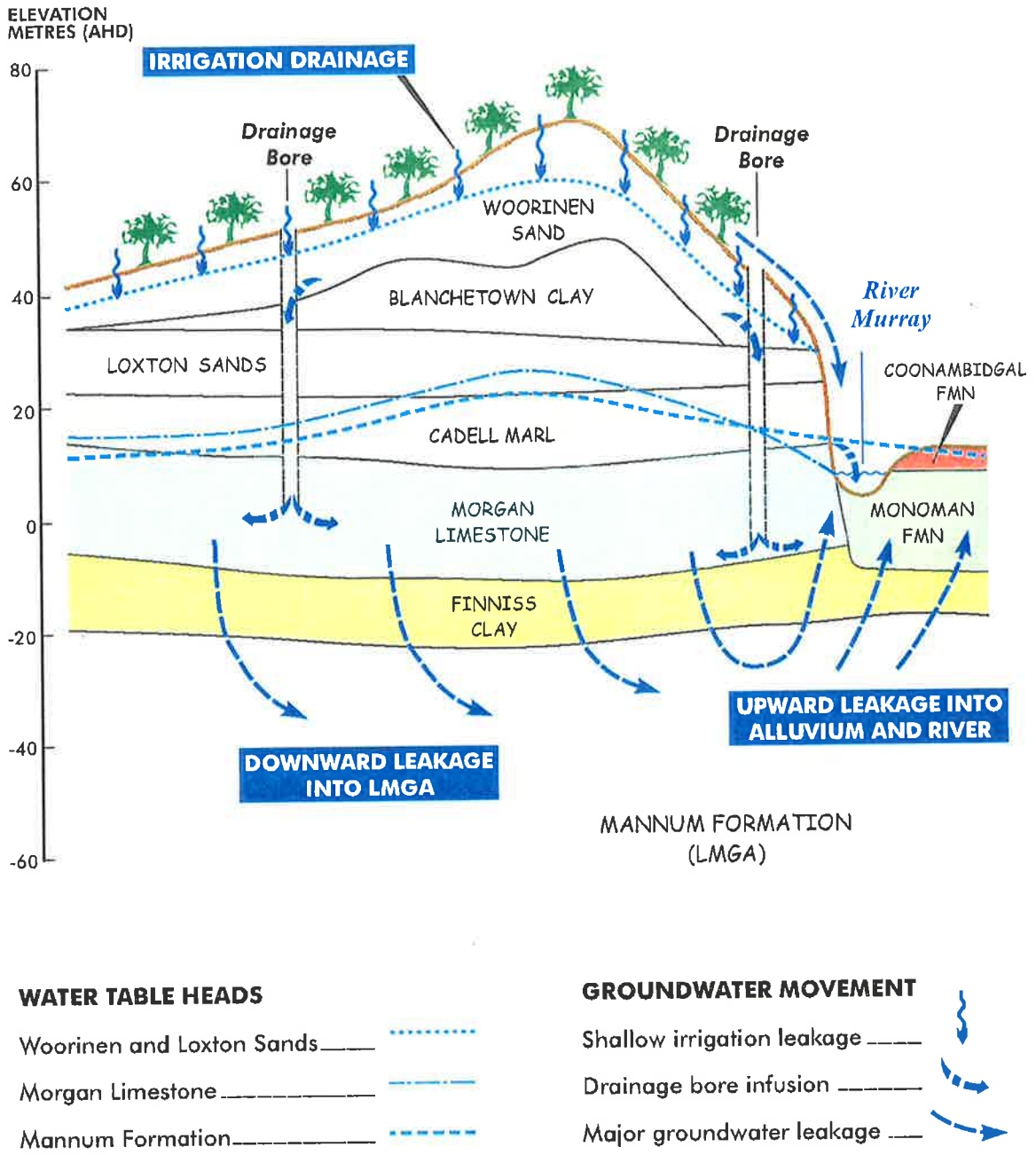

Figure 1.6a: The mechanisms involved in producing large volumes of saline-water accession to the Murray River. Water logging produced from irrigation drainage is reduced through the drilling of drainage bores. These over pressurise the Upper and Lower Murray Group Aquifers, resulting in saline groundwater flowing into the river Alluvium and subsequently, the Murray River. Figure provided by Australian Water Environments.

1.3.3 Salt Interception

In an attempt to combat Murray River salinity, salt interception schemes (SIS) have been established (Lindsay and Barnett, 1989; Telfer and Watkins, 1991). Such schemes involve pumping water from boreholes (production bores) that intersect the Lower MGA close to the river. This pumping reduces the excess head (or pressure) of the aquifer, reducing saline water flow into the river sediments above. Without the upward gradients produced by the over pressurised Lower MGA, groundwater from the alluvial sediments will leak down into the Lower MGA (Figure 1.6b). In such circumstances, saline leakage into the river is minimised. For schemes to effectively reduce river salinity, interception wells need to intersect the appropriate aquifer system, be spaced close enough to prevent upward leakage mid-way between wells (typically 500-1000m) and be close enough to the river to prevent saline inflow on both sides of the river. Production bore placement needs to take into account local variations in saline inflow that arise due to variations in irrigation activities and geological changes.

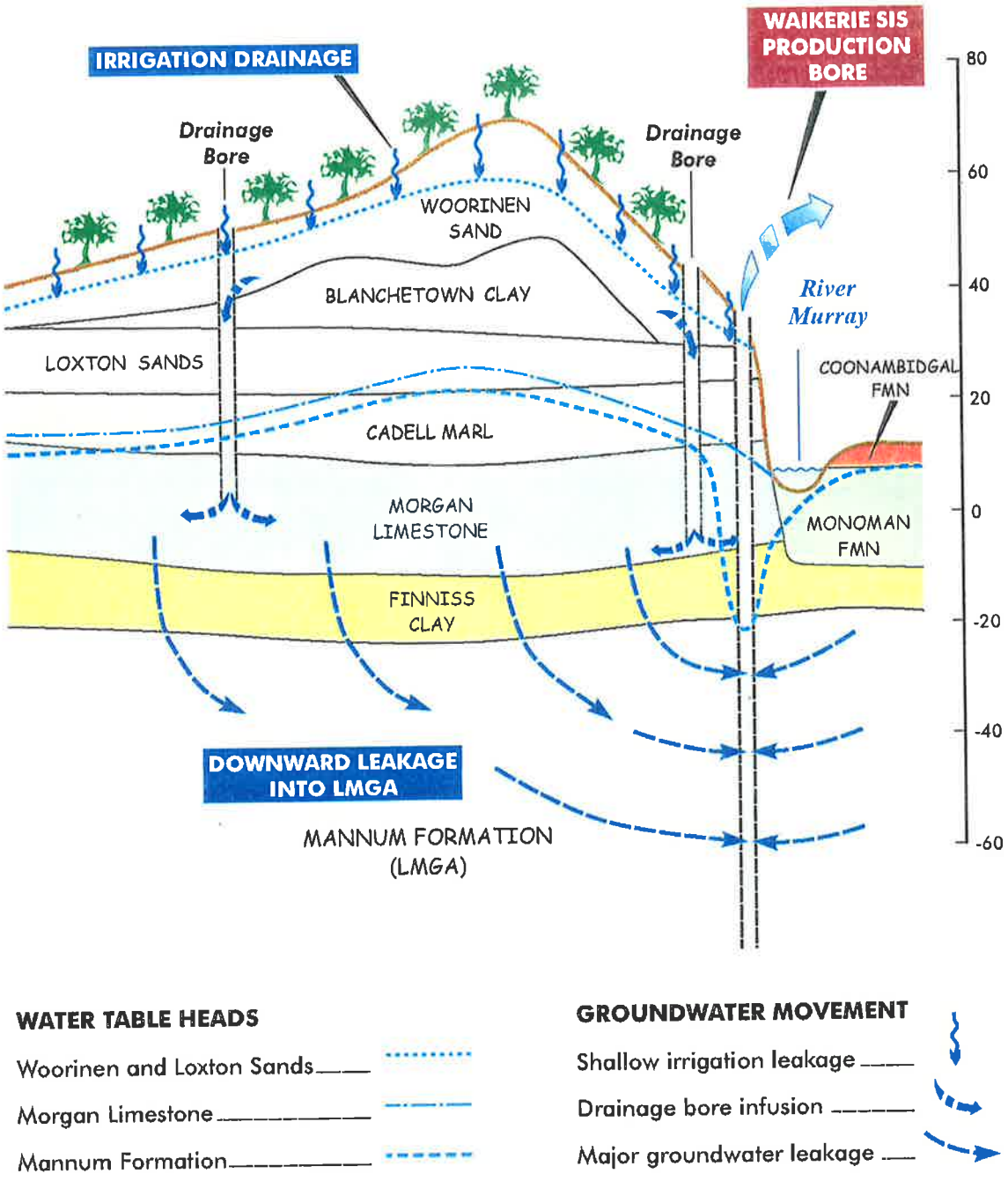

Figure 1.6b: After installation of the Waikerie Salt Interception Scheme, Lower Murray Group Aquifer pressure (head) is reduced near the production bores, minimising saline-water accession to the river. Figure provided by Australian Water Environments.

Salt interception is not a complete solution to the salinity problem as much as it is relocation. The saline water pumped from the Lower MGA is piped to *disposal basins* such as the Stockyard Plains Disposal Basin for the Waikerie SIS, for storage and evaporation (Evans, 1989; Barrett et al., 2002).

1.3.4 Current Monitoring Methods

Currently *run-of-river* salinity surveys are used for monitoring Murray River salt-loads (Porter, 1997; Telfer and Way, 2000). A run-of-river survey involves electrical conductivity (EC) measurement of surface river-water at 1 km intervals, which are converted to salinity. These measurements are repeated over approximately five consecutive days. The changing location of similar patterns in each of the five days of data is used to estimate the flow-rate of the river water. Parcels of water are tracked using water-flow data, and increases in salinity are plotted against river location. For example, if the rate of river flow was estimated at 2km/day, then the EC at one location is compared with the EC two kilometres down stream on the next day. Significant horizontal changes in salinity can be interpreted as regions where groundwater inflow is high, and is calculated as a salt-load in tonnes of salt per day per kilometre (t/d/km).

Inflowing saline water is denser than the fresher river water. Changes in river depth or river bends are required for water to become well mixed (Telfer, 1989). Since measurements are made only near the river surface, anomalies are swept downstream before completely mixing with the water column. Salt-loads calculated from this method must therefore be corrected for downstream displacement. Run-of-river surveys are only feasible during stable river flow periods (Porter, 1997). Figure 1.7 shows the salt-loads calculated from a run-of-river survey conducted in July 2002.

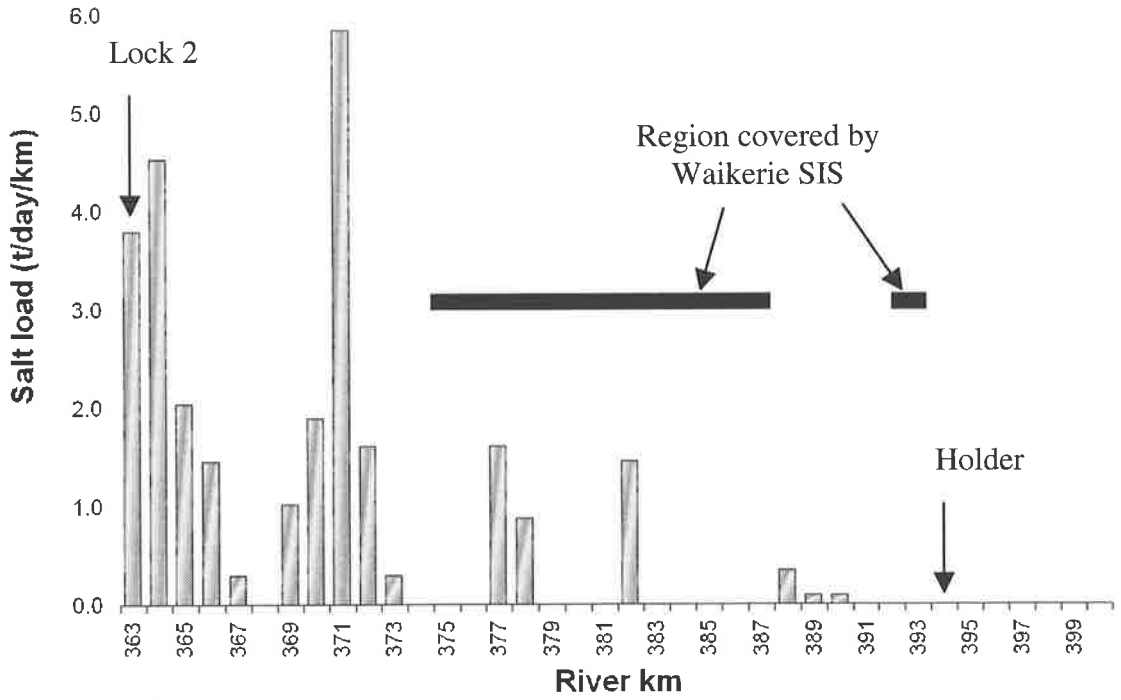

Figure 1.7: Calculated salt-loads per kilometre from Lock 2 to Holder. The river kilometres covered by the Waikerie SIS are indicated (downstream to left).

Longer term measurements are made at *salinity monitoring pontoons.* These measure the EC of the surface river-water at fixed and permanent locations using a toroidal coil. Measurements are recorded every 30 minutes. Salinity monitoring pontoons are more widely spaced (10 km or more) than run-of-river sampling points, but can take data year round, showing seasonal variation in river salinity. They are also used to show year to year variation in the river salinity and to verify and calibrate run-of-river surveys (Porter, 1997; Vivian et al., 1998; Telfer and Way, 2000). Figure 1.8 shows data from three salinity monitoring pontoons.

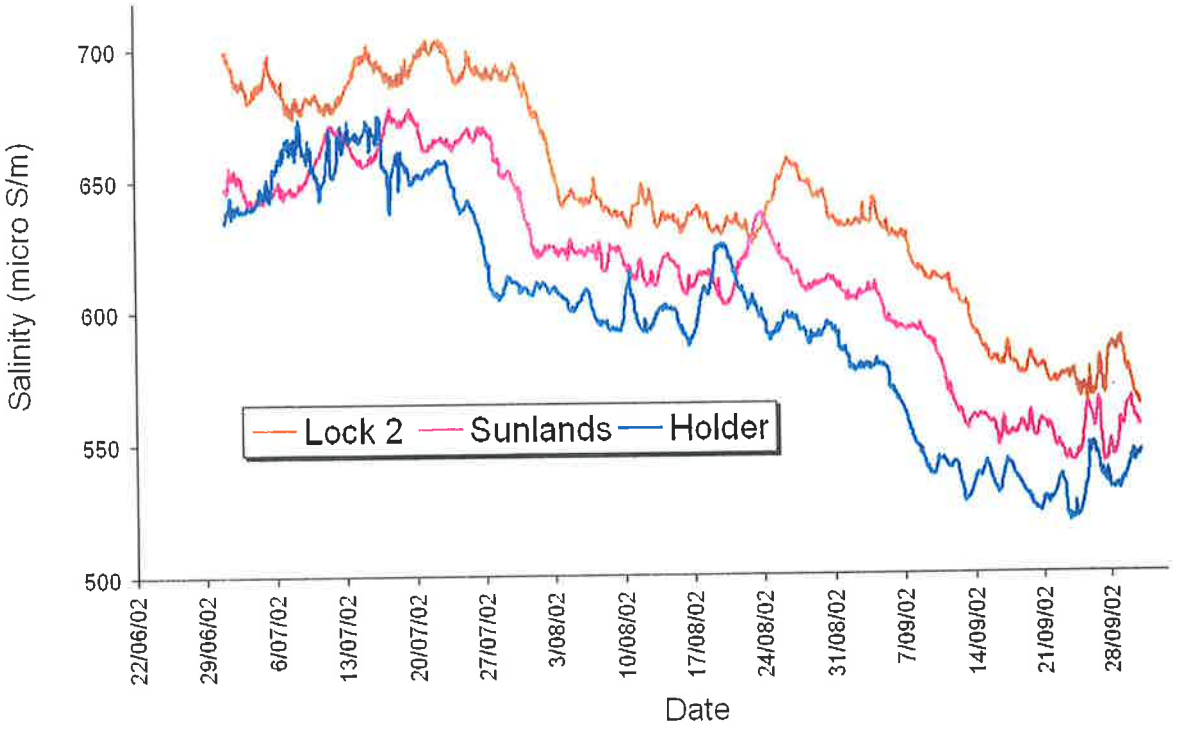

Figure 1.8: Data from three salinity monitoring pontoons over three months. Lock 2 is downstream of the survey area, Holder is upstream of the survey area and Sunlands is in the survey area. It shows that the salinity of the river increases down stream. Also, water flow rates can be determined by comparing the relative time that similar salinity patterns occur at each pontoon.

Neither run-of-river surveys nor salinity monitoring pontoons give a fast and accurate technique with sufficiently high lateral resolution (50 m) for locating saline water inflow hot-spots. Run-of-river surveys can only be undertaken during specific flow conditions, are time consuming (requiring approx five days of measurements) and suffer from anomaly displacements due to river flow while salinity monitoring pontoons provide only widely spaced data. Both methods are also affected at the merging of streams and tributaries. Where a fresh water stream merges with the Murray River, apparent freshening of river water occurs, masking salt-loads. Conversely, where high salt-loads exist in the merging stream, existing survey methods will predict higher salt-loads in the Murray River near the merging point.

1.4 Project Aims

The principal aim of this study was the development of a towed geophysical survey system that responds to the salinity of water in porous sediments in the top 5m of alluvium. If fresh water is contained in these sediments, it is reasonable to assume that the water flow gradient is down; where these sediments contain saline water, the flow gradient is likely to be upwards and the SIS can be described as inefficient.

A system was developed to evaluate the efficiency of The Waikerie Phase I SIS in cooperation with Australian Water Environments, the Department for Water Land and Biodiversity Conservation (South Australia) and Zonge Engineering and Research Organisation (Australia). Furthermore, the system was designed to identify locations where Interception is most critically required (salt-load hot-spots), thus aiding in the design of a SIS.

It was necessary for the system to be practical, cost-effective and relatively fast. Existing techniques (run-of-river surveys) require five complete days of data acquisition to produce a map of salt-loads. Given that salt-loads can be localised to very small locations (perhaps due to faults, clay lensing or trench locations in the river) the system also needed to locate hot-spots to within 50m (compared to the 1 km or worse resolution of run-of-river surveys). Finally, to develop confidence in the system, we aimed to demonstrate repeatability in the measurements.

Geophysical systems were tested on two contrasting river stretches. The first of these was a stretch that is currently pumped by the Waikerie SIS, the second was a stretch that was not yet pumped by a SIS, and is known to contribute substantial salt-loads to the Murray River.

To summarise, the geophysical aims of this survey were:

- Develop a practical, cost-effective and fast survey method that responds to salinity changes of water in the top 5 metres of alluvium beneath a river;
- Develop a data processing stream for such a system and demonstrate the ability to quickly produce models and interpretations. Part of this development involved an investigation into inversion techniques, including the fixing of known parameters (such as river depth and water resistivity).

The hydrogeological aims of the particular chosen survey location were:

- Assess the relative efficiency of the Waikerie Phase I SIS, identifying the effect of production bores on the local hydrology and locations where the Scheme is not sufficiently reducing saline-water accession;
- Locate salt-load hot-spots in an unpumped river stretch which may have implications for the placement of production bores for the Waikerie Phase II SIS.

Chapter 2

Theory

2.1 Physical Properties for Salinity Detection

The principal earth parameter that allows geophysics to be used to locate salt-loads, is electrical resistivity ρ (inverse of conductivity σ). Resistivity is the point property of a material that determines how easily it can carry an electrical current (Kearey and Brooks, 1991). Resistivity varies over several orders of magnitude in the Earth, depending on rock type, the nature of rock fluids and rock porosity.

Some typical resistivity values for saturated to partially saturated alluvium and sands are in the range 10-800 ohm.m. Crystalline basement rocks are typically much more resistive, being anywhere between 3 x 10^2 ohm.m and 10^6 ohm.m, while clays can typically make sediments more conductive due to surface charge movement on the clay minerals. Typical resistivity values for clays are between 1 ohm.m and 100 ohm.m. Water resistivity ranges from 0.05 ohm.m for saline aquifers up to about 100 ohm.m for meteoric water (sea-water has a resistivity of approximately 0.3 ohm.m). Kearey and Brooks (1991); Telford et al. (1990); and Ward and Hohmann (1988) provide more specific tables of typical resistivities of materials.

Variation in rock porosity ϕ plays a significant role in determining bulk resistivity due to the contrast between rock resistivities and that of their more conductive contained fluids. Archie's law (Archie, 1942) is an empirical law that relates bulk resistivity to porosity, saturation and fluid resistivity:

$$\rho_b = \frac{\rho_w \rho_r}{a\phi^m S^n \rho_r + \rho_w} \tag{2.1}$$

where ρ_b is the bulk resistivity of the formation, ρ_w is the resistivity of the contained fluids, ρ_r is the resistivity of the rock components (sand or clay), ϕ is the formation fractional porosity, S is the formation fractional saturation and a, m and n are empirical constants. In the present study a and m were set to 1 and 2 respectively, while the value of n was irrelevant because saturation S was assumed to be 1.

Archie's Law is more commonly written in terms of conductivities:

$$\sigma_b = a\phi^m S^n \sigma_w + \sigma_r \tag{2.2}$$

In this form the conductivity of rock components, σ_r is significant when the formation contains clays. If there is no clay present, Archie's Law can be written in terms of saturation, porosity and fluid conductivity only.

$$\sigma_b = a\phi^m S^n \sigma_w \tag{2.3}$$

which becomes

$$\rho_b = \frac{\rho_w}{a\phi^m S^n} \tag{2.4}$$

Fluid resistivity can be related to salinity through total dissolved salts (TDS in mg/L) (Keller and Frischknecht, 1966). Common values for TDS are less than 200 mg/L for drinking water (up to 1000 mg/L is considered drinkable water), 35,000 mg/L for sea-water and up to 100,000 mg/L for saline aquifers (Bouwer, 1978; Telfer et al., 2000). Fluid salinity is usually measured in EC units, which are equivalent to µS/cm. Values can be converted to TDS from EC units through a conversion factor that is dependant on the types of cations and anions present in the water (0.55 is used in the present study). Also, EC units can be converted to resistivity units (ohm.m) by dividing by 10,000 (to get S/m) and inverting the value.

In this survey, river water was measured to be approximately 600 EC. This converts to approximately 16 ohm.m. Typical porosity values for unconsolidated sands, silts and clays are between 40 and 60% (Bouwer, 1978). Using 16 ohm.m for ρ_w and assuming a sediment porosity of 55% gives a bulk resistivity ρ_b of 50 ohm.m for fresh-water saturated alluvium. If water in alluvium is saline (say 20,000 mg/L TDS) bulk resistivity will be less than 1 ohm.m.

2.2 Maxwell's Equations

All electric and electromagnetic processes obey Maxwell's equations, given as

$$\nabla \times \mathbf{E} = -\frac{\partial \mathbf{B}}{\partial t} \tag{2.5}$$

$$\nabla \times \mathbf{H} = \mathbf{J} + \frac{\partial \mathbf{D}}{\partial t} \tag{2.6}$$

where **E** is electric field intensity (V/m), **B** is magnetic flux density (webers/m^2), **H** is magnetic field intensity (ampere-turns/m), **D** is electric displacement (C/m^2) and **J** is current density (A/m^2) (Ward and Hohmann, 1988).

Equation 2.5 is the mathematical expression of Faraday's law; for any time varying magnetic field, an electric field will exist with intensity proportional to the negative rate of change in the magnetic field (Griffiths, 1999). Similarly, Equation 2.6 is the mathematical expression of Ampere's circuital Law; for any current flow, a magnetic field will exist with intensity proportional to the total current flow (Griffiths, 1999). In this case there are two types of current flow. The term **J** represents galvanic current flow, where electrons move freely through a medium, while $\partial \mathbf{D}/\partial t$ represents the displacement current, which is caused by charge separation or polarization in a dielectric (Ward and Hohmann, 1988; Telford et al., 1990).

There are two more Maxwell equations, which can be derived by substituting Equations 2.5 and 2.6 into the vector identity $\nabla . \nabla \times \mathbf{A} = 0$:

$$\nabla . \nabla \times \mathbf{E} = -\nabla . \frac{\partial \mathbf{B}}{\partial t} = -\frac{\partial}{\partial t}(\nabla . \mathbf{B}) = 0$$

and so, $\nabla . \mathbf{B} = 0$ (2.7)

This expression can be understood by considering magnetic field lines; to obey Maxwell's equations magnetic field lines always join up in loops (i.e. they do not diverge).

Secondly

$$\nabla . \nabla \times \mathbf{H} = \nabla . \left(\mathbf{J} + \frac{\partial \mathbf{D}}{\partial t} \right) = \nabla . \mathbf{J} + \frac{\partial}{\partial t}(\nabla . \mathbf{D}) = 0$$

and divergence of current density is equal to the negative rate of charge accumulation

$$\nabla \cdot \mathbf{J} = -\frac{\partial q}{\partial t}$$

where q is the electric charge density. Thus

$$\nabla \cdot \mathbf{D} = q \tag{2.8}$$

This expression describes current flow at an injection of charge; current flow diverges away from the current injection point.

The vector quantities defined in the four Maxwell's equations (**E**, **B**, **H**, **J**, and **D**) can be coupled in the frequency domain using the magnetic permeability μ, dielectric permittivity ε and electric conductivity σ (Ward and Hohmann, 1988)

$$\mathbf{B} = \mu\mathbf{H}, \quad \mathbf{D} = \varepsilon\mathbf{E}, \quad \text{and Ohm's Law } \mathbf{J} = \sigma\mathbf{E} \tag{2.9}$$

Magnetic permeability is a constant of proportionality that determines the relationship between a magnetic field intensity **H** and the magnetic flux density **B** that it creates in a body. It is determined by the magnetic susceptibility of that body. The free space value of magnetic permeability μ_0 is 4π x 10^{-7} H/m. For most materials μ does not vary significantly from the free space value, however in a few minerals, such as magnetite, μ can be as high as five times μ_0 (Telford et al., 1990).

Dielectric permittivity is a constant of proportionality that determines the relationship between electric field strength **E** and the displacement current **D** (or electrical polarisation) that is associated with it. The value of ε is dependant on the dielectric nature of the body and the frequency of the imposed electric field. Some materials (called dielectrics) have a dielectric permittivity us much as 100 times the permittivity of free space $\varepsilon_0 = 8.854 \times 10^{-12}$ (Telford et al., 1990).

Electrical conductivity (inverse of resistivity) is the property of a body that determines the size of the electrical current density **J** that flows in a body, for an applied electric field **E**. In common materials, σ varies over several orders of magnitude (as discussed in section 2.1).

2.3 DC Resistivity Theory

In the Direct Current (DC) Resistivity method, an electrical current source **I**, with current density **J** is introduced to the Earth. Ohm's law relates resistivity ρ to a current density and electric field **E** (Telford et al., 1990)

$$\rho = \frac{\mathbf{E}}{\mathbf{J}} \tag{2.10}$$

The electric field is the negative gradient of the scalar potential field V (Reynolds, 1997),

$$\mathbf{E} = -\nabla V \tag{2.11}$$

The distribution of the electrical potential is determined by the geometry of the current source, and the resistivity structure of the sub-surface and can be described by Maxwell's Equations. Time derivatives in Equations 2.5 and 2.6 can be set to zero because there is no time dependence on the input current. The only significant relation is then Equation 2.8 which, in terms of **E** is

$$\nabla . \mathbf{E} = \frac{q}{\varepsilon} \tag{2.12}$$

Taking the divergence of Equation 2.11 we have Poisson's Equation for the potential field in a source region (Griffiths, 1999)

$$\nabla . (\nabla V) = \nabla^2 V = -\frac{q}{\varepsilon} \tag{2.13}$$

In source-free regions (q = 0) Laplace's Equation applies (Griffiths, 1999)

$$\nabla^2 V = 0 \tag{2.14}$$

Poisson's and Laplace's equations describe the electric potential field V at and around a source of current for a homogenous region.

In the DC Resistivity method we estimate the sub-surface potential field (and hence the conductivity) by measuring the potential distribution on the Earth's surface.

For a current source on the surface of a homogenous half-space, the current is distributed over the surface of a hemisphere (area $2\pi r^2$). Current density, therefore, is related to the distance r from the current source and the total input current (Telford, 1990)

$$\mathbf{J} = \frac{I}{2\pi r^2} \tag{2.15}$$

Equation 2.10 can now be rewritten as

$$\frac{\delta V}{\delta r} = -\rho \frac{I}{2\pi r^2} \tag{2.16}$$

Thus the voltage V_r at a point distance r from the current source can be found through integration of Equation 2.16 (Reynolds, 1997)

$$V_r = \int \delta V = -\int \rho \frac{I}{2\pi r^2} \delta r = \frac{\rho I}{2\pi} . \frac{1}{r} \tag{2.17}$$

This formula can be applied to multiple current sources. If points A and B are current sources +I and –I respectively and the potential is measured at point M, we can sum the effect of each current source such that

$$V_M = \frac{\rho I}{2\pi} \left[\frac{1}{r_1} - \frac{1}{r_2} \right] \tag{2.18}$$

where r_1 and r_2 are distances from potential electrode M to current electrodes A and B respectively. This can be further extended to include two potential electrodes (M and N), which measure a potential difference (Reynolds, 1997).

$$\Delta V = \frac{\rho I}{2\pi} \left\{ \left[\frac{1}{r_1} - \frac{1}{r_2} \right] - \left[\frac{1}{r_3} - \frac{1}{r_4} \right] \right\} \tag{2.19}$$

where r_1 and r_2 are as before and r_3 and r_4 are distances from potential electrode N to current electrodes A and B respectively and where $\Delta V = V_2 - V_1$ (V_1 and V_2 are the potentials at electrodes M and N). Rearranging Equation 2.19 for apparent resistivity ρ_a,

$$\rho_a = \frac{2\pi \Delta V}{I} \left\{ \left[\frac{1}{r_1} - \frac{1}{r_2} \right] - \left[\frac{1}{r_3} - \frac{1}{r_4} \right] \right\}^{-1} \tag{2.20}$$

where the term in curly brackets is called the geometric factor. From Equation 2.20 the apparent resistivity can be found from a measured potential difference for any four electrode array configuration.

In the traditional dipole-dipole array (Figure 2.1) the distance between two current and between two potential electrodes is constant (dipole size, a), while the current pair – potential pair separation is varied. This separation distance is usually an integer multiple of the dipole size n x a, where n is the dipole number. From this configuration we can define r_1 to r_4 as follows

$r_1 = (n+1)a$
$r_2 = na$
$r_3 = (n+2)a$
$r_4 = (n+1)a$

The apparent resistivity formula for the traditional dipole-dipole array is then

$$\rho_a = \pi n(n+1)(n+2)a\frac{\Delta V}{I} \tag{2.21}$$

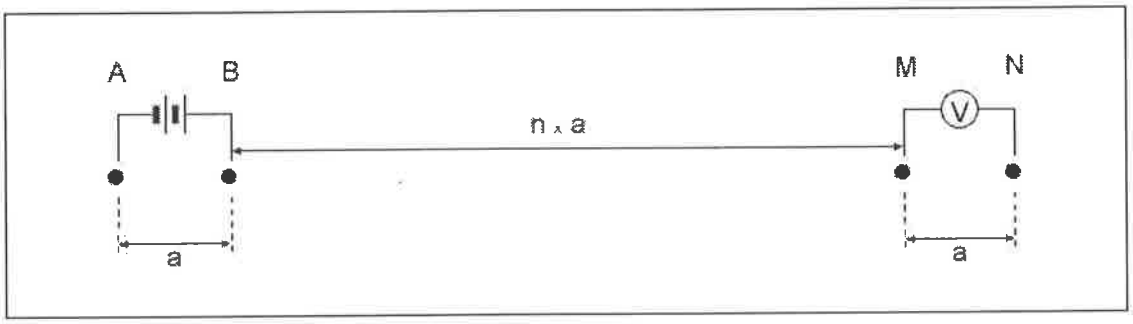

Figure 2.1: Traditional Dipole-Dipole electrode configuration. A and B are current source electrodes, M and N are potential electrodes, a is the dipole size and n is the dipole number.

2.4 Time-Domain Electromagnetic Theory

Electromagnetic (EM) survey methods measure the earth's response to a primary electromagnetic field H_p. This primary field is generated by a current flowing through a transmitter coil on the Earth's surface. When the applied current is changed rapidly (e.g. by turning it off abruptly) the EM fields become time varying. In this situation an electric field associated with the time-varying magnetic field (Maxwell's Equation 2.5) causes eddy currents to flow in buried conductors. These eddy currents produce a secondary magnetic field, H_s (Maxwell's Equation 2.6) that is measured at a receiver coil (Reynolds, 1997). Figure 2.2 shows the relationship between the transmitter coil, H_p, eddy currents, H_s and the receiver coil.

In the Transient EM (TEM) method measurements of the decaying eddy currents are made after the primary field is turned-off. In conductive ground the eddy currents decay slowly; in resistive ground the currents decay more quickly (Zonge, 1992).

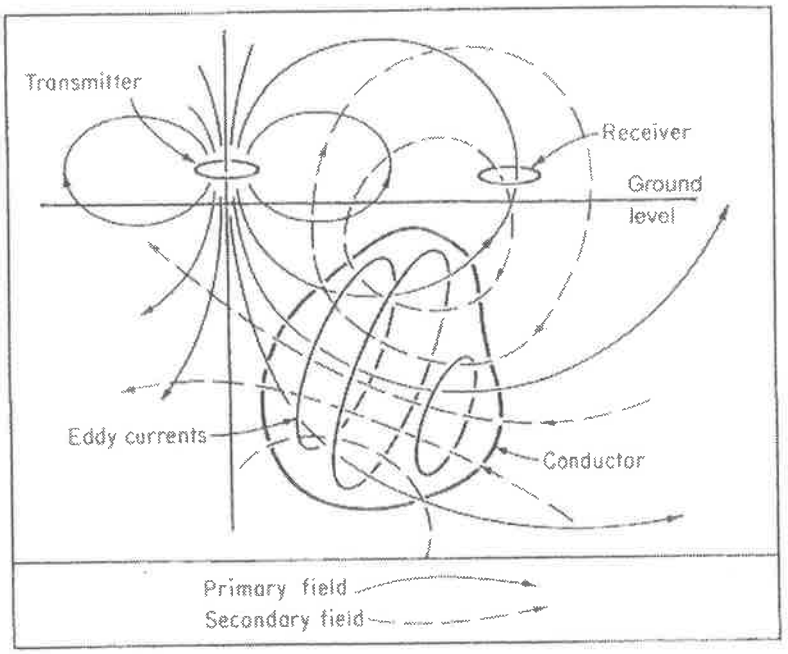

Figure 2.2: Relationship between the transmitter loop, primary magnetic field, eddy currents in earth conductors, secondary field and the receiver loop in EM systems (after Reynolds, 1997).

2.4.1 The Wave Equation

The propagation of EM waves in a homogenous and isotropic medium is defined by the wave equations for the electric and magnetic fields (Ward and Hohmann, 1988; Telford, 1990). These can be obtained by taking the curl of Equations 2.5 and 2.6, which become

$$\nabla\times(\nabla\times\mathbf{E}) = -\nabla\times\left(\frac{\partial\mathbf{B}}{\partial t}\right) \tag{2.22}$$

$$\nabla\times(\nabla\times\mathbf{H}) = \nabla\times\mathbf{J} + \nabla\times\left(\frac{\partial\mathbf{D}}{\partial t}\right) \tag{2.23}$$

and using the relations in 2.9,

$$\nabla\times(\nabla\times\mathbf{E}) = -\mu\nabla\times\left(\frac{\partial\mathbf{H}}{\partial t}\right) \tag{2.24}$$

$$\nabla\times(\nabla\times\mathbf{H}) = \sigma\nabla\times\mathbf{E} + \varepsilon\nabla\times\left(\frac{\partial\mathbf{E}}{\partial t}\right) \tag{2.25}$$

Provided that $\mathbf{E}$ and $\mathbf{H}$ are continuous with continuous first and second derivatives (i.e. there are no boundaries) then the operators $\nabla\times$ and $\partial/\partial t$ can be applied in the reverse order such that Equations 2.24 and 2.25 become

$$\nabla\times(\nabla\times\mathbf{E}) = -\mu\frac{\partial}{\partial t}(\nabla\times\mathbf{H}) \tag{2.26}$$

$$\nabla\times(\nabla\times\mathbf{H}) = \sigma\nabla\times\mathbf{E} + \varepsilon\frac{\partial}{\partial t}(\nabla\times\mathbf{E}) \tag{2.27}$$

Now Equations 2.5 and 2.6 can be used to replace $\nabla\times\mathbf{E}$ and $\nabla\times\mathbf{H}$ arriving at

$$\nabla\times\nabla\times\mathbf{E} = -\mu\frac{\partial^2\mathbf{D}}{\partial t^2} - \mu\frac{\partial\mathbf{J}}{\partial t} \tag{2.28}$$

$$\nabla\times\nabla\times\mathbf{H} = -\varepsilon\frac{\partial^2\mathbf{B}}{\partial t^2} - \sigma\frac{\partial\mathbf{B}}{\partial t} \tag{2.29}$$

and using Equations 2.9 we can write these in terms of only $\mathbf{E}$ and $\mathbf{H}$, giving

$$\nabla \times \nabla \times \mathbf{E} = -\varepsilon\mu \frac{\partial^2 \mathbf{E}}{\partial t^2} - \sigma\mu \frac{\partial \mathbf{E}}{\partial t} \tag{2.30}$$

$$\nabla \times \nabla \times \mathbf{H} = -\varepsilon\mu \frac{\partial^2 \mathbf{H}}{\partial t^2} - \sigma\mu \frac{\partial \mathbf{H}}{\partial t} \tag{2.31}$$

Rewriting Equations 2.7 and 2.8 in terms of **H** and **E** respectively (using Equation 2.9), in a source free region (such that q = 0) we have

$$\nabla \cdot \mathbf{H} = 0, \qquad \text{and } \nabla \cdot \mathbf{E} = \frac{q}{\varepsilon} = 0 \tag{2.32}$$

Finally, using this result and the vector identity $\nabla \times \nabla \times \mathbf{A} = \nabla\nabla \cdot \mathbf{A} - \nabla^2 \mathbf{A}$ with Equations 2.30 and 2.31 we have

$$\nabla^2 \mathbf{E} = \varepsilon\mu \frac{\partial^2 \mathbf{E}}{\partial t^2} + \sigma\mu \frac{\partial \mathbf{E}}{\partial t} \tag{2.33}$$

$$\nabla^2 \mathbf{H} = \varepsilon\mu \frac{\partial^2 \mathbf{H}}{\partial t^2} + \sigma\mu \frac{\partial \mathbf{H}}{\partial t} \tag{2.34}$$

These are the time-domain wave equations for the electric and the magnetic fields in a source free region.

The wave equations can be stated in the frequency domain using a Fourier transform (Ward and Hohmann, 1988) giving

$$\nabla^2 \mathbf{E} + (\mu\varepsilon\omega^2 - i\mu\sigma\omega)\mathbf{E} = 0 \tag{2.35}$$

$$\nabla^2 \mathbf{H} + (\mu\varepsilon\omega^2 - i\mu\sigma\omega)\mathbf{H} = 0 \tag{2.36}$$

which are easier to employ in the forward TEM problem (section 2.4.5)

2.4.2 TEM Field Propagation: The Diffusion Equation

For frequencies less than 10^5 Hz $\sigma\mu\frac{\partial \mathbf{E}}{\partial t} >> \varepsilon\mu\frac{\partial^2 \mathbf{E}}{\partial t^2}$ and $\sigma\mu\frac{\partial \mathbf{H}}{\partial t} >> \varepsilon\mu\frac{\partial^2 \mathbf{H}}{\partial t^2}$ in Equations 2.33 and 2.34 respectively (Ward and Hohmann, 1988). Under these circumstances we can ignore the double derivative terms giving the diffusion equations

$$\nabla^2 \mathbf{E} = \sigma\mu\frac{\partial \mathbf{E}}{\partial t} \tag{2.37}$$

$$\nabla^2 \mathbf{H} = \sigma\mu\frac{\partial \mathbf{H}}{\partial t} \tag{2.38}$$

This derivation of the diffusion equation is equivalent to ignoring the displacement current term in Equation 2.6. At low frequencies (long wavelengths) the EM field responds to the macroscopic properties (principally conductivity) of broad regions as the field spreads throughout the subsurface and is described by the Diffusion equation. In contrast, high frequency (short wavelength) electromagnetic interactions behave more like propagating wavefronts, interacting (refracting, diffracting and reflecting) at boundaries and the diffusion equation is insufficient to describe such interactions.

The diffusion equations are simplified by considering them in one dimension (in this case the vertical direction, since we most commonly measure the vertical field quantities)

$$\frac{\partial^2 \mathbf{E}}{\partial z^2} - \sigma\mu\frac{\partial \mathbf{E}}{\partial t} = 0 \tag{2.39}$$

$$\frac{\partial^2 \mathbf{H}}{\partial z^2} - \sigma\mu\frac{\partial \mathbf{H}}{\partial t} = 0 \tag{2.40}$$

These are second order linear differential equations which can be solved for homogenous subsurface regions in either the time domain or the frequency domain (Ward and Hohmann, 1988).

2.4.3 Solutions for the Diffusion Equation

The solution that applies to an impulse (delta function) electric and magnetic field at depth $z = 0$ (i.e. a TEM transmitting loop on the Earth's surface) is stated by Ward and Hohmann (1988) as

$$\begin{pmatrix} \mathbf{E} \\ \mathbf{H} \end{pmatrix} = \begin{pmatrix} \mathbf{E}_0^+ \\ \mathbf{H}_0^+ \end{pmatrix} \frac{(\mu\sigma)^{1/2} z}{2\pi^{1/2} t^{3/2}} e^{-\mu\sigma z^2 / 4t} \tag{2.41}$$

where $\mathbf{E}_0^+$ and $\mathbf{H}_0^+$ are the values at t = 0. This function explains the behaviour of the primary EM field and is shown graphically in Ward and Hohmann (1988 – page 140).

For a particular depth beneath the transmitter, the electric and magnetic fields increase with time from zero to a maximum at time

$$t_{max} = \frac{\mu\sigma z^2}{6} \tag{2.42}$$

This can be derived by solving for t when the time derivative of Equation 2.41 is set to zero. For highly conductive regions, the maximum field strength occurs at later time than for resistive regions, demonstrating that decay of the measured secondary field is slower for conductive features.

Similarly for a particular finite time after the impulse, the electric and magnetic field strengths have a maximum at a depth found by solving for z when the vertical derivative of Equation 2.42 is set to zero

$$z_{max} = \left(\frac{2t}{\mu\sigma} \right)^{1/2} \tag{2.43}$$

This equation is considered the penetration depth of a primary field for TEM surveys, and is a similar concept to the skin depth in the frequency domain.

A qualitative understanding of the nature of the induced eddy currents can be gained from graphs of Equation 2.41. Eddy currents are initially only near-surface effects (small z_{max} for early t), but are generated at greater depth with increasing time after the primary signal. Figure 2.3 illustrates this time dependence of the eddy currents due to the diffusion of EM fields (Nabighian and Macnae, 1991; Reynolds, 1997).

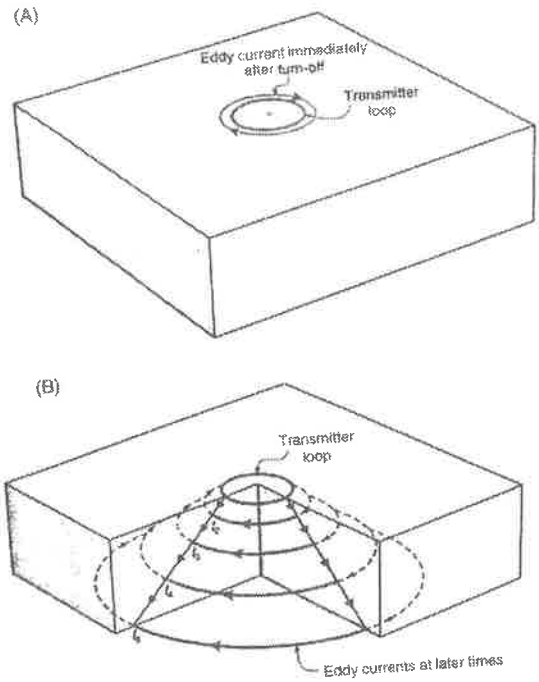

Figure 2.3: Eddy currents generated beneath a TEM transmitter loop at early time (A) and at greater time after current turn-off (B). This shows how the TEM signal deepens and broadens with time (after Reynolds, 1997).

2.4.4 Boundary Conditions

Equation 2.41 is the solution for electromagnetic fields at low frequencies (less than 10^5 Hz) in a homogenous region of the subsurface, but does not allow for regions where boundaries or gradients in conductivity exist. Any complete solution to the diffusion equation must meet certain conditions, defining how the fields behave on all boundaries within the problem (Telford et al., 1990). In the following boundary conditions, **n** is a unit vector that is normal to an interface between two media with different conductivity.

Tangential E: The tangential component of the electric field **E** is continuous across all boundaries,

$$\mathbf{n}\times(\mathbf{E}_1-\mathbf{E}_2)=0 \tag{2.44}$$

which means the tangential component of current density $\mathbf{J} = \sigma\mathbf{E}$ is discontinuous across boundaries.

Tangential H: The tangential component of magnetic field intensity **H** is continuous across all boundaries,

$$\mathbf{n}\times(\mathbf{H}_1-\mathbf{H}_2)=0 \tag{2.45}$$

which means the tangential component of magnetic flux density $\mathbf{B} = \mu\mathbf{H}$ is discontinuous across boundaries.

Normal E: The normal component of current density $\mathbf{J} = \sigma\mathbf{E}$ is continuous across all boundaries,

$$\mathbf{n}\cdot(\sigma_1\mathbf{E}_1-\sigma_2\mathbf{E}_2)=0 \tag{2.46}$$

which means the normal component of electric field $\mathbf{E}$ is discontinuous across boundaries.

Normal H: The normal component of the magnetic flux density $\mathbf{B} = \mu\mathbf{H}$ is continuous across all boundaries,

$$\mathbf{n}\cdot(\mu_1\mathbf{H}_1-\mu_2\mathbf{H}_2)=0 \tag{2.47}$$

which means the normal component of magnetic field intensity $\mathbf{H}$ is discontinuous across boundaries.

A solution is determined by satisfying each of these boundary conditions between all homogenous sub-regions in the problem. In this manner, EM fields can be described in any Earth model. Usually a layered Earth model is used, with boundary conditions being matched at the interface of each layer, and at the half-space surface.

2.4.5 The Forward Problem

The mutual impedance of a TEM system is defined by the ratio of the voltage induced in the receiver to the current in the transmitter and is a function of ground resistivity structure and the array properties (including dimensions and the current turn-off ramp duration). For a layered Earth model, the mutual impedance for a central, circular receiver-loop in the frequency domain is given by Raiche (1984) and Sandburg (1990) as

$$Z(\sigma,t)=\frac{\pi\mu a}{2\delta}\frac{A_R}{A_T}\int_0^\infty G(\xi^2\tau,P)\mathrm{J}_1(\xi)\xi\mathrm{d}\xi \tag{2.48}$$

which is an inverse Hankel transform of the Greens function G, where a is the transmitter loop radius, δ is the ramp time (assuming a linear turn-off ramp), A_R and A_T are the receiver and transmitter areas (respectively), ξ is the inverse Hankel transform operator and J_1 is a Bessel function of order 1. Function G takes the form

$$G(\xi^2\tau, P) = F(\xi^2\tau') - F(\xi^2\tau) \tag{2.49}$$

where $$\tau' = \frac{t}{\sigma\mu a^2} \tag{2.50}$$

$$\tau = \frac{t+\delta}{\sigma\mu a^2} \tag{2.51}$$

and P contains the Earth model information. For the layered earth case function F takes the form

$$F(\xi^2\tau) = -\mathrm{L}_q^{-1}\left[\frac{A_0(q)}{q}\right] \tag{2.52}$$

where L_p^{-1} is the inverse Laplace transform operator with respect to p, the transform pair is $(q, \xi^2\tau)$ and A_0 is the layered Earth impedance function. The expression of q is

$$q = \frac{-i\omega\sigma\mu a^2}{\xi^2} \tag{2.53}$$

where ω is the angular frequency and i is $\sqrt{-1}$. Calculating Equation 2.48 for a large range of frequencies and taking the inverse Fourier transform of the resulting discrete function gives the solution in the time-domain. Smith and Paine (1999) show that this method is most accurate at the early times, where fewer frequencies per decade are required in the Fourier transform. Also, removing high frequencies from the transform introduces errors at early times, while removing low frequencies introduces late-time errors. Equation 2.48 can be used for square loop geometries by using the radius for the equivalent area circular loop. However, Smith and Paine (1999) show analytically that this approximation is not suitable for early time measurements.

2.5 Forward Modelling

2.5.1 DC Resistivity Forward Models

In order to investigate the effect of a conductive shallow water channel in a more resistive halfspace on the DC Resistivity response, three-dimensional forward modelling was carried out using a code called Resim3D (Zhou and Greenhalgh, 2001).

First the recorded voltage (normalised by current) was calculated for each receiving dipole for a dipole-dipole survey configuration with a = 1 m and n = 2 to 17 over a homogenous 50 ohm.m halfspace. The value 50 ohm.m was chosen based on measured river water resistivity (approximately 16 ohm.m) and estimated near surface sediment porosity (between 50% and 60%) using Archie's Law (Equation 2.4). The homogenous model was compared to models in which resistivity of a 1 m thick layer was increased by 1%. The difference between the voltage calculated for each dipole before and after the resistivity increase (normalised by the homogenous model value) were plotted at the depth of the altered layer. The resulting graph (Figure 2.4) shows a curve of sensitivity (to small resistivity increases) for each dipole-spacing. For small dipole spacings (n = 2) the maximum sensitivity occurs at approximately 1 m depth, and has virtually no sensitivity below 4 m depth. For larger dipole spacings (n = 17) the sensitivity peak is smaller but broader, and has a maximum at approximately 4 m depth. These are consistent with depth of investigation for the dipole-dipole array, defined by roy and Apparao (1971) as the depth at which a thin horizontal layer of ground contributes the maximum amount to the measured resistivity, being approximately one fifth the array size (Roy and Apparao, 1971; Apparao, 1991). Edwards (1977) and Merrick (1997) have also discussed the effective depth of dipole-dipole array measurements.

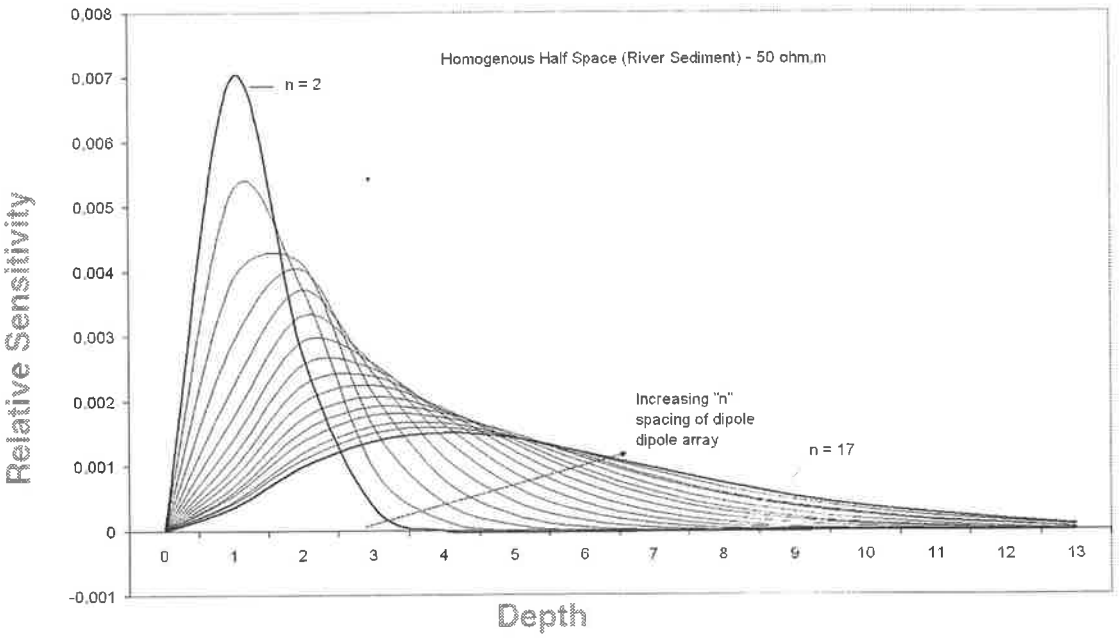

Figure 2.4: Sensitivity curves for dipole size a = 1 m, and dipole numbers n = 2 – 17 for a 50 ohm.m homogenous halfspace. As dipole number increases sensitivity peak becomes smaller and broader.

The same method was used to calculate depth sensitivity curves for a two-layer model with a 16 ohm.m, 5 m deep water layer above a 50 ohm.m halfspace. Figure 2.5 shows that the introduced conductive layer dominates the current flow. Compared to the homogenous halfspace, sensitivity is slightly increased for most dipoles in the top 5 m, but falls away quickly as depth increases into the more resistive sediments. In this model, all dipoles are more sensitive to changes in the conductive water layer than the resistive sediment layer.

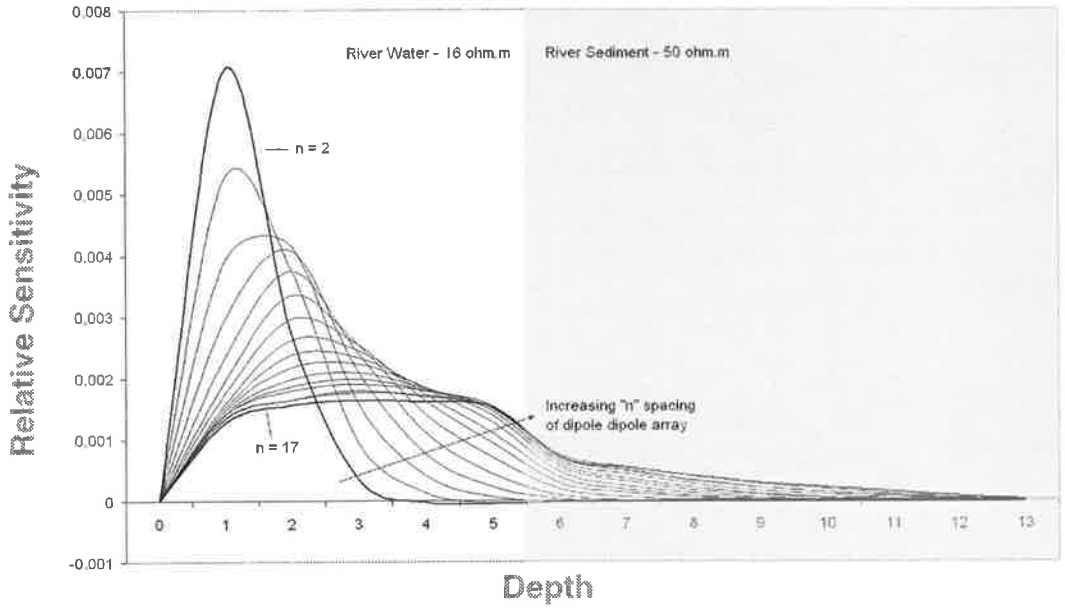

Figure 2.5: Sensitivity curves for dipole size a = 1 m, and dipole numbers n = 2 – 17 for a 50 ohm.m homogenous half space overlain by a 5 m water (16 ohm.m) layer. Sensitivity of all dipoles reduces rapidly below the water-sediment boundary.

The next model change was to introduce river banks. A channel width of 10m was chosen, which is narrower than is likely to be encountered on the Murray River (which is on the order of 100-200 m wide). The narrow channel was chosen to investigate the worst case scenario, which might be appropriate for studies of smaller channels. Figure 2.6 shows that introducing the resistive riverbanks slightly increases the array's sensitivity to the conductivity of the uppermost sediments. This is because there is less of a conductive layer to dominate the current flow.

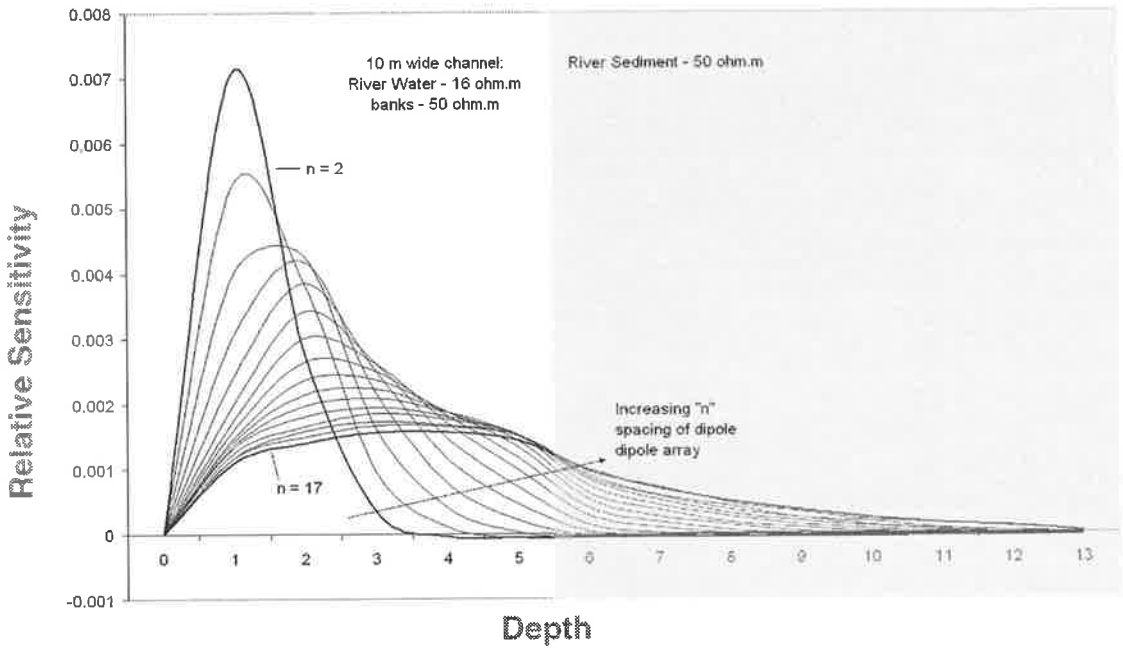

Figure 2.6: Sensitivity curves for dipole size a = 1 m, and dipole numbers n = 2 – 17 for a 50 ohm.m homogenous half space containing a 5 m deep, 10 m wide water channel (16 ohm.m). Sensitivity of all dipoles reduces more smoothly across the water-sediment boundary.

Figure 2.7 shows the effect of increasing the dipole size from a = 1 to a = 5 m (maintaining dipole numbers 2 to 17). This is the first model to show more sensitivity to the sediments than the river water for at least some dipoles. This suggests that the scale of the dipoles needs to be similar to or larger than the expected depth of the river water for a survey system to be sensitive to salinity changes in the top few metres of river sediments rather than the water column. This is further supported by Figure 2.8, which shows a reduced water depth to 2m. In this model all but the smallest dipole number shows more sensitivity to the sediment than the water.

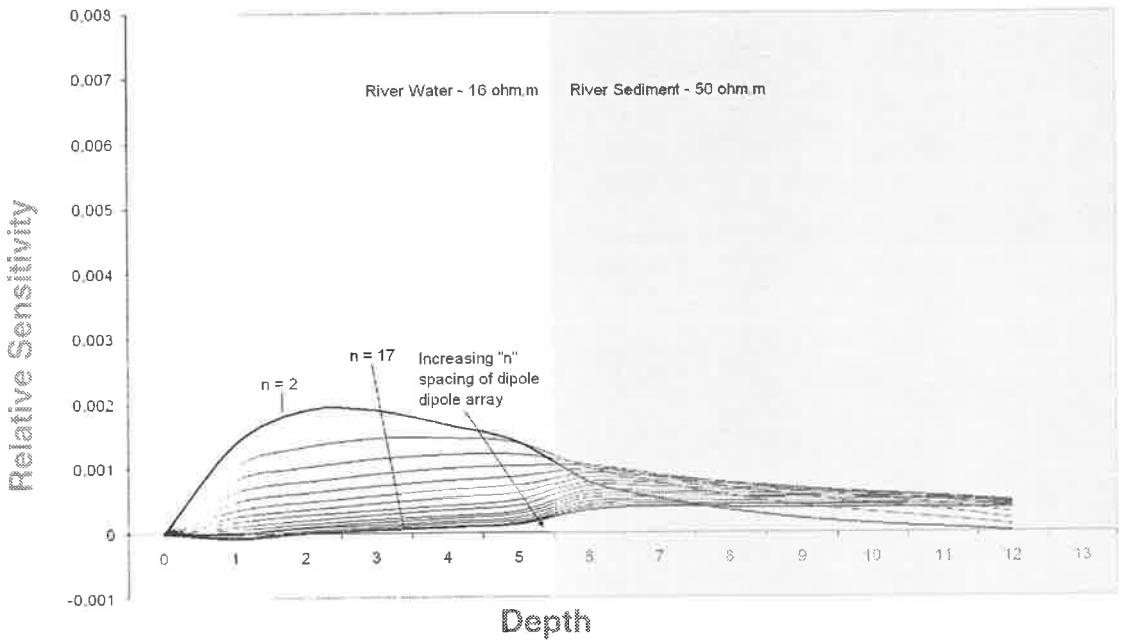

Figure 2.7: Sensitivity curves for dipole size a = 5 m, and dipole numbers n = 2 to 17 for a 50 ohm.m homogenous half space containing a 5 m water (16 ohm.m) layer. Increasing the dipole size has reduced the relative sensitivity of all dipoles, however the sensitivity of larger dipoles (n = 10 – 17) is greater in the sediments than in the water channel.

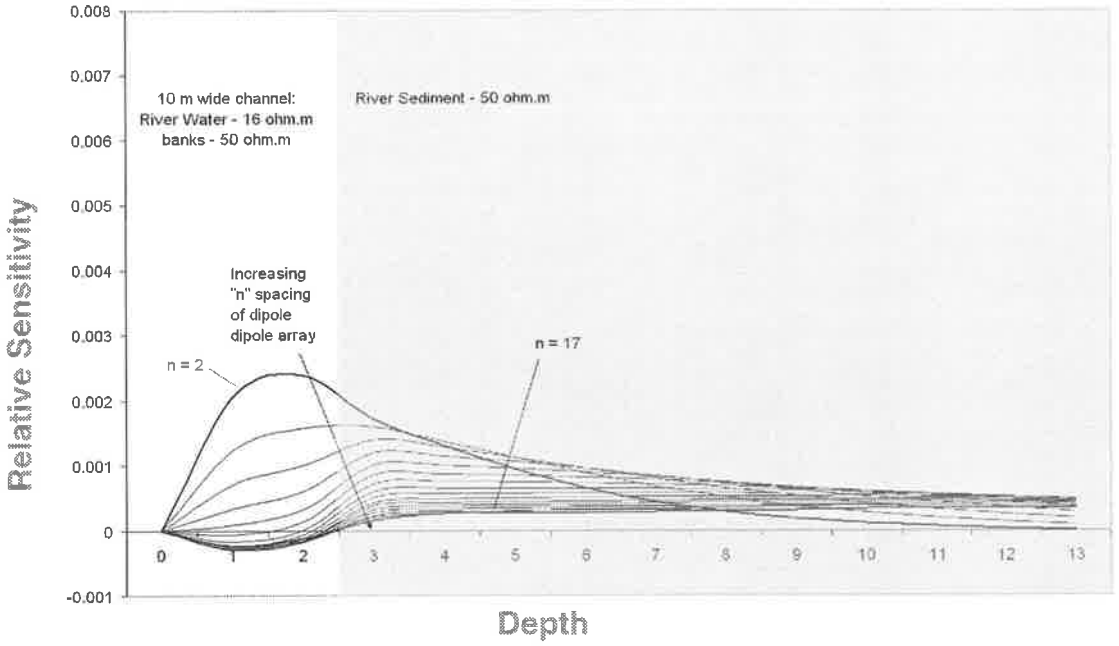

Figure 2.8: Sensitivity curves for dipole size a = 5 m, and dipole numbers n = 2 – 17 for a 50 ohm.m homogenous half space containing a 2 m deep, 10 m wide water channel (16 ohm.m). Decreasing the water depth has had the effect of making the sensitivity of all dipoles from n = 4 – 17 greater in the sediments than in the water column.

2.5.2 TEM Forward Models

The smooth modelling program STEMINV (MacInnes and Raymond, 2001a) was used as part of a sensitivity analysis for the TEM system to improve choice of inversion characteristics and aid interpretation processes. STEMINV is a one dimensional inversion package (assumes infinite horizontal layers) that can create two dimensional figures by stitching (and contouring) adjacent models. The program simultaneously minimises model roughness and misfit criteria. Smoothness of the final model is dependant on the user controlled smoothness constraint which determines the relative importance of minimising roughness compared to misfit in the inversion. For sensitivity analysis, single-station models were defined using various configurations of 16 ohm.m river water, 50 ohm.m freshwater saturated sediments (assuming porosity between 50% and 60%), a conservative conductive value at 10 ohm.m (for example 6,000 mg/L saline water in sand) and a very conductive value of 0.5 ohm.m (equivalent to 27,000 mg/L saline water in a sediment with some conductive clay content). These values have been chosen based on Archie's Law (Equation 2.4).

The forward response for these models was calculated using STEMINV by setting the number of inversions to zero, with the required model set as a starting model for the inversion. The output response was then inverted using the same program. Noise estimates were not added to the response, so the inversions are more accurate then we would expect from real data (particularly at depth).

Where 5 m of river water overlies very conductive sediments (Figure 2.9a), the results indicate that the location of the boundary corresponds approximately with the inflection point on the inverted model. This figure also shows that the inverted model tends to oscillate about the conductive value with depth. This instability can be reduced by increasing the smoothness constraint in the inversion (Figure 2.9b), but this reduces the resolution of the boundary depth. If gradational boundaries are encountered, the smooth inversion is much more successful at reproducing the original model (Figure 2.10). While a smooth boundary is not expected at the water-sediment interface, most other resistivity changes encountered in this project are likely to be gradual. Figure 2.11 shows that when a 5 m thick resistive layer occurs at a depth of 5 m, the resistivity value is significantly underestimated. In contrast, the resistivity value of a conductive layer of the same thickness is well determined, except that resistivity is too high both above and below the

conductive layer (Figure 2.12). In both the resistive layer and the conductive layer case, smoothing has been applied and the inverted model is much broader than the true layer thickness, having a half-width of almost 10 m. When smoothing is reduced, the definition of layer thickness becomes more accurate (Figure 2.13). The half-width for this model is only slightly more than 5 m. Finally, for a boundary at 10 m depth, the value of the lower layer is reached by the smooth model at some depth below the actual boundary. For a conductive lower layer the value is reached much sooner than for a resistive lower layer (Figure 2.14). The two models in Figure 2.14 also show that the oscillation about the value of the lower layer is larger for a conductive region than for a resistive region.

From this study, we have established a list of guidelines for successful interpretation of STEMINV inverted data

1. Smoothing criteria provide better constraints on lower layer resistivities (by stabilising the oscillations of the model with depth);

2. Where sharp or rapid resistivity changes are expected (e.g. water-sediment boundary) the smoothing criterion reduces the resolution of the boundary;

3. Where gradual resistivity changes are expected (e.g. most hydrology related changes) the estimate of resistivity can be very close to the true resistivity, regardless of smoothing criteria; and

4. The resistivity of conductive layers is more accurately determined than that of resistive layers (which are underestimated).

The smoothness constraint will be used in this project to attempt to stabilise resistivity at depth. Inversions should also be made with the smoothness factor reduced because the water-sediment boundary (specifically the resistivity immediately below this boundary) are of critical importance in this study. Ideally, a graduated smoothness function could be applied, so that in the top 10-15m, where a sharp resistivity boundary is expected, minimal smoothing can be applied, while at depth, where resistivity should vary more slowly, smoothing can be used to stabilise the model.

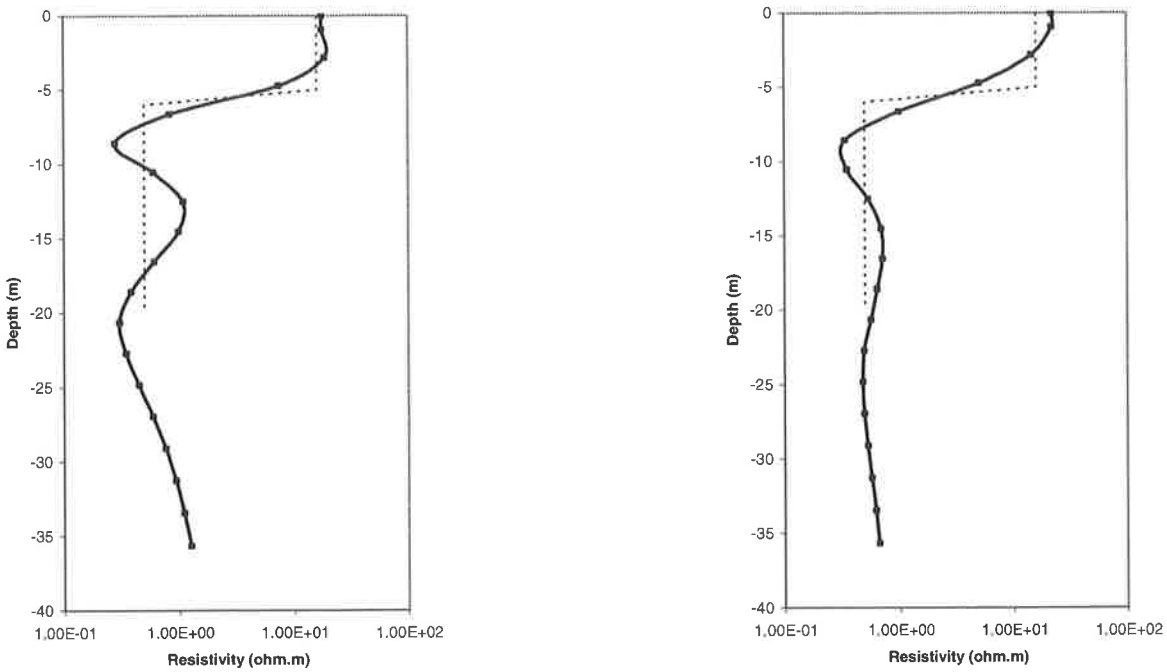

Figure 2.9: A step down in resistivity at 5 m depth from 16 ohm.m to 0.5 ohm.m with a smoothing factor of 1.0 (a) and with a smoothing factor of 3.0 (b). The smoothing criterion reduces the fluctuation with depth about the low resistivity value.

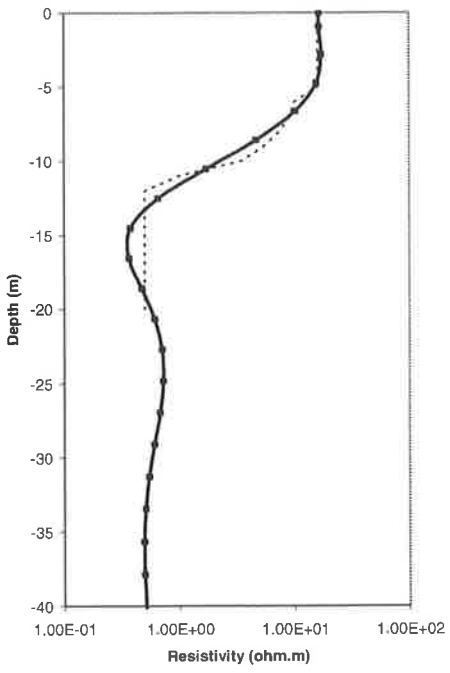

Figure 2.10: When the step down in resistivity is a gradual or smooth feature, the inversion fits very closely (compare to Figure 2.10)

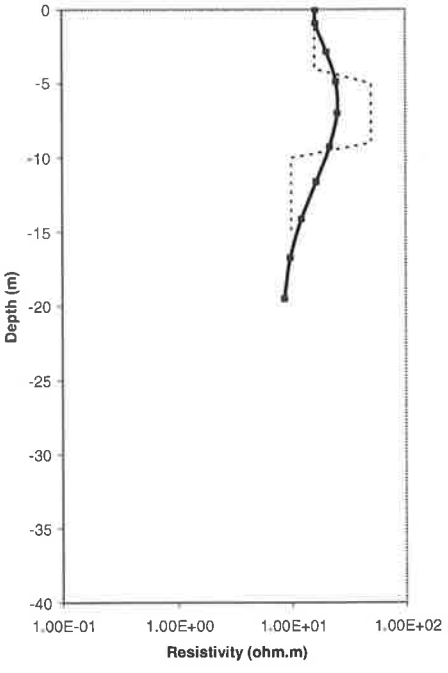

Figure 2.11: A 5 m thick layer step up in resistivity from 16 ohm.m to 50 ohm.m is only poorly detected by the inversion. The resulting peak is broader and only half the true resistivity

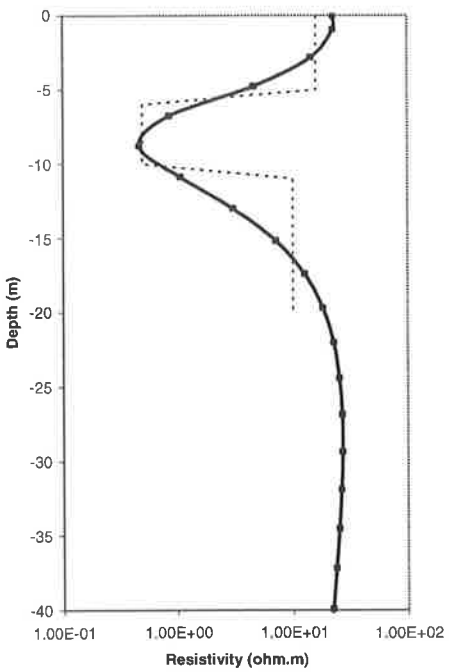

Figure 2.12: The peak produced by the inversion of a 5 m thick step down in resistivity from 16 ohm.m to 0.5 ohm.m shows the correct value, but is much broader than the layer thickness.

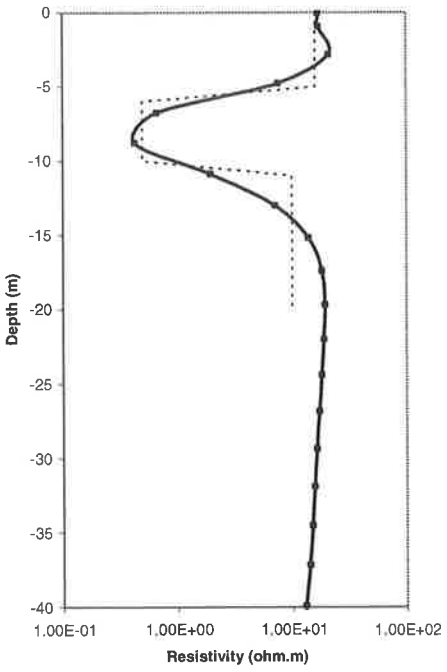

Figure 2.13: The peak produced by the inversion of the same conductive layer as in Figure 4.12 more closely defines layer thickness when smoothing is reduced in the inversion.

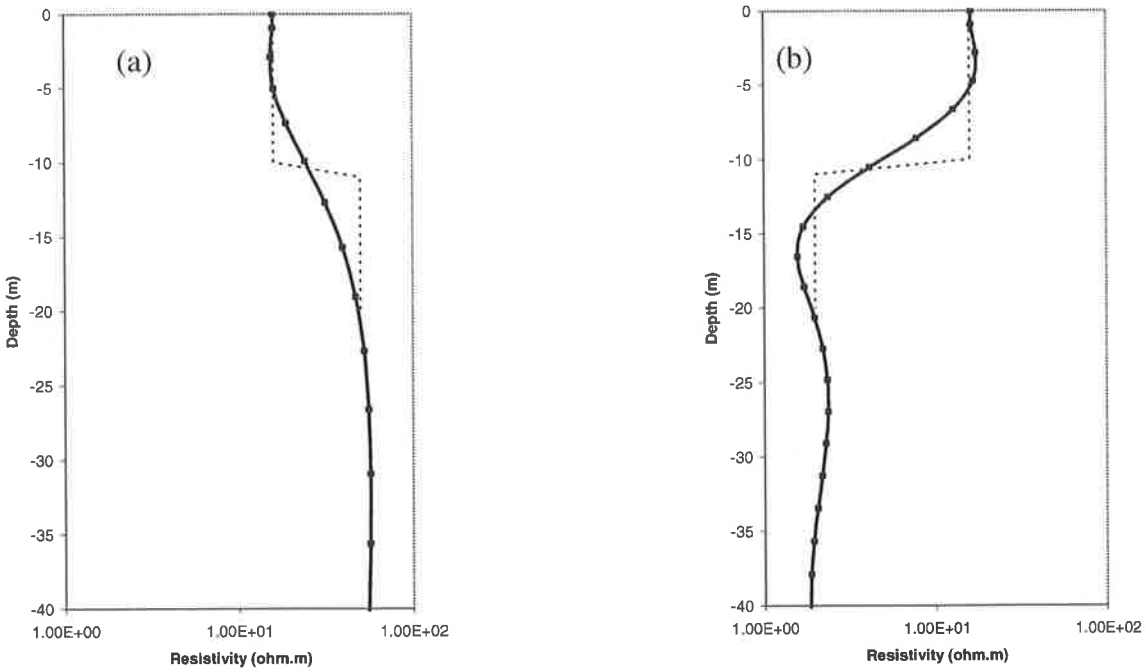

Figure 2.14: A comparison between (a) a step up in resistivity from 16 ohm.m to 50 ohm.m (0.5 orders of magnitude difference) and (b) a step down in resistivity from 16 ohm.m to 2 ohm.m (0.9 orders of magnitude). The full resistivity value beneath the boundary is not reached in model A until about 20m depth, where as in model (b) the full value is reached by 14 m depth.

Chapter 3

Methods

3.1 DC Resistivity

3.1.1 Array Design

DC Resistivity profiling was undertaken using a floating array called the 'Blue Eel' (Allen and Merrick, 2003). The Blue Eel is constructed from lengths of layflat tubing separating variably spaced electrodes. The entire array is inflated so that it floats at the river surface. The current electrode dipole was 10 m and was approximately 10 m behind the boat. Potential electrode pairs were at n = 1 to 5 for 5 m potential dipoles, n = 3 and 4 for 10 m potential dipoles and n = 2.5 and 3.5 for 20 m potential dipoles, where n is the current dipole - potential dipole spacing in multiples of the potential dipole size (Figure 3.1). This made an array that was 100 m long (giving depth of investigation of approximately 20m; Apparao, 1991). The array was originally designed to be up to 150m in length, however damage occurred due to snagging of the array, resulting in the unknown breakage of an internal wire (and the towing of 50 m of redundant tubing). The array has been used in continuous multi-channel logging mode with a Zonge GDP32 16 channel receiver and a Zonge ZT30 transmitter with an input voltage booster. The system provided only 1 Amp at 100 V, as it was thought that higher input currents would result in shorter battery life, limiting the duration of the survey. However, battery life problems were not encountered. The potential difference at each potential pair was simultaneously read every 4 seconds. Travelling at 10-12 km/hr with this sampling rate gave a horizontal resolution of approximately 12m. Figure 3.2 shows the Blue-Eel in operation and Figure 3.3 shows the equipment before deployment.

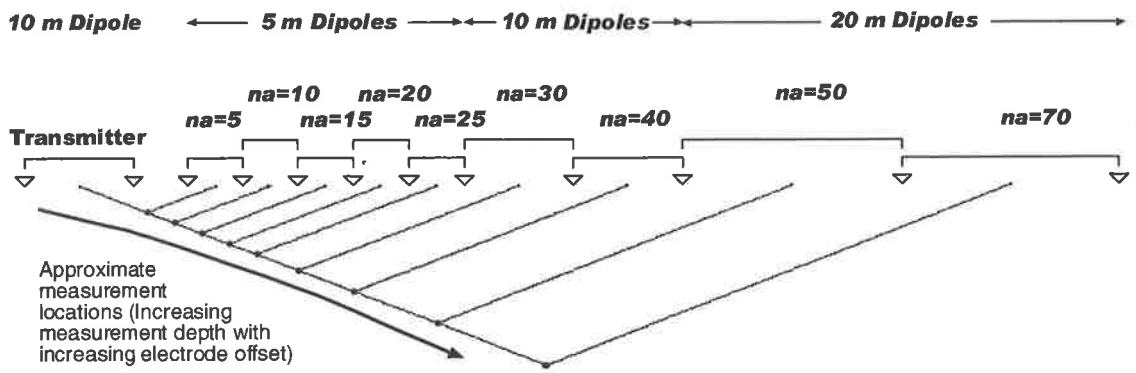

Figure 3.1: Electrode configurations for The Blue Eel DC Resistivity profiling array. Transmitter dipole size is a constant 10 m. Receiver dipole size varies with electrode offset. The term *na* corresponds to inner electrode offset in metres.

Figure 3.2: (left) Blue Eel in tow on the Murray River. The inflated array can be seen extending 150m behind the boat.

Figure 3.3: (below) Blue Eel array ready for deployment. Labelled are the potential and current electrodes. (Image courtesy Allen and Merrick, 2003)

3.1.2 Survey Parameters

DC Resistivity data were acquired in late August 2002, near Waikerie, South Australia. Approximately 54km of data (27km in each direction) were acquired from river km 366 to 393 (Figure 3.4). This included parts of the river where no interception scheme was operating and high salt-loads are known to exist ("unpumped section": 366km to 376km), and covered the part of the Waikerie SIS ("pumped section": 376km to 393km). Water depth varied between 2 m and 14 m, being deepest on the outside of river bends

(particularly those that correlate with cliff faces) and shallowest in the middle of straight stretches of river. GPS data were recorded from a Garmin handheld GPS unit (accurate to approximately 5 m) located on the boat. Water depth was measured at one minute intervals from an echo sounder, which corresponds to approximately 150-200 m between depth measurements - sufficient to identify such large scale variations. Small scale variations such as trenches and bars on 10-20 m wavelength scales were observed (but not recorded) on the echo sounder. Similarly, an onboard EC meter was observed but not logged with the data, because minimal variation occurred.

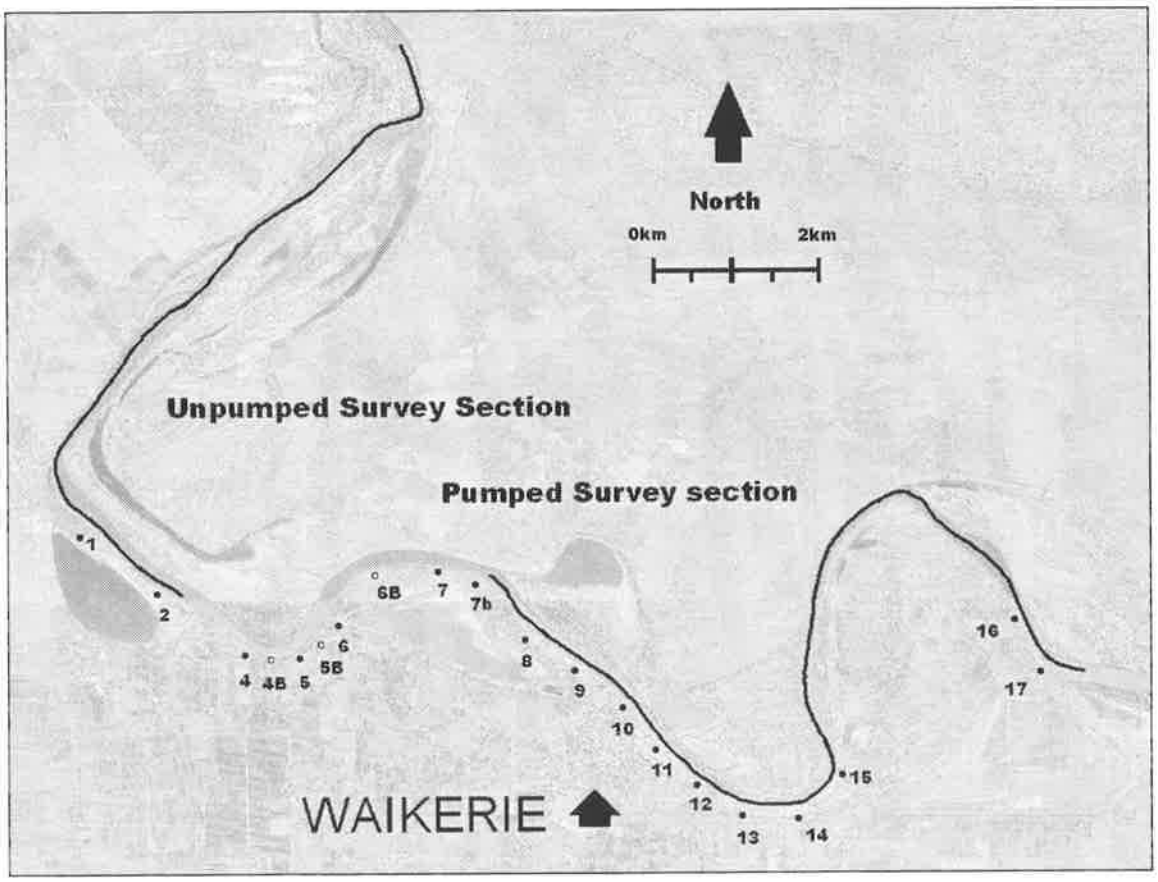

Figure 3.4: Location map for the two DC Resistivity survey lines. The Waikerie SIS production bores are labelled.

3.1.3 Processing

Electrode locations were determined by resampling from the GPS path (boat travel path) at appropriate offsets from the boat. This assumes that the array follows the exact path of the boat. The Blue Eel array appeared to follow the boat path on most river corners. Errors due to this assumption would be more significant in the larger dipole spacings (deeper data).

GPS electrode locations were merged with depths and voltages using time as a linking field (Allen and Merrick, 2003).

The program TS2DIP (MacInnes and Raymond, 2001b) was used to create smooth two dimensional models. Two dimensional modelling required approximately 10 minutes per km of data, however the surveys must be separated into short (approx 1km) overlapping models, which can be merged later.

The model files produced by the inversion program were gridded using Geosoft Corporation's Oasis Montaj Earth Science Mapping and Interpretation package. Figures produced with this program were gridded with either easting or northing as the horizontal ordinate. Consequently, the sections are effectively compressed where the survey line is oblique to the gridding direction. Furthermore, borehole locations (which are also plotted according to their easting or northing) do not always correspond with the model's point of closest approach. A description of the gridding techniques used to generate three dimensional figures appears in Appendix A.

3.2 Time-Domain Electromagnetics

3.2.1 Array Design

The TEM array was a floating deployment of the Zonge Engineering and Research Organisation's ground-based NanoTEM system (Hatch et al., 2002, Barrett et al., 2002). We used a 7.5 m x 7.5 m single-turn square transmitter loop, with a 3.0 amp square wave source and a central 2.5 m x 2.5 m single-turn square receiver loop (Figure 3.5). Construction of the TEM array required a trade-off between weight and stability. The frame was constructed from timber and strengthened using fibre-tape and diagonal ropes. Floatation was achieved using tyre inner tubes. An effort was made to minimise the metal content of the frame. To this end, nylon bolts were used in the construction of the timber frame. Metal valves in each of the eight inner tubes were thought to have a negligible effect. The frame was towed 10 m behind the boat. Towing speed was kept as low as possible, at about 3 km/hr, to minimise strain and vibration on the array. Figures 3.6, 3.7 and 3.8 show images of the array in construction and during operation.

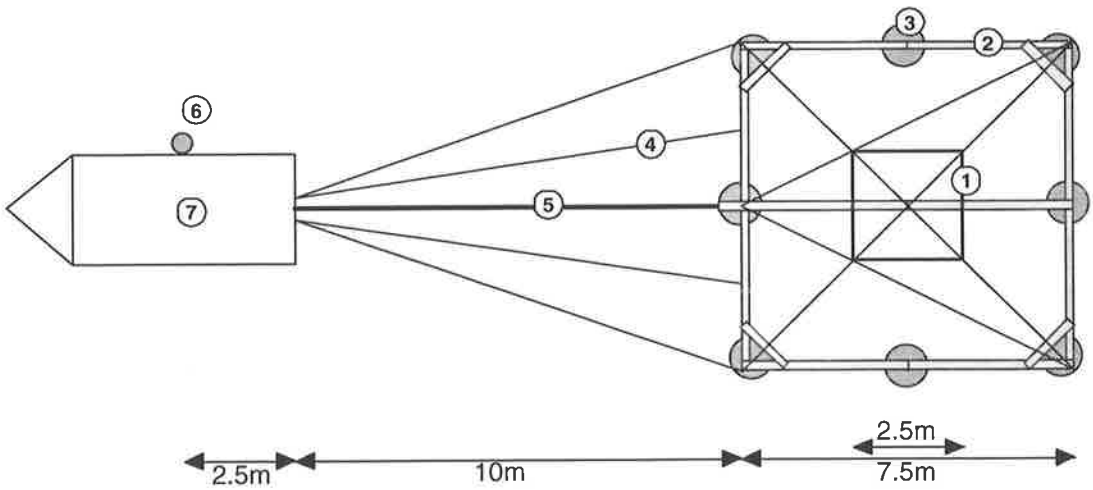

Figure 3.5: Floating deployment of the Zonge NanoTEM. Labelled are (1) receiver loop, (2) transmitter loop, (3) tyre inner tubes, (4) tow ropes and diagonal support ropes, (5) 10 m spacer and cable housing, (6) GPS and echo sounder units and (7) the boat.

Figure 3.6: Image of the floating TEM array during construction

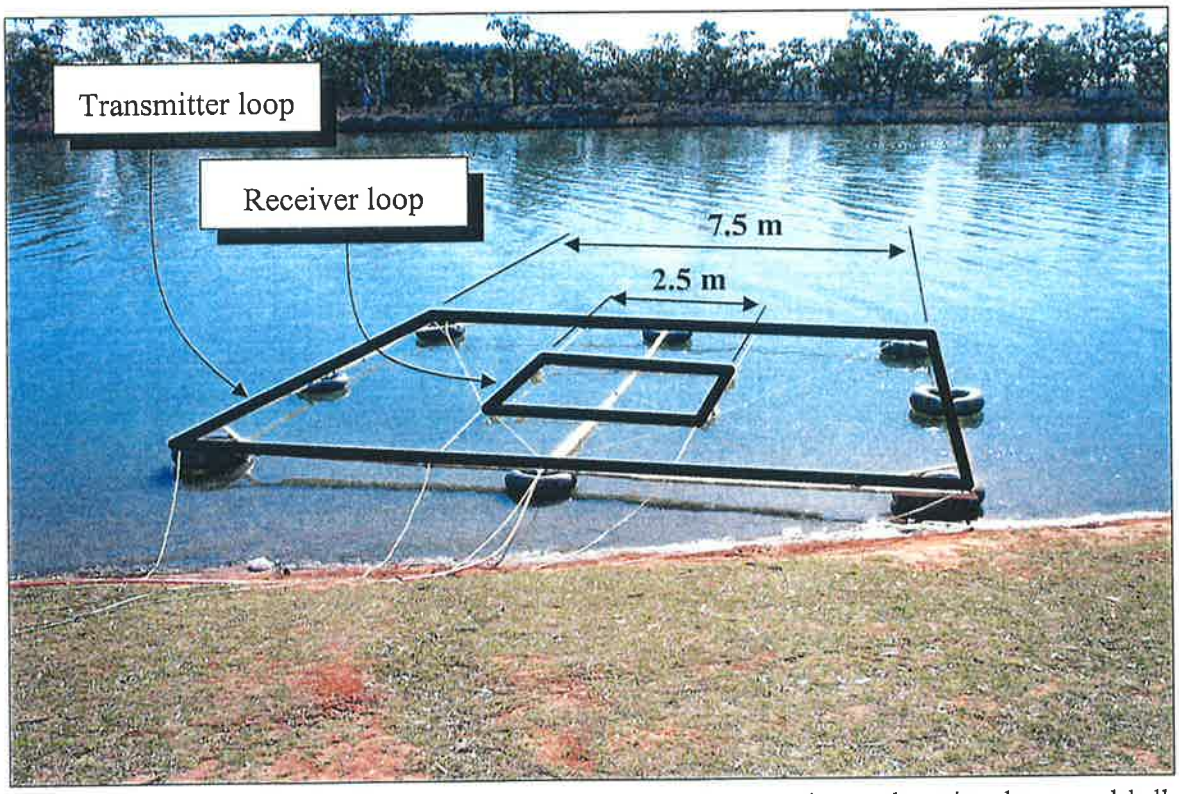

Figure 3.7: Image of floating the TEM array after deployment. Transmitter and receiver loops are labelled with their dimensions marked

Figure 3.8: Floating TEM array during data acquisition. The array is 10m behind the boat and towing speed is approximately 3 km/hr

3.2.2 Survey Parameters

The transmitter turn-off ramp was 1.8 μs. Other delays that were incorporated into the measurements were an anti-aliasing filter delay (1 μs) and a receiver antennae delay (1.5 μs). This gave a total required delay of 4.3 μs. Sampling interval was 1.6 μs, so the first multiple of the sampling interval that is larger than the required delay time is 3 x 1.6 = 4.8 μs, which corresponds to time of the first data measurement, with time origin at the start of the turn-off. Time origin is more commonly set to the end of all delays (4.3 μs after transmitter turn-off begins). Accordingly, the first window time is found by subtraction: 4.8 - 4.3 = 0.5 μs. Early time windows are one data point wide (at the sampling rate of 1.6 μs), but later time windows are an average of an increasing number of samples (determined by the window width). Table 3.1 lists the time after turn-off for the central sample and the number of samples (window width) for each window. The approximate signal depth for each window was calculated for half-space resistivities of 2 ohm.m, 16 ohm.m and 50 ohm.m (using Equation 2.43).

For each station, 64 soundings were stacked at 32 Hz and sampled at intervals of 1.6 μs, with the final time window (channel 31) recorded at 2.5 ms. However, all data after approximately the 15th time window (64μs) were discarded due to poor signal-to-noise ratio. Remaining data provided information to approximately 25m depth.

Window	Window Centre Time (μs)	Window Width (samples)	Depth (m) if 2 ohm.m half-space	Depth (m) if 16 ohm.m half-space	Depth (m) If 50 ohm.m half-space
1	0.519	1	1.3	3.6	6.4
2	2.125	1	2.6	7.4	13.0
3	3.371	1	3.3	9.3	16.4
4	5.337	1	4.1	11.7	20.6
5	6.943	1	4.7	13.3	23.5
6	8.55	1	5.2	14.8	26.1
7	10.93	2	5.9	16.7	29.5
8	14.15	2	6.7	19.0	33.6
9	17.36	2	7.4	21.0	37.2
10	21.36	3	8.2	23.3	41.2
11	26.17	3	9.1	25.8	45.6
12	32.48	5	10.2	28.8	50.8
13	41.28	6	11.5	32.4	57.3
14	51.69	7	12.8	36.3	64.1
15	64.44	9	14.3	40.5	71.6
16	80.43	11	16.0	45.3	80.0
17	101.1	15	17.9	50.7	89.7
18	128.2	18	20.2	57.1	101.0
19	161.8	23	22.7	64.2	113.5
20	203.3	29	25.4	72.0	127.2
21	255.2	36	28.5	80.6	142.5
22	321.2	47	32.0	90.4	159.9
23	405.1	58	35.9	101.6	179.5
24	508.9	72	40.2	113.8	201.2
25	639.6	92	45.1	127.6	225.6
26	805.6	116	50.6	143.2	253.2
27	1014	145	56.8	160.7	284.1
28	1276	184	63.7	180.3	318.7
29	1607	231	71.5	202.3	357.6
30	2022	289	80.2	226.9	401.1
31	2547	369	90.0	254.7	450.2

Table 3.1: Window times, window durations (in samples) and effective penetration depth assuming 2, 16 and 50 ohm.m half-spaces. The sampling rate is 1.6 μs. For most inversions, windows 4 to 15 (non-shaded) were used.

The NanoTEM survey was undertaken in two separate trips. In August 2002, 9km were acquired between river km 376 and 386 (line 1). This stretch of the river is currently pumped by the Waikerie SIS (Bores 4 to 15) and is referred to as the "pumped" section (Figure 3.9). A sub-section of this data (river km 377 to 381) was measured again in December as a test of repeatability. In the latter survey, four survey lines were recorded (lines 4 to 7), each separated by approximately 50 m, to enable changes in the response

across the river to be observed. During the December survey, lines 2 and 3, close to each bank of the "unpumped" river stretch (river km 368 to 376) were also recorded (Figure 3.9). These surveys total approximately 40km of data, which was acquired in a total of approximately 15 hours. As for the DC Resistivity surveys, GPS locations were recorded with a Garmin handheld GPS unit located on the boat, while water depth was recorded at one minute intervals from an echo sounder.

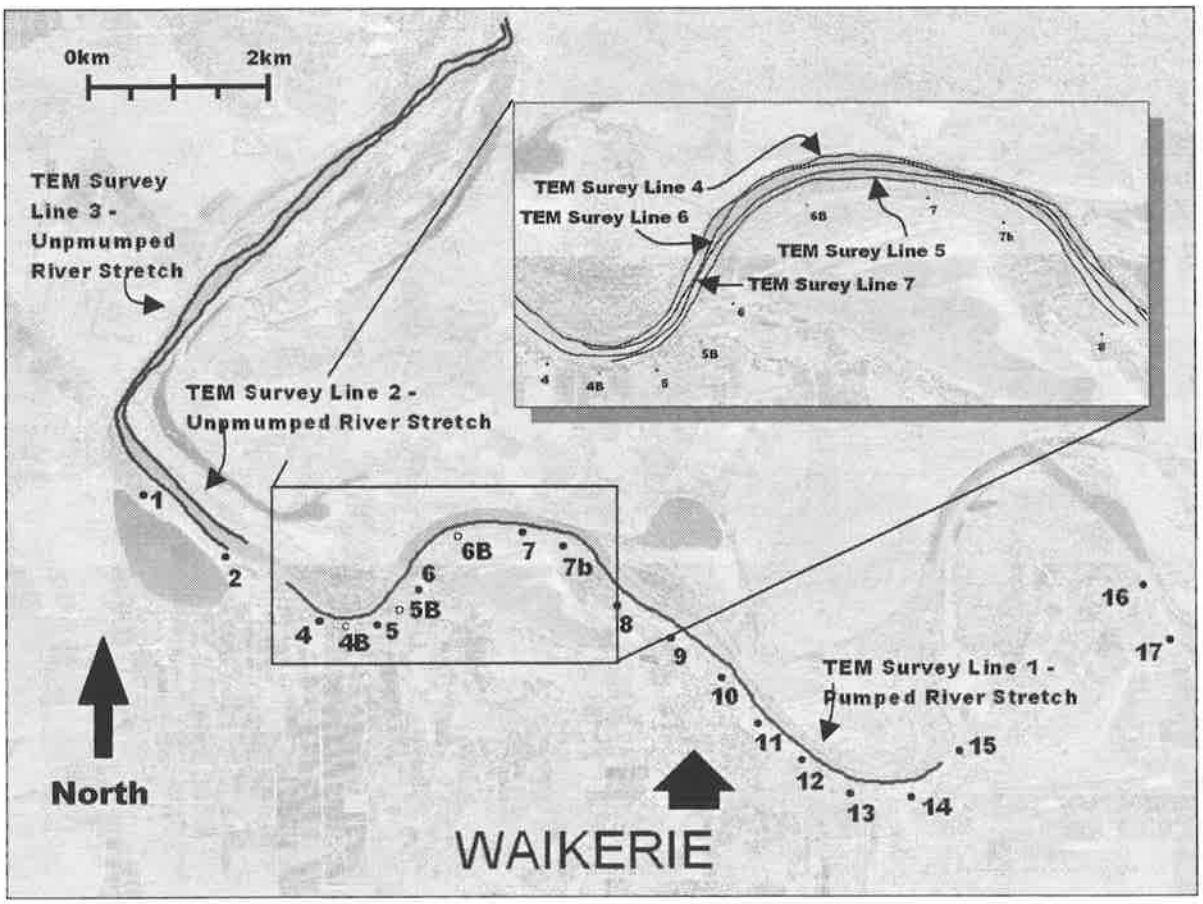

Figure 3.9: Location map of NanoTEM survey lines. Lines 2 and 3 are in the unpumped survey section, while lines 1 and 4 to 7 are in the pumped survey section. Waikerie SIS production bores are labelled.

3.2.3 Processing

GPS, TEM and depth data were recorded in separate files, which were merged using time registration and a Zonge Engineering program called "raw2csv.exe". This program assigns a noise level to each time window by averaging the recorded voltage from its four neighbouring stations. The assigned noise level is the variance from the mean. This relies on the assumption that changes in the response are slow laterally, which is particularly fair with the high sampling rate being used.

The program STEMINV was used to create models from the data. In the inversion, a weighting of three was applied to the vertical smoothing function, and a maximum of eight iterations were performed (most stations required approximately only five iterations before the misfit criteria were reached). Measurements with an error greater than 5% (as determined by the program raw2csv) were disregarded in the inversion. At most stations this corresponded to data after the 15th time window. Note from Table 3.1 that if the resistivity was high (e.g. in fresh water filled sediments), the penetration depth would be greater than 40 m, while in a less resistive model (clay or saline-water filled sediments) the penetration depth would be between 15 to 40 m. Most models were significantly more conductive than 16 ohm.m, so maximum depth of signal penetration seen in the data was approximately 25 m.

TEM models were gridded and displayed using the Geosoft Corporation's Oasis Montaj Earth Science Mapping and Interpretation package (the same software as for DC Resistivity sections) for both two and three dimensional figures

The initial target for this study was the resistivity of the top 5 m of alluvial sediments. To isolate this area in the presentation, a Fortran code was scripted (Appendix A) that changes the depths at each station, such that the river bed is at 0 m.

Chapter 4

Results

4.1 DC Resistivity Data

DC Resistivity data from the August 2002 survey were converted to apparent resistivity for each dipole spacing according to Equation 2.20. Figure 4.1 shows a plot of apparent resistivity for three dipole spacings, na = 5, na = 15, and na = 40, where a is the potential pair size (metres) and n is the dipole off-set (multiples of a); na = inner electrode spacing in metres. This figure shows approximately a kilometre long section that gets more conductive with depth (wider electrode spacings are associated with deeper current flow). Wider electrode spacings are also introducing significantly more variation in the observed apparent resistivity, due to reduced signal strength. The signal-to-noise level appears to be approximately one for na = 40. For even larger electrode offsets (na = 50 in Figure 4.2) the signal-to-noise level is much less than one, and large variations in apparent resistivity between stations (more than an order of magnitude) make recognition of data trends difficult. The system could be run with higher input current which would help to improve the signal-to-noise ratio at large off-set, however considerably large power requirements will limit the duration of the survey due to the logistical problems of battery storage on a small river launch.

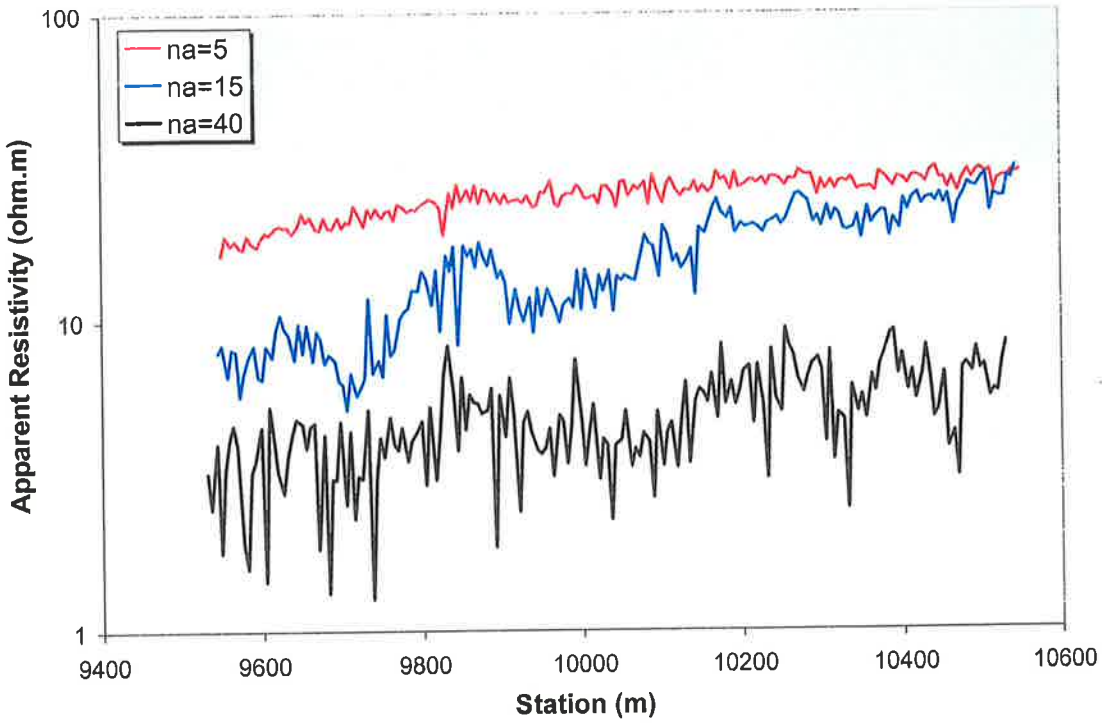

Figure 4.1: Apparent resistivity estimates from dipole spacings na = 5, 15 and 40 (where a is the receiver dipole size and n is the dipole spacing in integer multiples of a). Smaller electrode spacings (near surface measurements) show higher resistivity and significantly less noise.

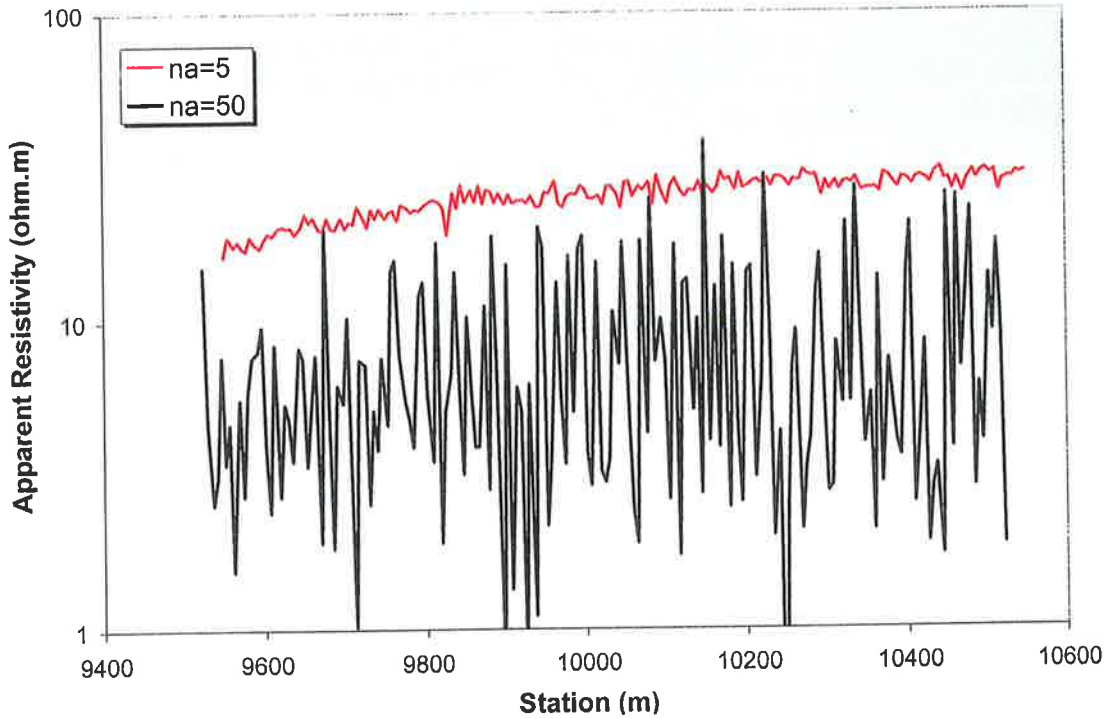

Figure 4.2: Apparent resistivity estimates from dipole spacings na = 5 and 50 (where a is the receiver dipole size and n is the dipole spacing in integer multiples of a). Noise is so high in the largest dipole spacings as to make trend identification all but impossible.

Figures 4.3 and 4.4 show DC resistivity models from data obtained in the unpumped and the pumped survey areas respectively (see inset or Figure 3.4 for survey line locations). The models were generated using TS2DIP with all available dipoles included. Models have been coloured according to resistivity on a log scale, from 1 ohm.m to 15 ohm.m with warm colours corresponding to conductive features and cool colours corresponding to resistive features. The original models extended to approximately 60m depth, however only the top 25m have been displayed. Both figures have significant vertical exaggeration (see vertical scale on figures), producing a "banded" or "striped" appearance in most areas.

An important source of noise in the DC Resistivity system may come from the flow of river water through the Earth's magnetic field (Longuet-Higgins et al., 1954). A potential field is created in a direction perpendicular to both the water flow and the magnetic field:

$$\nabla\phi = \mathbf{v}\times\mathbf{B} - \rho\mathbf{J} \tag{4.1}$$

where $\nabla\phi$ is the potential difference due to water of resistivity ρ flowing with velocity $\mathbf{v}$, and $\mathbf{J}$ is the current density that results. When water flow has a component perpendicular to the separation of the potential electrodes, this potential difference may be measured as noise. As an example, if the cross-line component of water velocity is 0.5 m/s and the vertical component of the Earth's magnetic field is approximately 50,000 nT, the measured potential is on the scale of 25 μV/m. When the potential dipoles are 20 m, we have possible noise levels as large 0.5 mV. This is significant at far offsets, when the signal voltage is on the millivolt scale.

The models show a resistive (30 ohm.m) uppermost layer with a thickness that correlates well with measured water depth at most locations. However, 30 ohm.m is higher than the known water resistivity of 16 ohm.m. This may be due to the finite width of the river, which is assumed to be infinitely wide in a two dimensional modelling sense, and will distort the surface potentials.

Beneath the river bed, resistivity decreases to between 0.1 and 5 ohm.m to a depth of 25m, probably due to conductive water contained in porous river alluvium and/or clay conduction effects. Archie's Law (Equation 2.4) suggests that water with 22,000 mg/L TDS (40,000 EC) would need to exist in 50% porosity sand to produce 1 ohm.m bulk resistivity sediments. This conductive feature is present throughout most of the survey, but

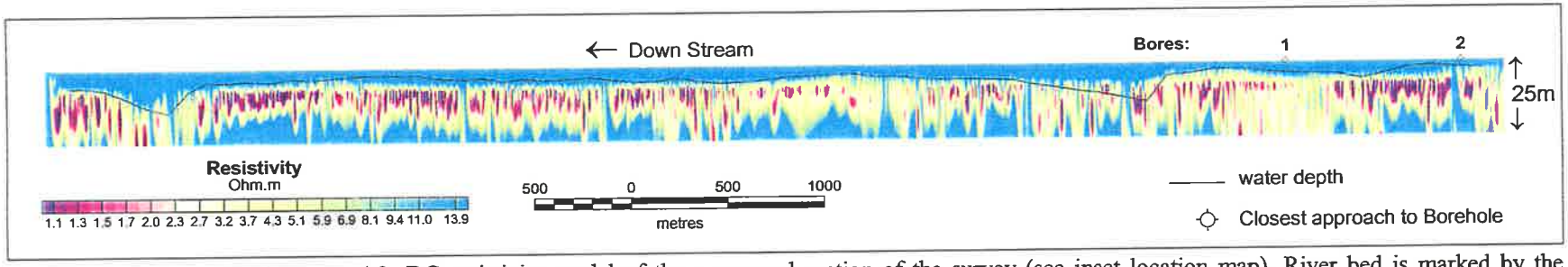

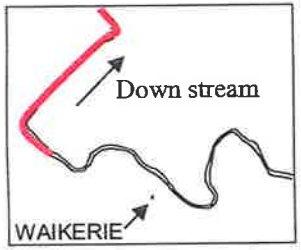

Figure 4.3: DC resistivity model of the unpumped section of the survey (see inset location map). River bed is marked by the horizontal line. The conductive features beneath the riverbed appear as vertically orientated features due to vertical exaggeration, and become slightly more consistent in the downstream direction.

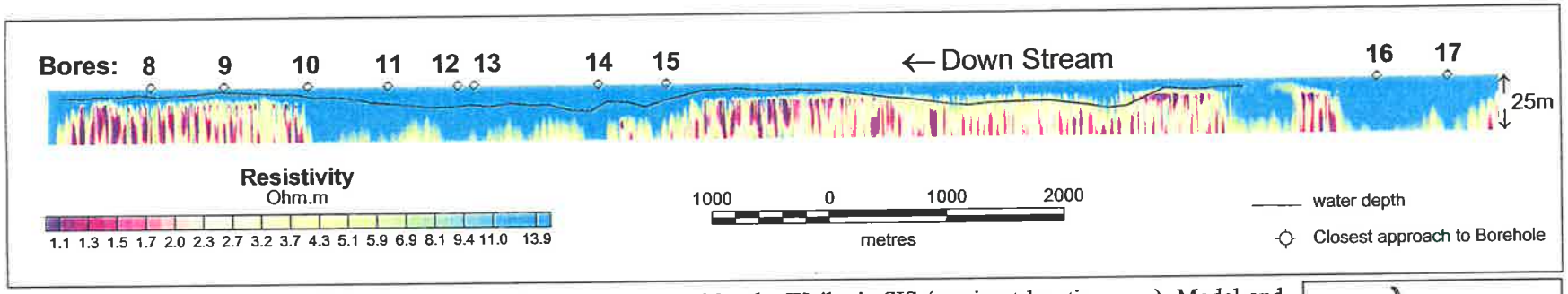

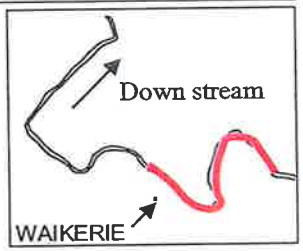

Figure 4.4: DC resistivity model for the section of the survey pumped by the Waikerie SIS (see inset location map). Model and production bore locations are plotted with respect to eastings, and since production bores are between 50 and 200m away from the survey line, there is a slight mismatch between production bore location and the closest approach of the model. 3D presentations (Figures 4.5 and 4.6) assist correlation of features with production bores.

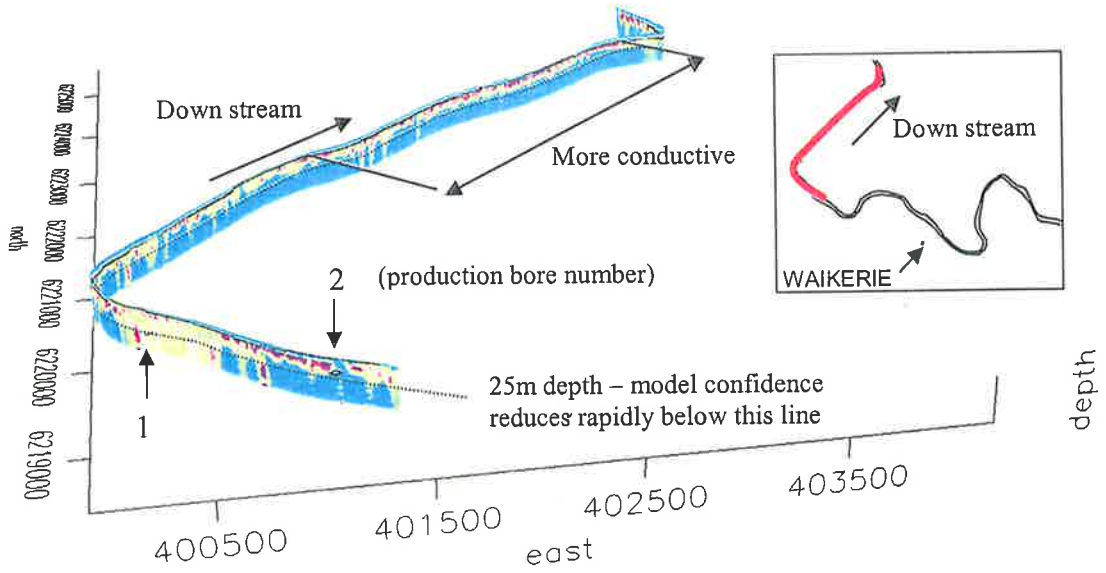

Figure 4.5: Three dimensional projection of the model in Figure 4.3. The full 60m model section is displayed with 5 times vertical exageration, however the largest outer electrode spacing is 100m, so confidence in the model is small below approximately 25m depth. Production bores 1 and 2 from the Waikerie SIS are labelled, however most of this section was not under the influence of a SIS during the survey.

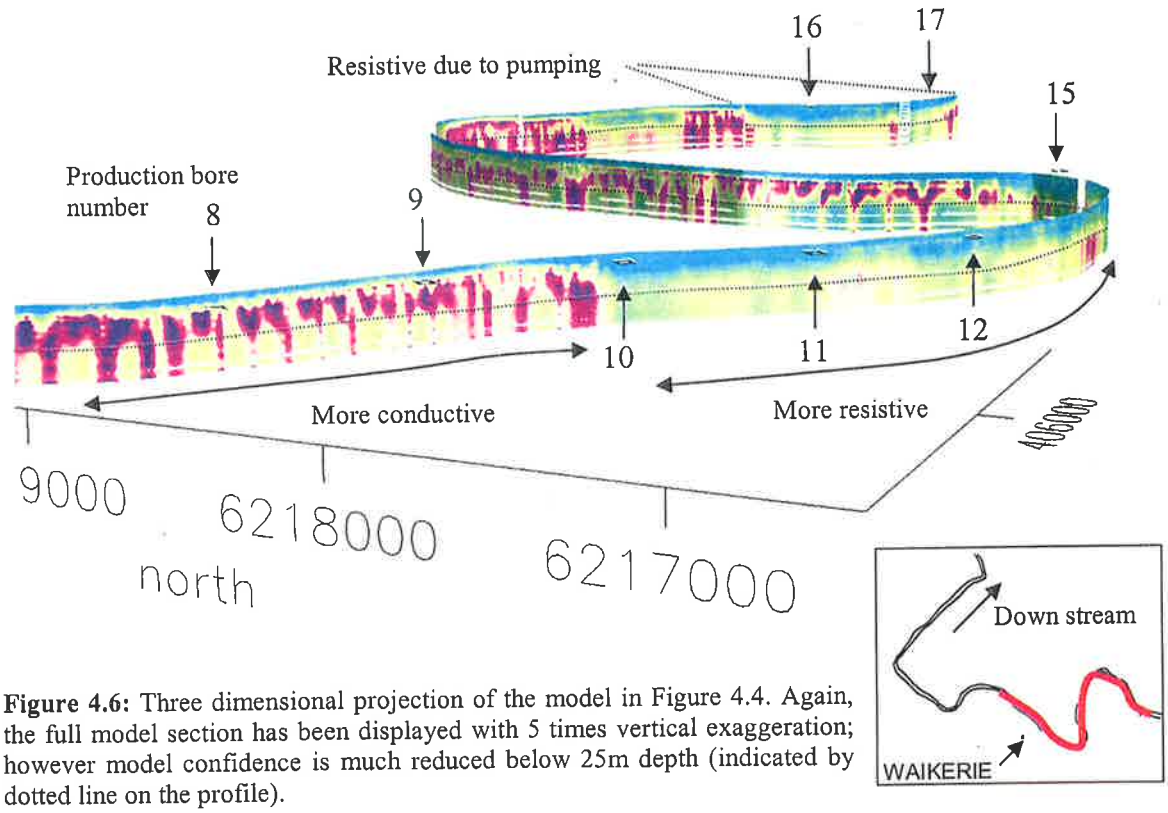

Figure 4.6: Three dimensional projection of the model in Figure 4.4. Again, the full model section has been displayed with 5 times vertical exaggeration; however model confidence is much reduced below 25m depth (indicated by dotted line on the profile).

is very noisy, giving a banded appearance. Towards the down-stream end of the unpumped section, this feature becomes slightly more conductive, ranging between 0.1 and 2 ohm.m (Figure 4.3).

In the pumped survey section (Figure 4.4) some correlations exist between resistivity at depth and production bore locations. In particular, production bores 16 and 17 show resistive features down to at least 20m depth, and maybe a direct response of the SIS drawing fresh river-water through the river alluvium. However, a similar anomaly is present approximately 1km downstream of production bore 16, where no SIS production bore is operating. One explanation could be that paleo-channels cause inhomogeneous permeability patterns, resulting in fresh-water drawdown at this location. Variations in permeability of sediments may also explain why some production bores show significant resistive anomalies, while others appear to occur where there are no anomalies (e.g. production bores 8 and 9 in Figure 4.4).

Three-dimensional presentations of data are important for correlating anomalies with geographical and geological features because the survey does not follow straight lines. The three-dimensional presentations for Figures 4.3 and 4.4 are shown as Figures 4.5 and 4.6 respectively.

4.2 TEM Data

Figure 4.7 is a plot of raw TEM data, showing the voltage measured in each of 31 time windows for a single station (stack of 64 soundings). A smooth decay of the secondary field is indicated by smooth changes in the measured voltage. Time windows 1 to 3 do not exhibit such smooth changes and were discarded from the inversions. Possible reasons for the unusual behaviour of the early time windows are discussed in section 4.3. An estimate of noise in each window was determined by the variance from a mean value calculated from neighbouring stations, enabling rejection of noisy data before an inversion. At most stations 5% variance and larger occurred after the 15th time window; such windows were therefore rejected. Windows 4 to 15, shown on Figure 4.7, were used for most stations. The approximate noise-level occurs where voltages become approximately invariant with time (do not decay). Table 4.1 lists the error estimates for each time window from a typical station.

All TEM models have been coloured using the same scale used for DC resistivity model sections. Resistivity values measured at the surface are between 5 and 10 ohm.m. These are slightly more conductive than the known water resistivity of 16 ohm.m; possible causes for this discrepancy are discussed in Chapter 5. Figure 4.8 shows the TEM model produced for the pumped survey section during the August survey (between SIS production bores 4 and 13). Three simple observations can be made from the model: (a) there is an extensive resistive region upstream of production bore 10; (b) there is an extensive conductive region between production bores 6 and 7; and (c) there are isolated resistive features that correspond with production bore locations.

The top profile in Figure 4.8 (between production bores 4 and 8) was chosen for the repeat survey (see Figure 3.9 for survey line location), to investigate changes across the width of the river (approximately 200m). Figure 4.9 shows four parallel profiles (survey lines 4 to 7) arranged with the northern most line at the top. The resistive anomalies produced by pumping from production bores can be identified on each of the survey lines, but the effect is greatest on the lines closest to the southern river bank. The conductive region between production bores 6 and 7 is more extensive, and closer to the river bed in the northern most lines.

The unpumped river stretch is shown in Figure 4.10 (survey lines 2 and 3) with the western most line on top (see Figure 3.9 for survey line locations). Data show conductive features beneath the river bed on the southern ends of the survey lines (at the left of the figure), and an increase in conductivity from downstream of borehole T5 toward the northern end of the survey lines (towards the right of the figure).

Some differences between the two sides of the river can be seen. In particular, a conductive feature 500m downstream of borehole T5 appears more prominently on the western side than on the eastern side of the river.

Figures 4.9 and 4.10 are represented in three dimensions by Figures 4.11 and 4.12 respectively. In both of these figures the survey lines have been offset from each other by 200m, enabling their full sections to be viewed. The relationship between borehole location and resistive anomalies is more apparent in these projections.

Window	Centre Time (μs)	Measured Voltage (μV/A)	Noise (%)
1	0.519	1.53E+06	0.1
2	2.125	1.66E+05	0.1
3	3.731	4.21E+04	0.1
4	5.337	2.24E+04	0.1
5	6.943	1.12E+04	0.15
6	8.55	7.82E+03	0.2
7	10.93	5.01E+03	0.29
8	14.15	3.11E+03	0.41
9	17.36	2.16E+03	0.54
10	21.34	1.52E+03	0.7
11	26.17	1.06E+03	0.91
12	32.48	7.10E+02	1.23
13	41.28	4.40E+02	1.76
14	51.69	2.77E+02	2.52
15	64.44	1.98E+02	3.17
16	80.43	1.00E+02	5.61
17	101.1	6.42E+01	7.83
18	128.2	2.73E+01	16.39
19	161.8	2.59E+01	15.38
20	203.3	1.34E+01	26.65
21	255.2	3.48E+00	91.48
22	321.2	2.06E+00	100
23	405.1	6.60E+00	38.28
24	508.9	2.90E+00	77.87
25	639.6	1.86E+00	100
26	805.6	3.98E+00	45.06
27	1014	6.90E+00	23.2
28	1276	3.68E+00	38.71
29	1607	2.92E+00	43.5
30	2022	4.10E+00	27.65
31	2547	4.38E+00	23.07

Table 4.1: Example values and noise level recorded in TEM data. The noise was estimated by comparing the value recorded in five adjacent stations. The first three time windows and windows with noise greater than 5% were rejected in the inversion, leaving the unshaded values.

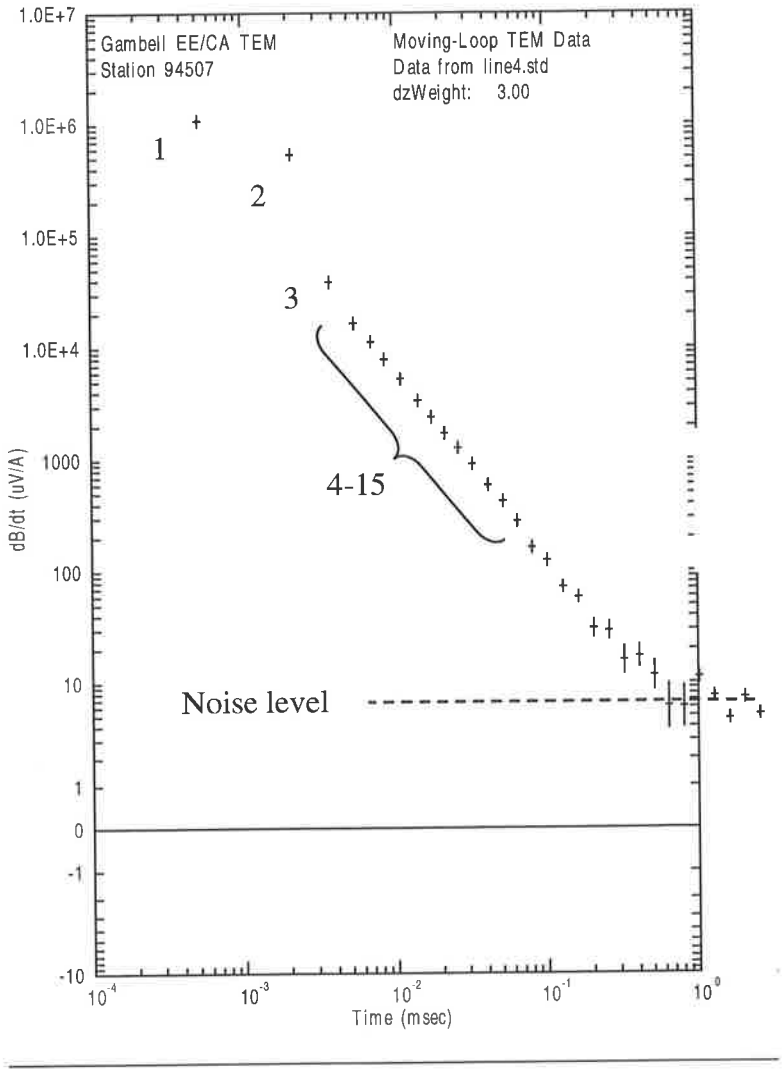

Figure 4.1: A graphical example of the TEM data recorded for one station. Windows 1, 2 and 3 do not exhibit a smooth decay relationship and were discarded in the inversion. Windows after window 15 generally contained too much noise and were also discarded. Windows 4-15 were used to develop the TEM models presented in this chapter and are indicated in this figure. Finally the noise level is defined by the levelling of the decay curve.

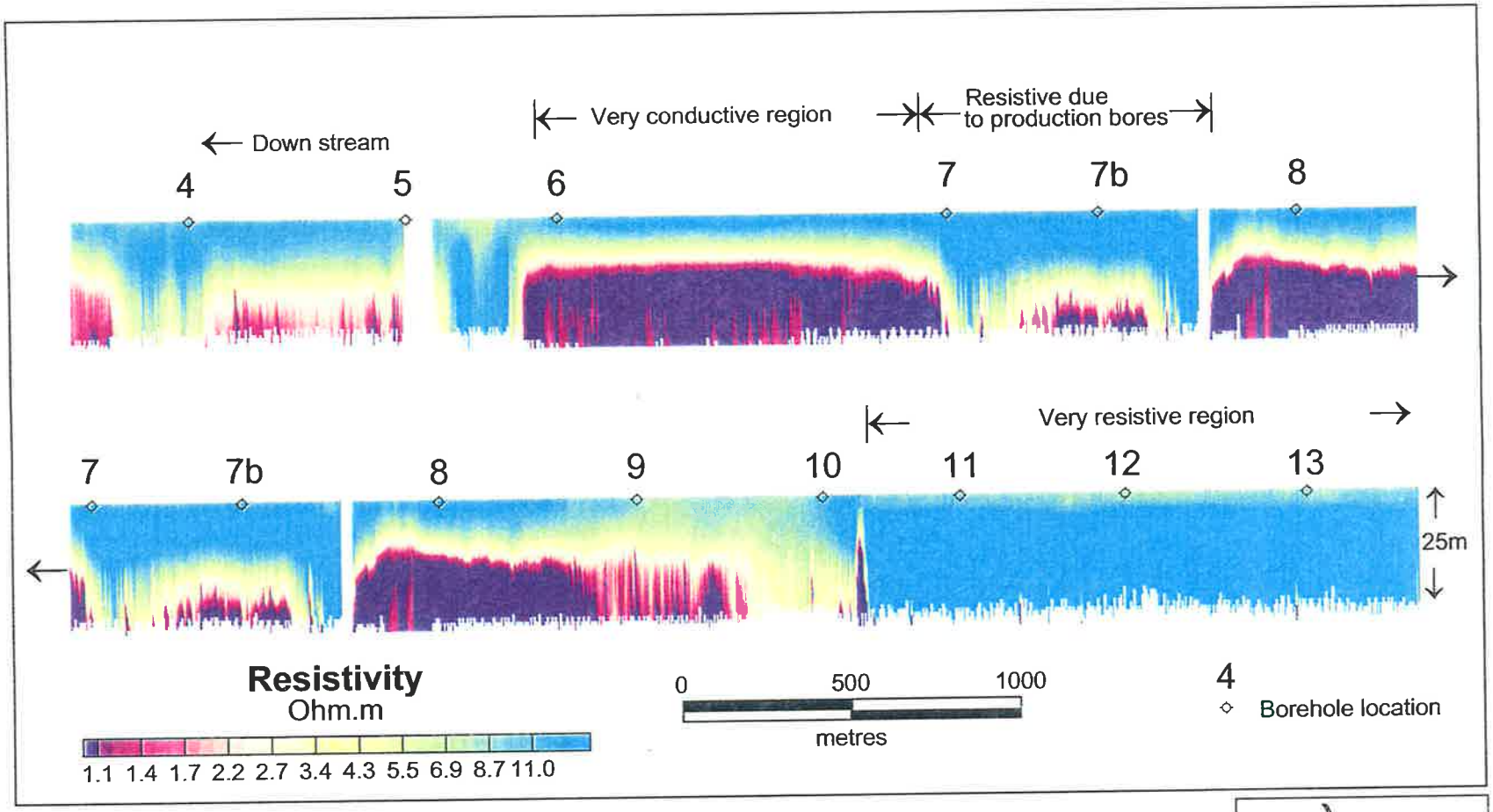

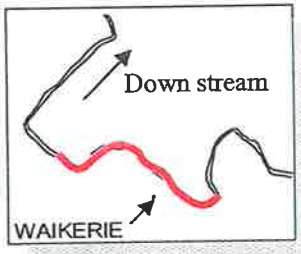

Figure 4.8: TEM model from the August 2002 survey, showing very conductive region between production bore 6 and 7, a very resistive region upstream of production bore 10 and regions of high resistivity approximately corresponding with production bore locations. Note that production bore locations are plotted according to their easting (as with DC Resistivity figures), and consequently, may be offset from the model's closest point of approach.

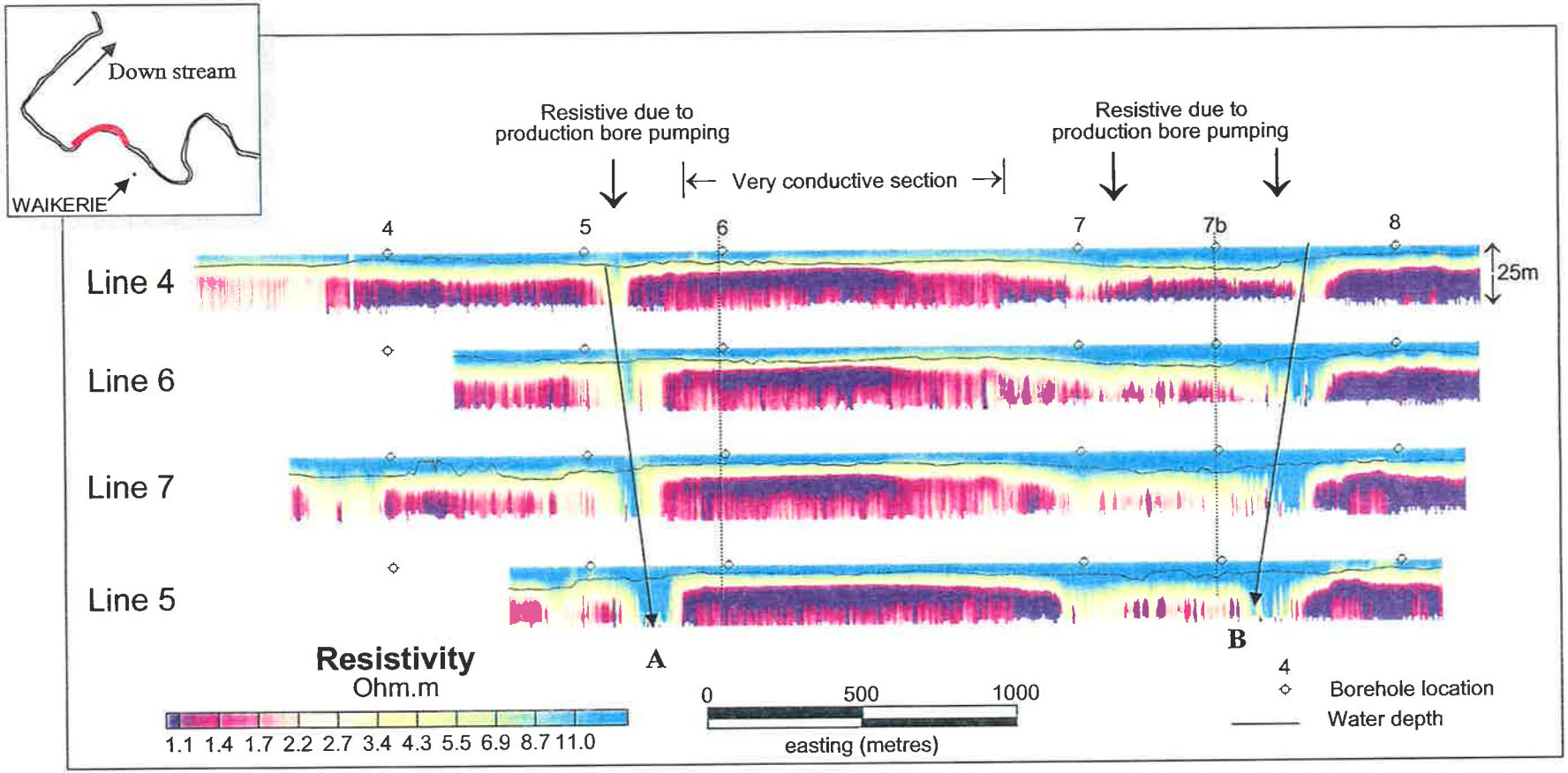

Figure 4.9: Four parallel TEM survey lines from the December 2002 survey. These are arranged with the northern most line at the top. These figures show how the resistivity structure beneath the river varies across the river. As for Figure 4.8, production bore locations are only approximate. Note that the conductive region between production bores 6 and 7 gets broader and closer to the river bed towards the north side of the river. Also, resistive anomalies (A and B) become more prominent towards the southern bank of the river (closer to the production bores). We can also see that the anomaly A is due to production bore 6, and anomaly B is due to production bore 7B because the error in production bore placement is reduced in the closer survey lines.

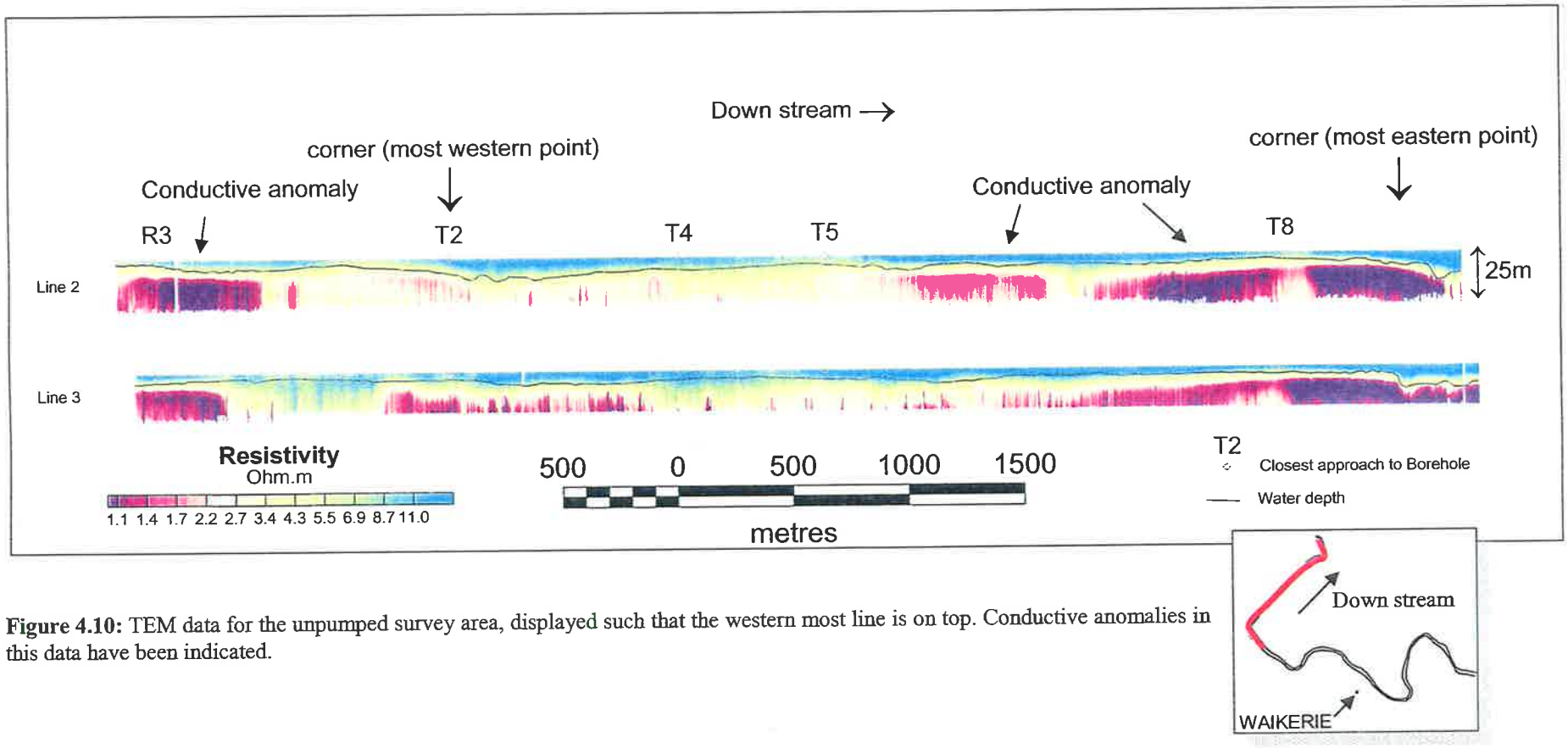

Figure 4.10: TEM data for the unpumped survey area, displayed such that the western most line is on top. Conductive anomalies in this data have been indicated.

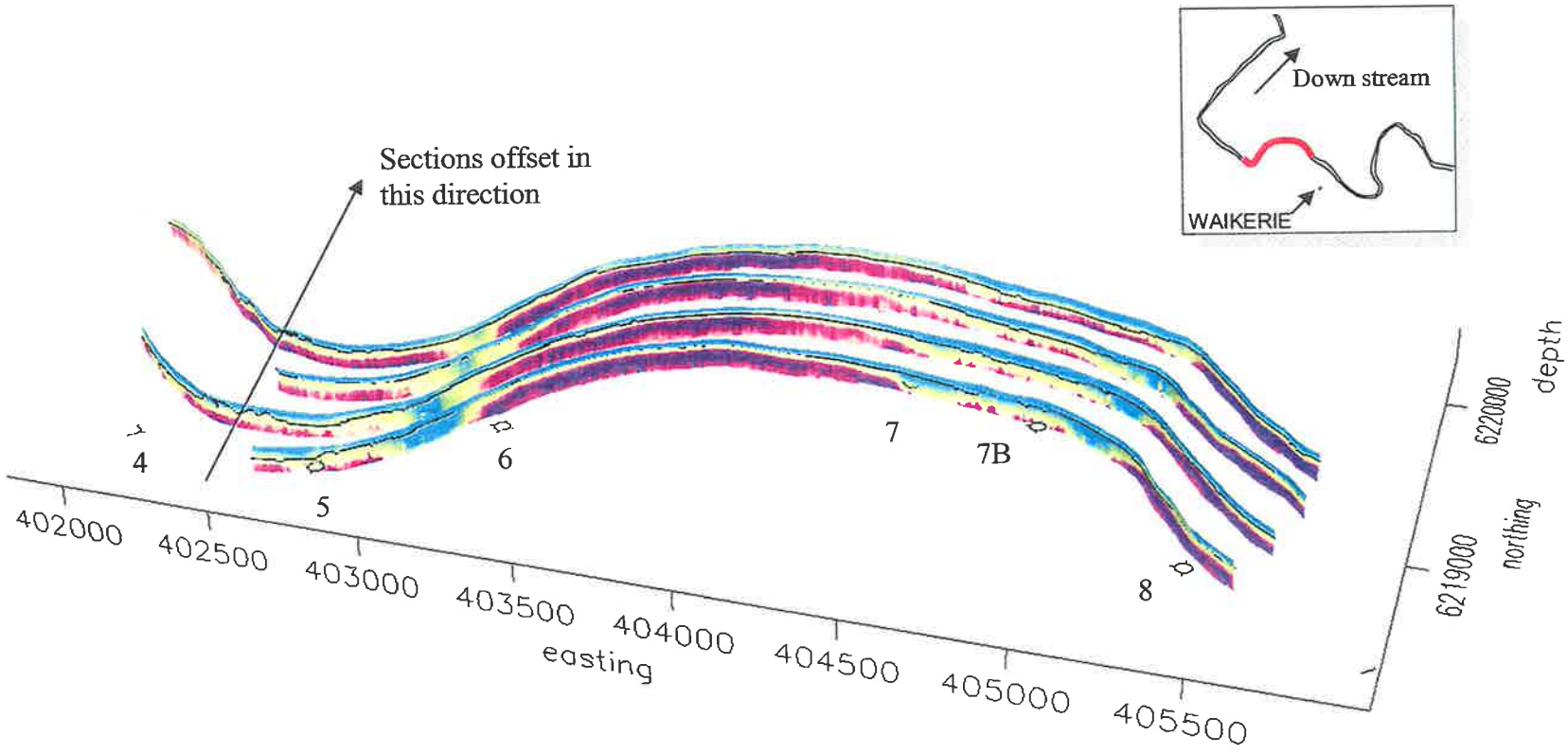

Figure 4.11: Three-dimensional presentation of TEM data in Figure 4.9. Borehole locations are numbered. The sections were offset towards the north so that all data could be viewed (width of river is approximately 200m). This presentation enables correlation between production bores and resistivity anomalies. Water depth is drawn on the model sections. The colouring of the data is identical to that used in Figure 4.9.

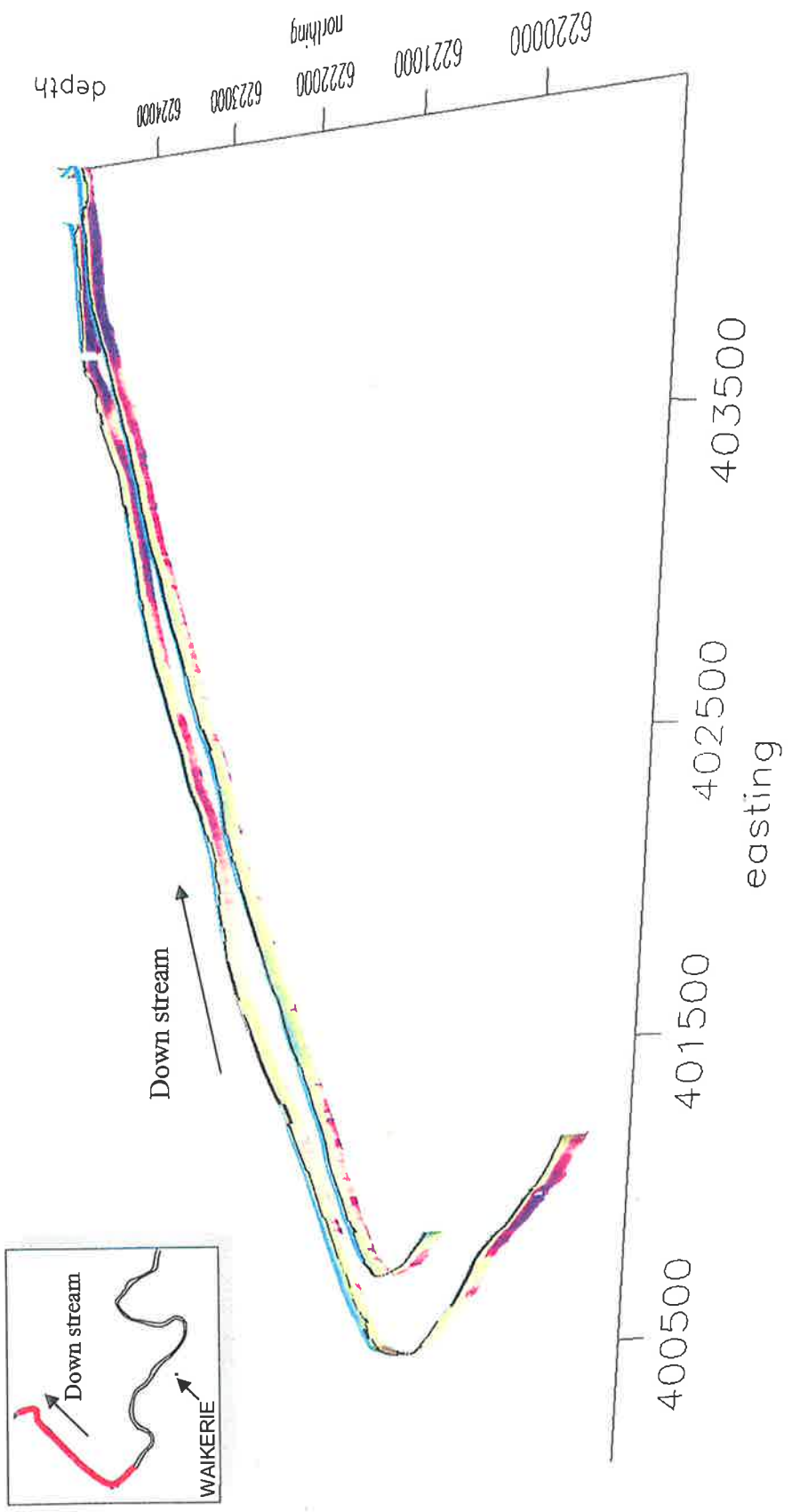

Figure 4.12: Three-dimensional presentation of TEM data in Figure 4.10. The sections were offset in the east-west direction so that all data could be viewed. The section becomes more conductive towards the downstream end of the sections. Water depth is drawn on the model sections. The colouring of the data is identical to that used in Figure 4.10

4.2.1 River Alluvium Profiles

Figure 4.13 shows the resistivity structure of the top 5m of river sediments for survey lines 4 to 7. The conductive anomaly between production bores 6 and 7 is more prominent on the northern most survey line. Also, there is a good correlation between production bore locations and the resistivity of the top 5m of river sediment.

A plan view of the resistivity of the top 5m of alluvial sediment is shown in Figure 4.14. This Figure was created by averaging the resistivity of the top 5m of alluvial sediment at each data station, and creating a horizontal, minimum-curvature grid of the data. The survey line paths have been plotted on the figure and salt-loads calculated from run-of-river data have been plotted adjacent the grid. Three major and four minor salt-load locations have been identified. The major salt-load locations occur 1-2 km upstream of run-of-river salt-load highs, because denser saline water is not detected at the surface until changes in river depth or bends in the river cause mixing to occur (Telfer, 1989).

Finally, the horizontal grid of the pumped section (four parallel survey lines) is shown draped over river bathymetry in Figure 4.15. In this presentation, resistivity changes are compared with changes in water depth. The most significant conductive regions in this figure correspond with deep points in the river, in agreement with Telfer (1989) who calculated that river trenches provide 40-60% higher accession rates than other locations using theoretical models.

Figures 4.14 and 4.15 show conductive anomalies that have been labelled salt-load hot-spots, but it is worth noting some limitations. Using only two survey lines in the unpumped section means that cross-river data resolution is low (100-150m compared to 25-50m for the four parallel lines in the pumped section). Consequently, less confidence can be given to the unpumped section in Figure 4.14.

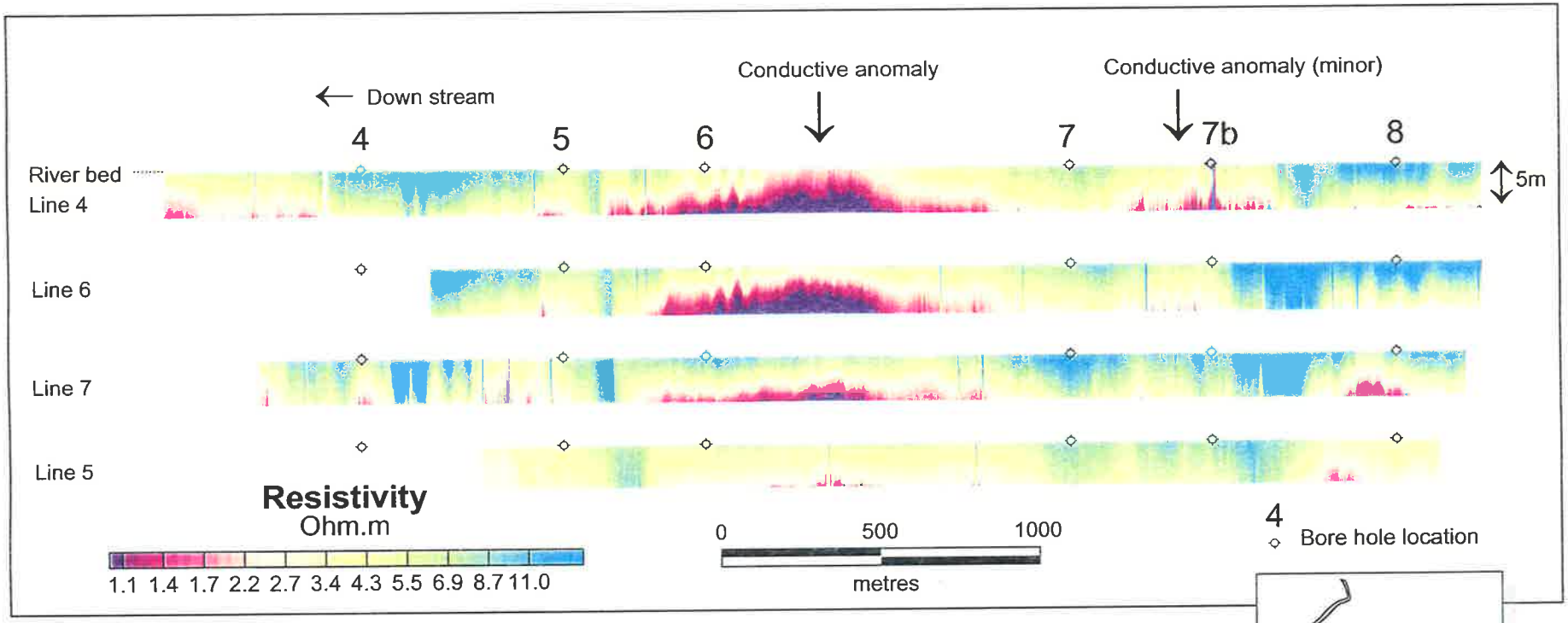

Figure 4.13: Resistivity structure of the top 5m of alluvial sediments showing a major conductive feature between production bores 6 and 7. Survey lines are arranged with the northern most line at the top (as for Figure 4.9). The conductive feature is likely to be saline water in the alluvial sediments, and hence a salt-load peak (or hotspot). The feature is most predominant on the northern side of the river. Minor conductive anomalies can also be seen in line 4 opposite production bore 7B and in lines 7 and 5, adjacent production bore 8.

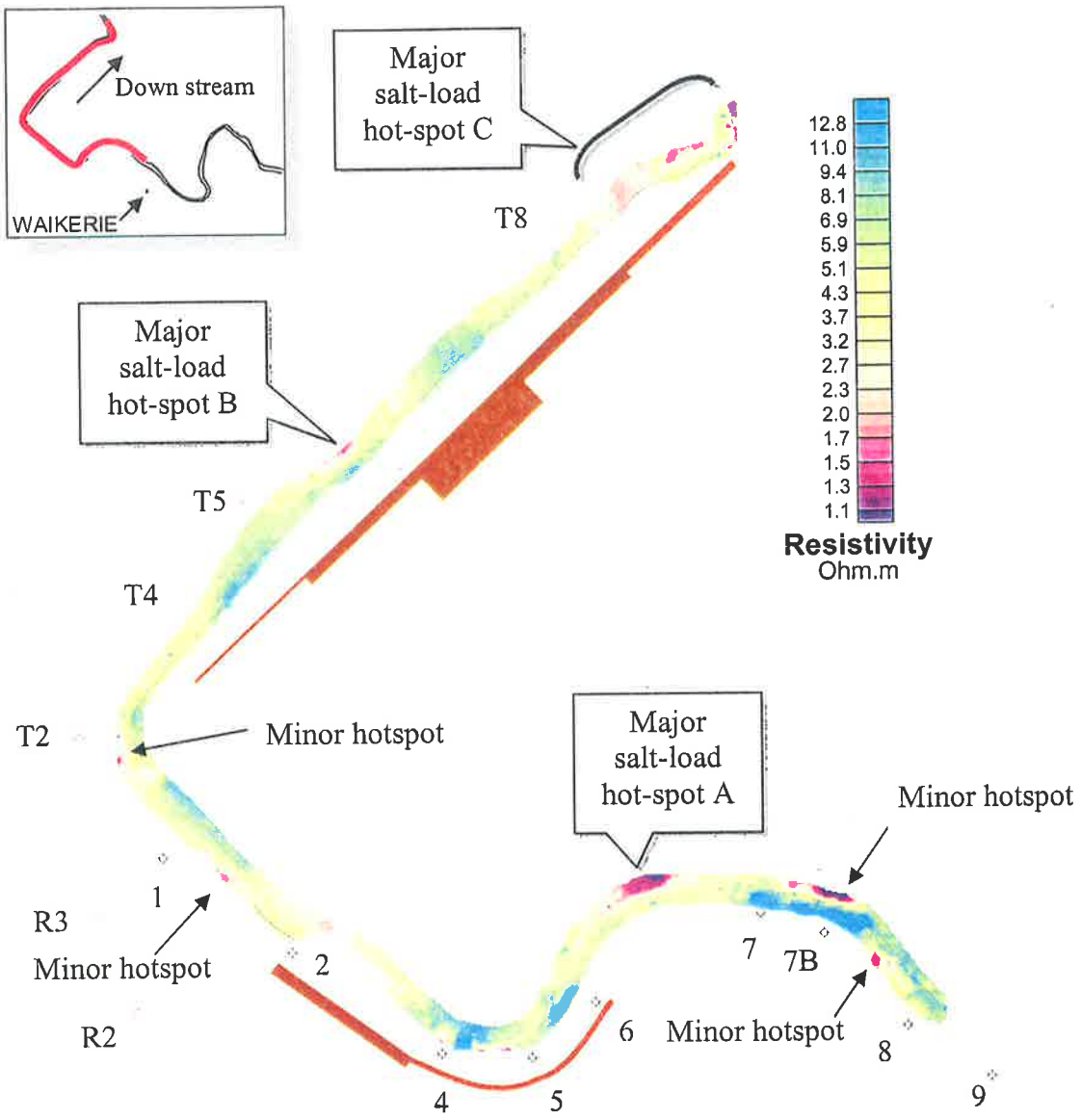

Figure 4.14: Horizontal grid of the average resistivity of the top 5 m of river alluvium showing conductive anomalies that are interpreted as salt-load hot-spots. Production bores are labelled. Red lines adjacent the data indicate run-of-river determined salt-loads (with line thickness proportional to salt-load ranging from 0.3 tonnes/day/km to 5.8 tonnes/day/km)

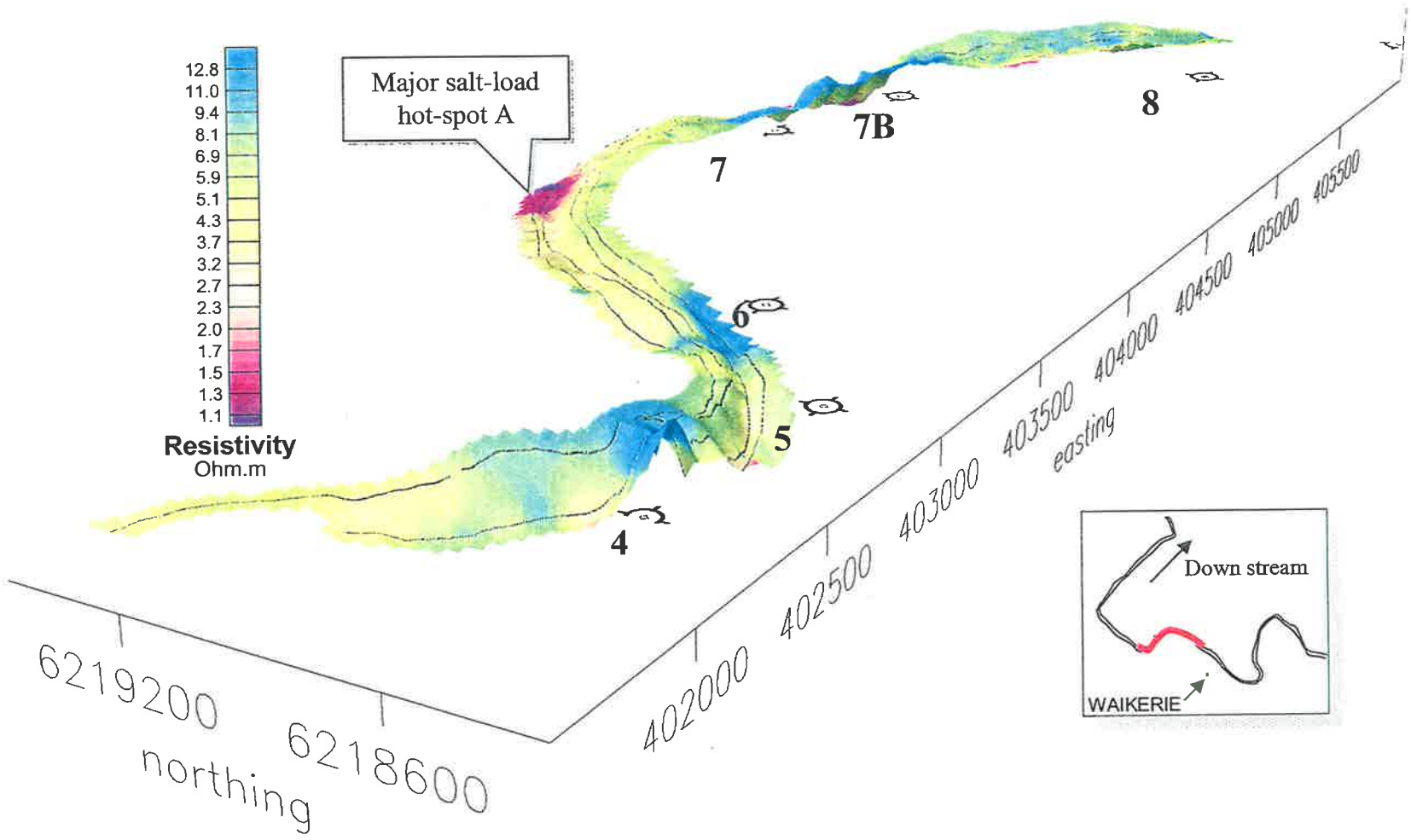

Figure 4.15: Four parallel lines have been used to create this horizontal grid of the average resistivity of the upper 5m of Murray River Alluvium. The grid has been displayed with the vertical relief defined by the measured water depth. It shows that Waikerie SIS production bores 4, 6 7 and 7B correspond with resistive anomalies. A conductive feature that is possibly a salt-load hotspot is indicated between production bores 6 and 7.

4.3 Comparison of Inversions

4.3.1 Inclusion of Early Time Windows

The earliest recorded time windows (1-3) were discarded during the inversions because they did not appear to obey a simple decay relationship (Figure 4.7). The first two time windows appear to have similar voltages, and a large voltage drop occurs between windows 2 and 3.

There are a number of possible contributing factors to the errors in these early-time voltages. Firstly, there exists a known sharp boundary between the 16 ohm.m water and the more resistive sediments (where fresh water saturates the sediments). In Chapter 3, it was established that in a 16 ohm.m half-space, the first three time windows would correspond to 3.6, 7.9 and 9.3m depth, which is within the depth range of this interface. Because early time windows correspond with diffusion across the water-alluvium interface, the data was inverted again with the first three time windows included. The calculated model (Figure 4.16) fits reasonably well at later times, but the smoothness constraint prevents a good model fit at the early times (near surface) and there is serial correlation in the residuals of the model. For comparison, Figure 4.17 shows a station from the inversions with the first three windows excluded. The model fits all data at all times and shows no serial correlation. Figure 4.18 shows a comparison of the resistivity models calculated for the inversions with and without the first three time windows. The inversion that excludes the early time data is a less complicated model, showing smoother variation, and is more realistic.

Including the three time windows changed the calculated vertical resistivity pattern, but did not change the horizontal resistivity patterns in the top 5m of alluvium. Using the same processing techniques, Figure 4.19 shows the same interpreted salt-load locations as was seen in Figure 4.14. However, resistivity at non-salt-load locations in Figure 4.19 is greater (around 25-30 ohm.m), than in Figure 4.14 (around 10 ohm.m).

There are, however, other effects that may cause unusual voltages in the early time windows. In developing the TEM method, the terms $\varepsilon\mu\frac{\partial^2\mathbf{E}}{\partial t^2}$ and $\varepsilon\mu\frac{\partial^2\mathbf{H}}{\partial t^2}$ were ignored in Equations 2.33 and 2.34 for frequencies less than 10^5Hz (equivalent to ignoring displacement currents). The early time windows are sampled at approximately 10^6Hz

(periods of 1 or 2 μs), so the assumptions made may not be satisfactory to explain the behaviour of the EM response at the early times. Displacement currents (which may be due to the Induced Polarisation effect of clay conduction) are most significant immediately after the current turn-off and rapidly diminish; thus the term $\partial \mathbf{D}/\partial t$ in Equation 2.6 will be negative. As a result, the measured magnetic field intensity **H** (and hence the measured receiver voltage) would be smaller than the developed TEM theory would predict (and the inversion codes would calculate).

Additionally, the forward model algorithm in STEMINV assumes uniform currents in the transmitter loop, and a linear current turn-off ramp. Deviations from these assumptions may introduce errors in high frequency (early-time) measurements (MacInnes, pers. comm., 2003). Also, the high currents used in the transmitter (3 Amp) in order to gain signal at later times might be over powering the receiver in the earliest time windows. This would saturate the measurements of dB/dt.

Due to the uncertainty in the cause of the irregularities in the early time windows, more confidence is held in the interpretations gained from the inversions in which these data were ignored.

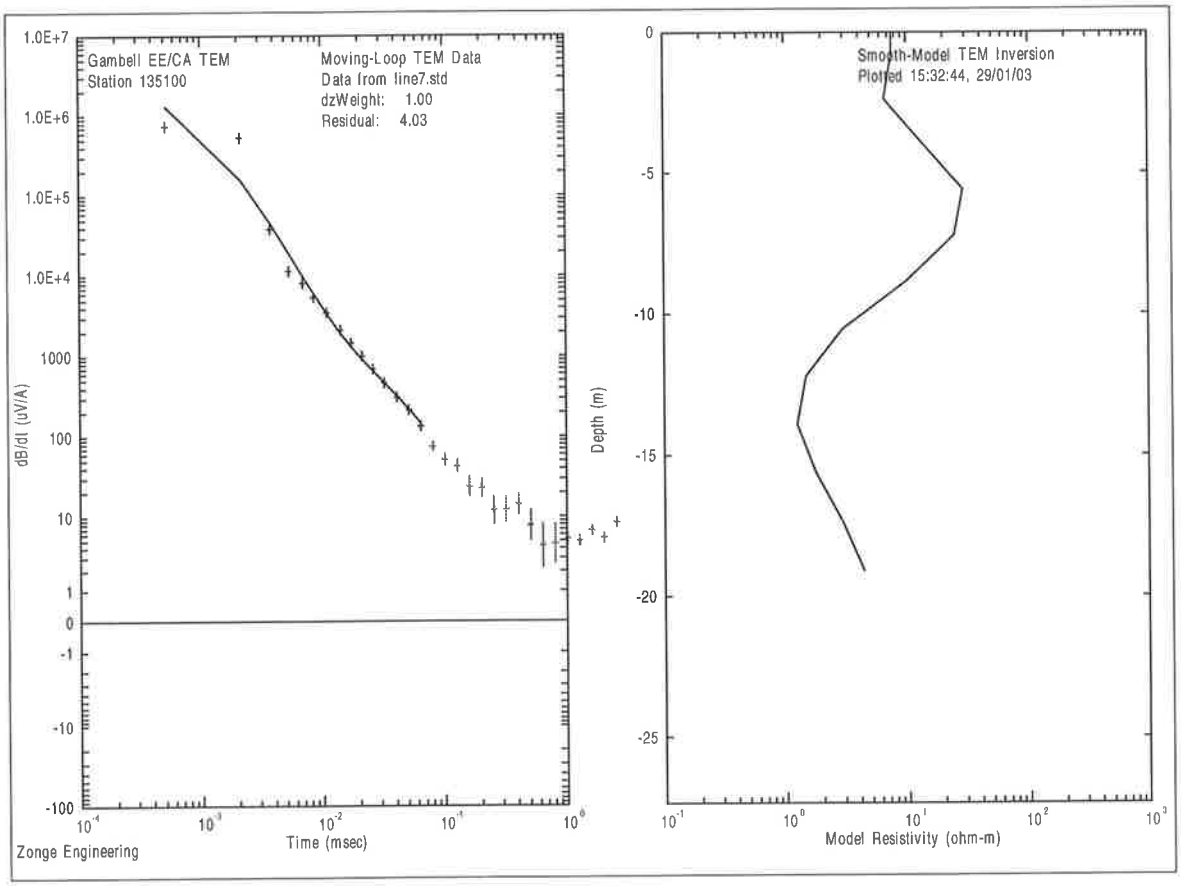

Figure 4.2: Observed and calculated receiver voltages for the inversion that includes the first three time windows (left). Model fit is poor in the early times and the residuals at later times show serial correlation rather than a Gaussian distribution. The calculated resistivity model is shown on the right.

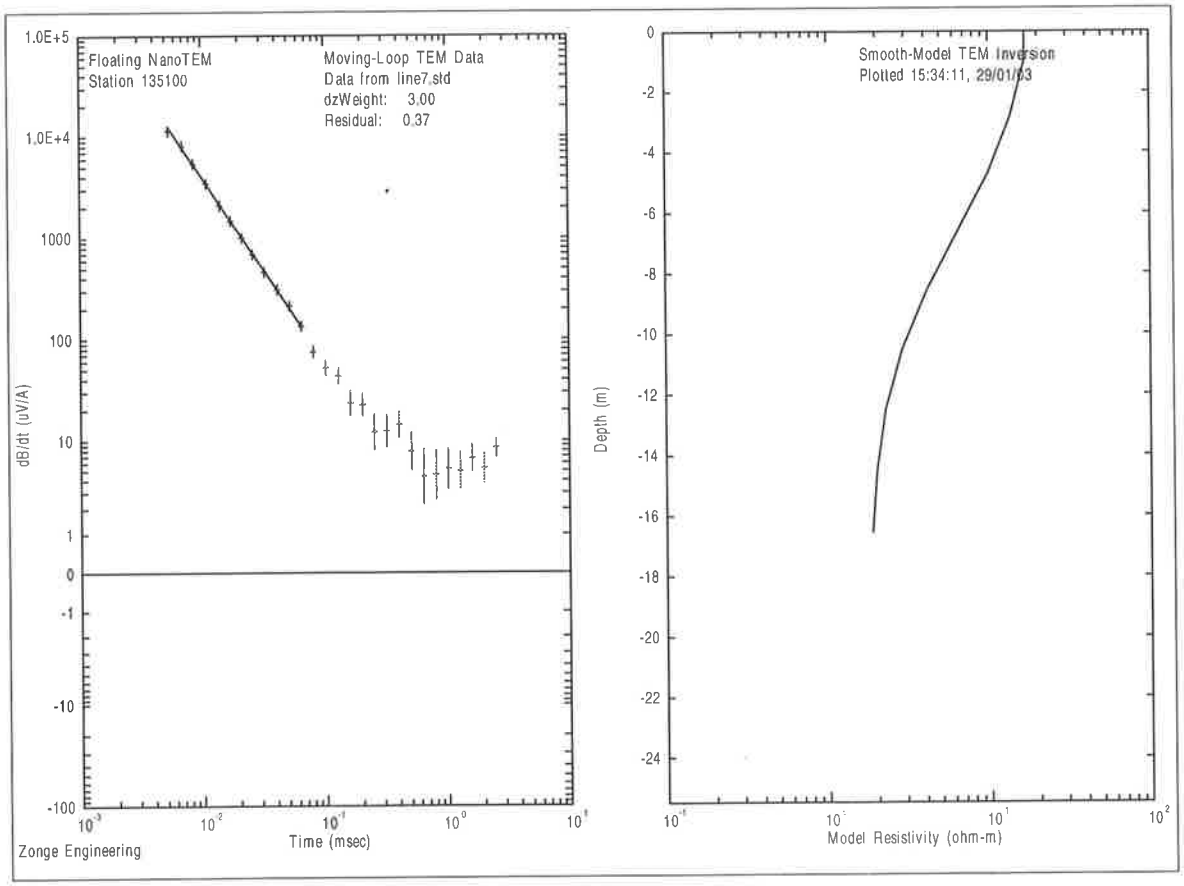

Figure 4.3: Observed and calculated receiver voltages for the inversion that excludes the first three time windows (left). Model fit is very good, and the equivalent resistivity model (right) is smooth and simple.

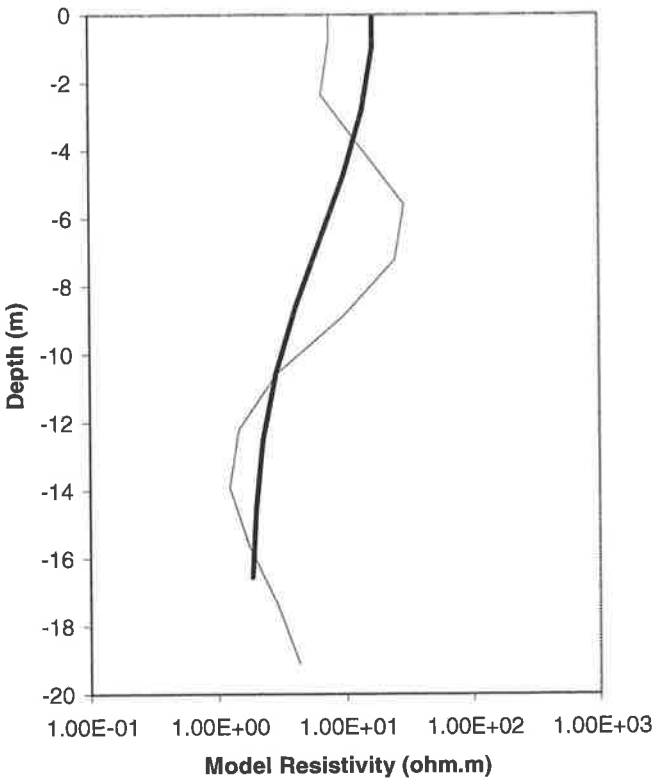

Figure 4.4: The calculated resistivity model for the inversion excluding the early time windows (bold line) and the inversion including the early time windows (light line). The early time windows cause the model to be more complex.

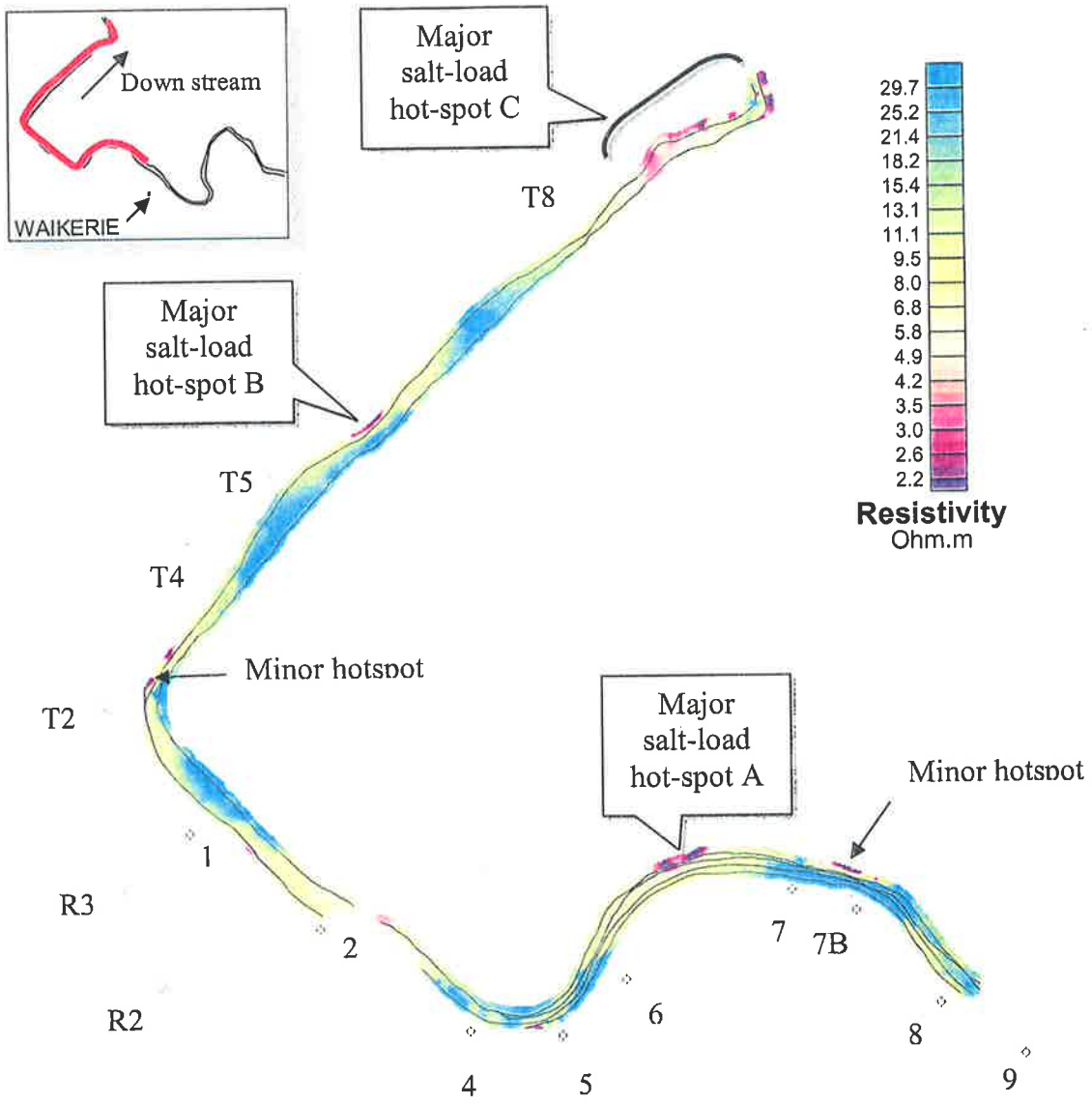

Figure 4.19: The inversion including the early time data results in the same conductive anomaly distribution as the inversion that excluded these windows (compare to Figure 4.14), however the background resistivity (in the top 5m of alluvium) is significantly higher. The values here are approximately 30 ohm.m which could be explained by 10 ohm.m river water in 55% porosity alluvium.

4.3.2 Layer Fixing

Geophysical problems are underdetermined, and have an infinite number of solutions. The more constraint that can be put on a data inversion, the more likely it is to produce a realistic solution (depending on the suitability of the constraints). The STEMINV code puts a smoothness constraint on the models, which is appropriate because of the way EM fields diffuse through the Earth (section 2.4.2) and because most hydrology related resistivity variations are gradual. In most geophysical studies, knowledge of the subsurface is only available in a few boreholes, but in the current survey the resistivity and thickness (water depth) of the top layer of the model is readily available from surface measurements conducted during the survey. Such information could be used as a model constraint, in order to better determine the resistivity of the alluvium, assuming the measured resistivity value is representative of the full water column (which may not be true at salt-load hot-spot locations).

The current version of STEMINV does not allow for parameters to be fixed during an inversion. Instead, a code called EINVRT4 (Sandburg, 1990) was edited to investigate the effect of layer fixing. EINVRT4 is a program for the simultaneous inversion of central loop TEM, DC Resistivity (Schlumberger or Dipole-Dipole arrays) and Induced Polarisation data. For the current study, the code was simplified, by removing all but the TEM operations, removing all graphics operations and defining the NanoTEM system (window times and array size etc).

The forward model in EINVRT4 is as described in section 2.4.5 (also Knight and Raiche, 1982; Raiche, 1984), and the inversion uses the Jupp-Vozoff algorithm (Jupp and Vozoff, 1975; Raiche et al., 1985; Hohmann and Raiche, 1988). EINVRT4 requires n thickness and $n + 1$ resistivity parameters, any of which can be fixed in the inversions. The code does not have a specific smoothing constraint, but each model update occurs in small steps, so that some smoothness is preserved from the original model. To reduce the number of parameters to be used in the inversion, the thickness parameters for each of ten layers were fixed at 2 m.

Figure 4.20 shows two inversions of the same section of TEM data. Section A contains the smooth STEMINV inversion, while B contains the inversion using EINVRT4 with no resistivity fixing. This figure demonstrates that to a large extent, the two codes produce

similar outputs. The Sandburg code, having no vertical smoothness constraint, contains more sharply defined layer boundaries.

The Sandburg code shows higher resistivity in the labelled resistive (blue) region than the STEMINV inversion. The forward modelling that was described in Chapter 2 suggested that the resistivity of layers of finite thickness with high resistivity values will be significantly underestimated by the STEMINV inversion program. The Sandburg code maybe more accurately determining the resistivity of high resistive features, however, the surface resistivity is significantly under-estimated by the Sandburg code.

It is not surprising that the calculated surface resistivity from TEM models is not accurately determined when there is no parameter fixing because we have discarded the first three time windows. The first utilised time window is at approximately 5 μs, which corresponds to over 11m depth (table 3.1). Thus no data in the inversion corresponds to the water column. Models with conductive surface layers may fit the remaining data as closely as models with true surface-layer resistivity and parameter fixing of the upper layer should guide the inversion towards the correct model.

Attempts were made to fix the water layer at 16 ohm.m however the inversion did not converge to a model. Instability in the inversion for a fixed resistivity water-layer are possibly due to the early-time effects that were discussed previously (displacement currents, linear ramp assumptions etc) remaining significant as long as 10 μs (frequencies greater than 10^5Hz), which includes data up to the 6th time window. If the water column is not a constant resistivity, it is likely to be more resistive at the surface due to the density contrast between saline and fresh water. In this situation the measured surface-water resistivity may be higher than an average value.

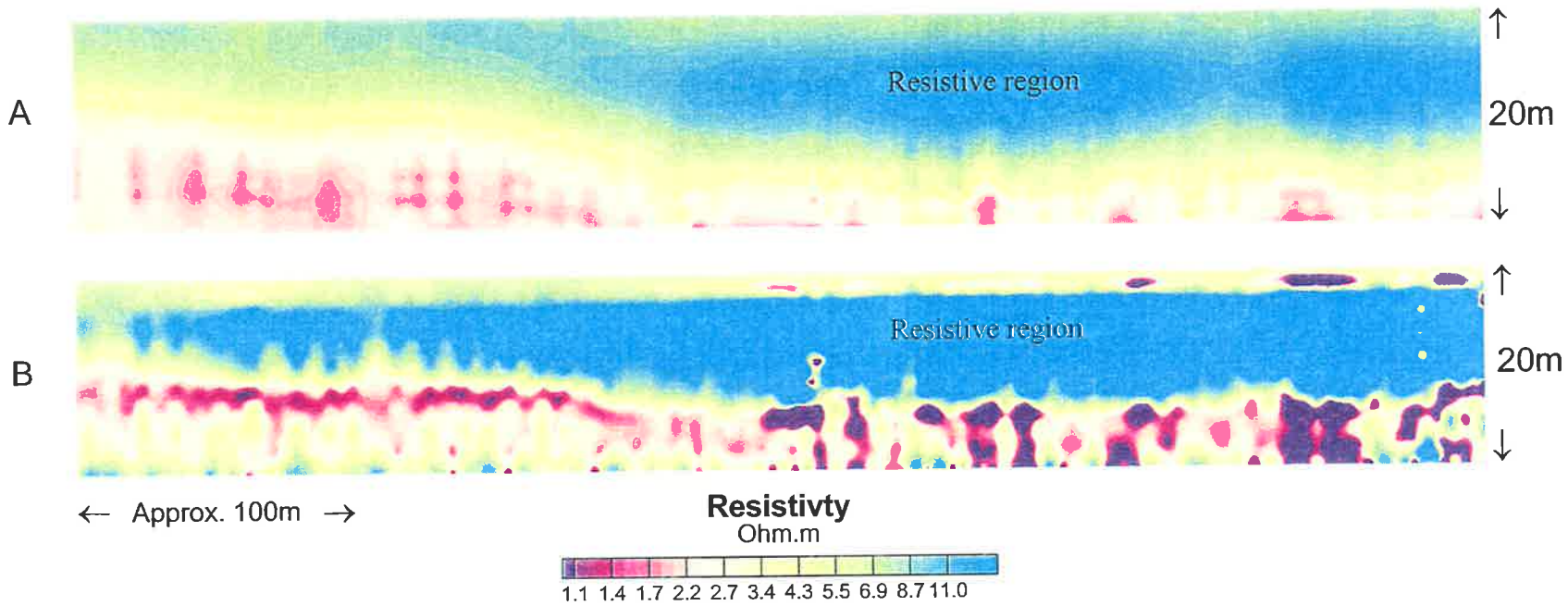

Figure 4.20: Two inversions of the same section of data; section A is the STEMINV program result, while section B is the Sandburg code output. Both show the same broad trend of a resistive region (labelled) that becomes thicker towards the right of figure, overlaying a conductive feature that deepens to the right. The Sandburg code shows higher resistivity values for the resistive feature and lower resistivity values for conductive regions than the STEMINV program. This is probably due to the smoothing criteria in the STEMINV inversion.

Chapter 5

Discussion

5.1 Comparison of Techniques

Two techniques are used in this study to measure the resistivity beneath the Murray River to a depth of approximately 25m and to locate salt-load hot-spots from the resistivity of the upper 5 m of river alluvium. Such data will assist in assessing the performance of Salt Interception Schemes and identify target areas for further investigation. DC Resistivity and TEM techniques are both able to collect many kilometres of data per day. However, TEM exhibits some advantages over the DC Resistivity method.

The TEM array is relatively small (7.5 m x 7.5 m) and is towed only 10 m behind the boat. This makes towing logistics simpler compared to the 150 m array used in the DC Resistivity method (The Blue Eel). Manoeuvrability is greater for the TEM array due to its smaller length. Turning around with The Blue Eel requires almost the entire width of the river (alternatively the array could be gathered onto the boat and re-deployed after the turning manoeuvre, however this is considered an inconvenience). The TEM array is also more visible in the water than The Blue Eel, which floats just below water surface. In future surveys, warning buoys are recommended for The Blue Eel, to reduce the chance of interference from other river traffic. Construction and deconstruction of the TEM array is considerably time consuming compared to The Blue Eel which can be rolled onto a reel for transport. Deployment of the Blue Eel required the array to be laid out along an open bank so that it can be pulled into the water as the boat departs. The TEM array however, needs to be lifted into the water, requiring three people. The development of the TEM array into an autonomous and quickly assembled array is an essential requirement for future work.

Determining the georeferenced location of data points is a simpler process in the TEM survey because the array is closer to the GPS receiver and the measurements are dependant on earth properties directly beneath the array. In contrast, the effective measurement location for the DC Resistivity is the midpoint between the current and potential dipoles. This point is located by extrapolation along the recorded GPS path, but the true data location should be linearly between the dipoles. Consequently, the actual data locations

are off-line from the assumed data locations when the array is not straight. Furthermore, the true distance between the potential and current dipoles would be smaller than the assumed distance (effectively a different dipole number, n). From equation 2.21, over estimating the dipole spacing would cause a more resistive estimate of apparent resistivity.

Signal-to-noise levels appear to become less than one for inner electrode spacing greater than 40 m in the DC Resistivity data (Figure 4.1), which corresponds to less than 15 m depth, however all measured data were included in the inversions, giving models as deep as 25 m. TEM data appears to reach a signal-to-noise level smaller than one after the 25th time window, however all data after the 15th time window were discarded, giving models also to 25m, but at signal to noise levels higher than one. Consequently the TEM data are more reliable at depth.

For practical interpretations of the data to be made, the aesthetic appearance of the models is potentially as important as the accuracy of the model. Signal-to-noise levels less than one below 15 m depth in the DC Resistivity models has produced high frequency spatial variations in resistivity that make the models difficult to interpret. In contrast, TEM models show broad features separated by relatively smooth changes that make interpretation easier.

The surface water resistivity was measured with an EC meter as 16 ohm.m. This and the water depth are the only constraints available for the data. The DC Resistivity method showed a surface resistivity of approximately 30 ohm.m; about twice the accepted value. This may be caused by the finite width of the river altering the potential distribution pattern (which is not accounted for in a two dimensional inversion). Snyder et al. (2002) compared in-stream DC Resistivity profiling to borehole resistivity methods, and the calculated offset between apparent and true resistivity. They concluded that the effect is negligible if the array dimensions are larger than water depth, but in the current study, the array dimensions were similar to measured water depths.

In contrast, the TEM models showed surface resistivities of about 5-10 ohm.m: about half the accepted value. Such variation between the techniques suggests that they were more suitable for identifying relative changes in resistivity than for absolute-resistivity determination. Some justification has been made for the conductive estimate of river water by the TEM technique:

- Forward modelling in Section 2.5.2 demonstrated that resistive layers are likely to be underestimated in STEMINV inversions due to the smoothing criterion.

- Discussion of displacement current effects in Section 4.3.1 predicted that the modelling code would estimate lower resistivity from the early-time measurements when displacement currents are ignored.

- Salinity stratification due to density contrasts are predicted down stream of salt-load hot-spots (Telfer, 1989). Thus the average resistivity of the water column is potentially lower than the surface measurement.

- Given that the first three time windows were discarded for most inversions, the earliest data used is probably from signal already in the sediment layer. Due to the underdetermined nature of geophysical inversion, a model with conductive surface water may fit the data just as closely as a model with resistive (16 ohm.m) fresh-water. The more conductive model may be the inversion result because it is smoother than the correct model.

While both techniques have successfully imaged relative changes in the resistivity structure beneath the Murray River, showing features that correlate with the existing Waikerie Phase I SIS production bores, the TEM method is perhaps more practical due to the dimensions of the towed array and the simplicity in data processing.

5.2 Interpretations

Presentation of data is of critical importance to a successful interpretation process. In this project, five styles of data presentation were used. These were:

1. Full (surface to 25 m depth) vertical sections in two dimensions;
2. Full (surface to 25 m depth) vertical sections in three dimensions;
3. Vertical grid of top 5 m of alluvium in two dimensions;
4. Horizontal grid of top 5 m of alluvium in two dimensions;
5. Horizontal grid of top 5 m of alluvium in three dimensions.

An integrated use of each of these presentations is the most effective method of locating potential salt-load hot-spots.

Full vertical sections in two dimensions are used to establish broad-scale resistivity variations (larger than a kilometre) that are potentially related to geological variations (changes in porosity and clay content are the most important of these). Full vertical sections in three dimensions enabled resistivity anomalies (of all scales) to be correlated with the river course and borehole locations. Two dimensional figures are important for initial identification of anomalies, while their geographical location is best realised in three dimensional figures.

The technique of isolating the top 5m of river alluvium described in Appendix B, has enabled the target of the survey to be interpreted without bias from deeper or shallower resistivity patterns. Two dimensional profiles of these models enabled identification of localised conductive anomalies; these were labelled as potential salt-load hot-spots. Where parallel lines were measured (more lines giving better results) a horizontal grid was created of the resistivity of the top 5m of alluvium, to provide a plan view of the occurrence of conductive anomalies. This allowed salt-load interpretations to include accurate location determination. Viewing this map in three dimensions, and using river bathymetry as relief, demonstrated the concept put forward by Telfer (1989) that river trenches provide significantly more saline water accession than other areas.

An important part of the interpretation process is deciding how geology and hydrology are each reflected in the resistivity structure. This has been achieved by comparing the models with observations of geological changes during acquisition (occurrence of cliffs or flood plain), maps of ground-water salinity (contoured from borehole measurements), and geological cross-sections (created from borehole logs).

5.2.1 Pumped Sections

Figure 5.1 shows a geological cross section A-A' constructed from logs of boreholes that approximately follow the river course between Waikerie SIS production bores 1 and 15 (the pumped survey stretch). Figure 5.2 shows the borehole locations and the path used to create this cross section. Between boreholes 10 and 15, the Glenforslan Formation appears to interrupt the Monoman Formation because the section crosses from flood plain to highlands in this area. The same location is significantly more resistive in the models than other sections of the survey (Figures 4.6 and 4.8), suggesting some relation between the Glenforslan Formation and resistive conditions. The river at this location is at the edge of the flood plain, and is therefore adjacent the Glenforslan according to the local geological section described in section 1.3.1 (Figure 1.5). However, where the river has been eroding into cliffs, the Glenforslan Formation may underlie the river sediments (depending on the shape of the river valley). Other areas where the river is at the edge of the flood plain and eroding cliffs do not show similar resistive features, suggesting that the observed resistivity change is not strictly geology controlled.

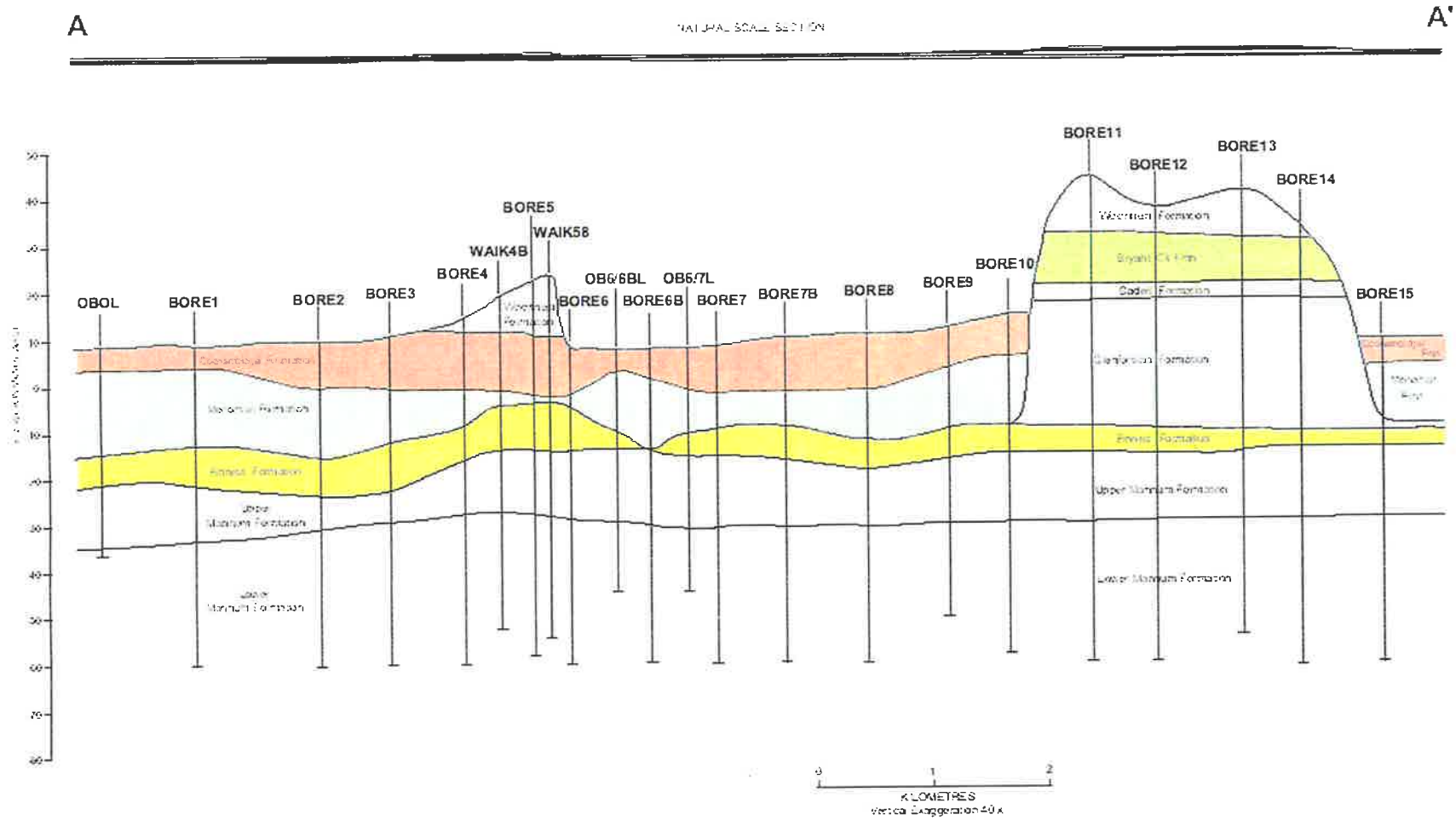

Figure 5.1: Geological cross section based on borehole logs. Bores 11 to 14 are not on the flood plain, and consequently encounter the Glenforslan Formation. Also, bore 6B encountered no Finniss Formation, which may allow more saline water accession. Cross-section provided by Australian Water Environments.

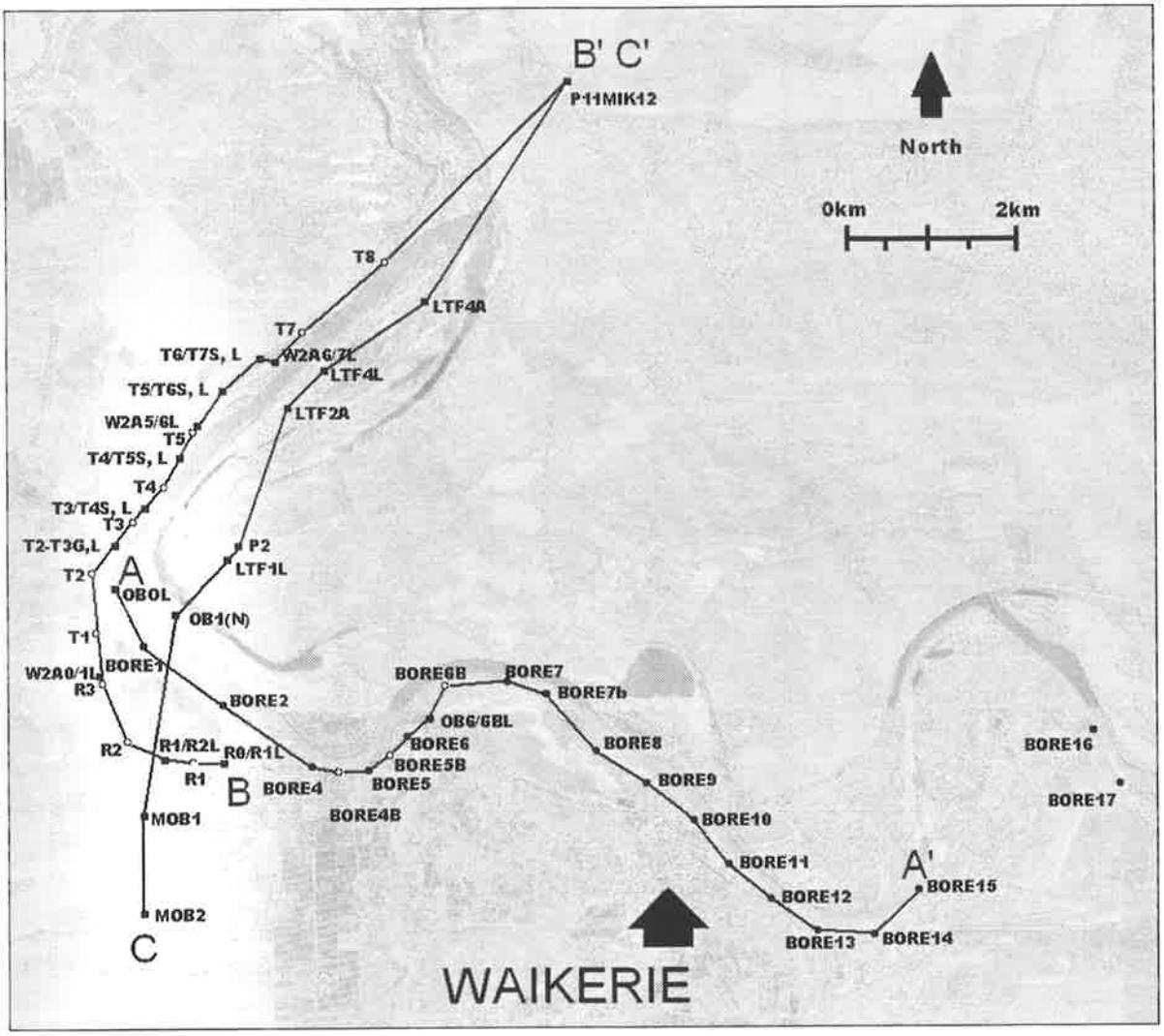

Figure 5.2: Borehole location map for cross sections A-A', B-B' and C-C'.

Given that a known geological variation (the occurrence of the Glenforslan Formation adjacent and possibly beneath the survey line) shows a correlation with a change in measured resistivity, it is important to determine whether hydrological variations are also being detected. Figures 4.14 and 4.15 show localised resistive anomalies around the Waikerie production bores 4, 6, 7 and 7B. This result agrees with expected hydrogeological response from pumping, as fresh river water replaces saline-water in the alluvium. Such anomalies are evidence that the surveys are responding to hydrology as much as (or more than) geology. Given that the Glenforslan was described as a considerably permeable formation (section 1.3.1), it is possible that the resistive section between production bores 10 and 15 is caused by a hydrological response to the described geological change: increased permeability of the Glenforslan acting as a conduit for the draw-down of fresh water during production bore pumping.

Variation in clay occurrence might also influence the measured resistivity of the sediments beneath the river. If clay-conduction is large enough (compared to non-clay sediments), conductive anomalies may be due to the occurrence of clay. However, clay layers have an important impact on the resistivity through another mechanism; low permeable clays act as aquitards and confining layers. Such hydrological control exhibited by clay may be more significant than clay-conduction if fluid conductivity is highly variable. An Induced Polarisation (IP) survey may be successful in identifying clay occurrence and could be run simultaneously with a DC Resistivity survey.

Major conductive anomaly A in the top 5m of alluvium in the pumped section of the survey (Figure 4.13) was midway between production bores 6 and 7. Production bore 6B, which had not commenced operation at the time of the survey, is located in the same region. A geological log from the drilling of production bore 6B revealed that the Finniss Formation was not present (see Figure 5.1), which has significant implications for the mechanism of Murray River salt-loads. The Finniss Formation is known to be a confining layer for the MGA, and consequently increased saline-water inflow should be anticipated where this confining layer is absent. Absence of the Finniss Formation at production bore 6B is evidence that the conductive anomaly is a salt-load hot-spot, and that hydrology is more important than clay-conduction in these models. Figure 4.15 shows that this conductive anomaly corresponds with a deep part of the river. Telfer (1989) calculated that groundwater discharge into rivers is 40-60% greater at trenches than elsewhere due to differences in hydrostatic pressures that occur in saline groundwater environments.

Other conductive anomalies that were identified as potential hot-spots are located between production bores 7 and 7B and between production bores 7B and 8 (Figure 4.11), which were smaller and less conductive than the anomaly between production bores 6 and 7. These have been labelled as minor potential hot-spots

Some production bores show little or no resistivity correlations (production bores 5, 8 and 9). Various mechanisms are proposed to explain this. Efficient pumping of the production bores may be enough to prevent saline water flowing into the river, but not enough to produce significant drawdown of fresh water, with the result that neither conductive nor resistive anomalies are seen; the permeability of aquitard units above the pumping depth may be low in these locations, preventing drawdown of fresh water into the sediments; and, near surface regions with high permeability may result in lateral fluid flow from

locations offset from the borehole location. Regardless of the mechanism involved, these production bores do not show conductive anomalies, and so are not described as inefficient in the Waikerie SIS. Indeed these production bores might be described as pumping at optimal efficiency, while others showing resistive features are described as over pumping.

Figure 5.3 shows contours of groundwater salinity, as measured in the marked boreholes. High resistivity sections from the TEM models (between production bores 10 and 15) correspond with Lower MGA salinity values less than 15,000 mg/L. Lower MGA groundwater salinity peaks at above 25,000 mg/L over the broad conductive region in the TEM data. The implication is that at depth (10 to 25m), the TEM modelled resistivities correlate with the spatial variation of groundwater salinity. Therefore, a conductive region of the model at depth does not immediately indicate higher salt-loads, but may indicate higher salinity groundwater. Instead, salt-load hot-spots are likely to occur at locations where the section is more conductive in the top 5m of alluvium (which may coincide with high groundwater salinity).

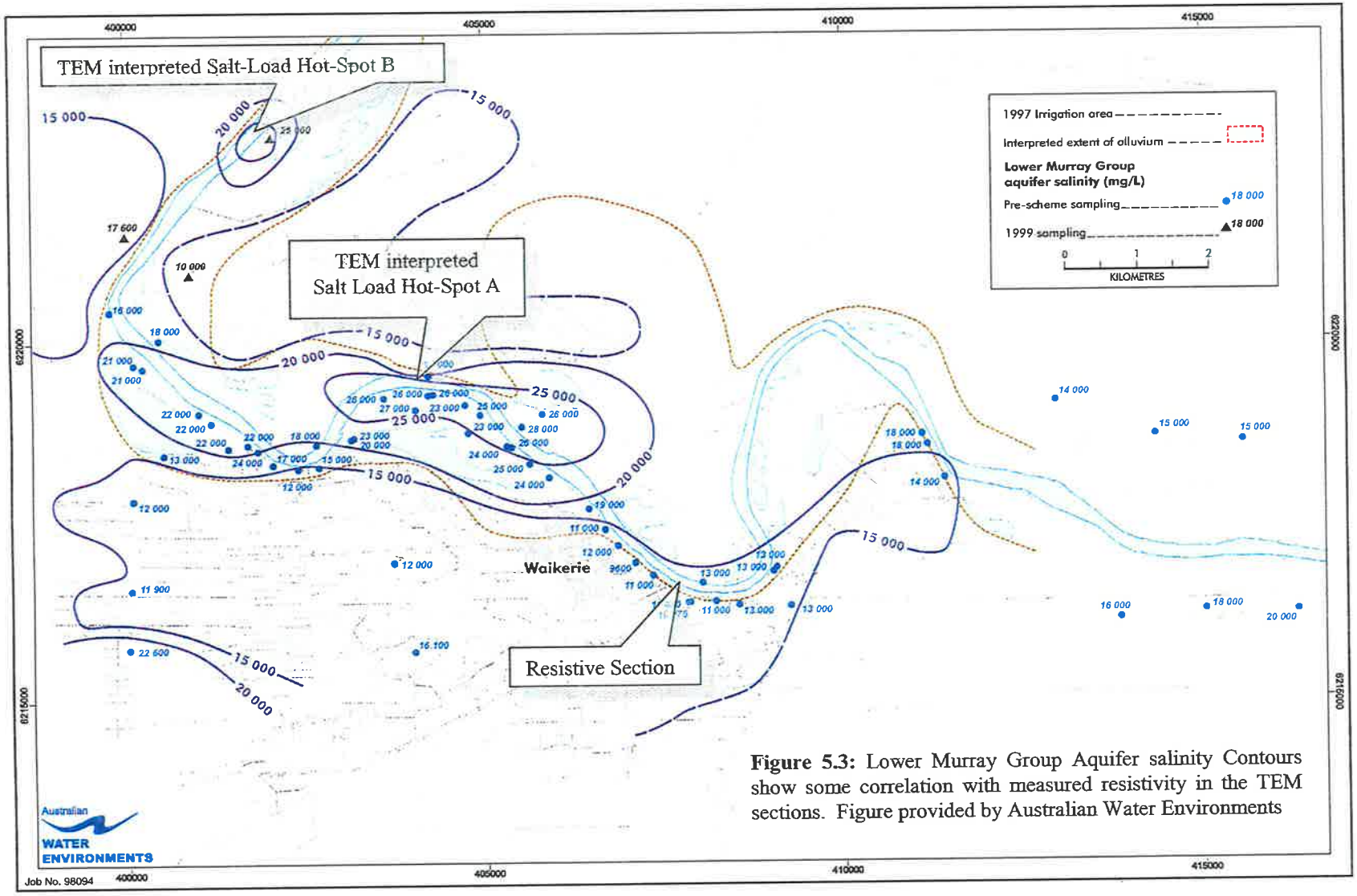

Figure 5.3: Lower Murray Group Aquifer salinity Contours show some correlation with measured resistivity in the TEM sections. Figure provided by Australian Water Environments

5.2.2 Unpumped Section

The purpose of the unpumped survey section was to compare observations with the pumped section and to identify salt-load hot-spots in a river section that has not been affected by SIS operation. Most of the unpumped survey line (Figure 3.4) lies at the edge of the flood plain. Consequently two geological cross sections are appropriate. Profile B-B' (Figure 5.4) was created from boreholes on the East of the survey (flood plain), while profile C-C' (Figure 5.5) was created from boreholes to the West of the survey line (highlands). See Figure 5.2 for cross section locations. There are no known significant geological changes along this section of the river, but the survey line is in close proximity to the Glenforslan Formation. The section is not as resistive as the region with similar geology in the pumped section (between production bores 10 and 15), but could become very resistive in response to pumping if the Glenforslan Formation acts as a permeable conduit for fresh-water drawdown.

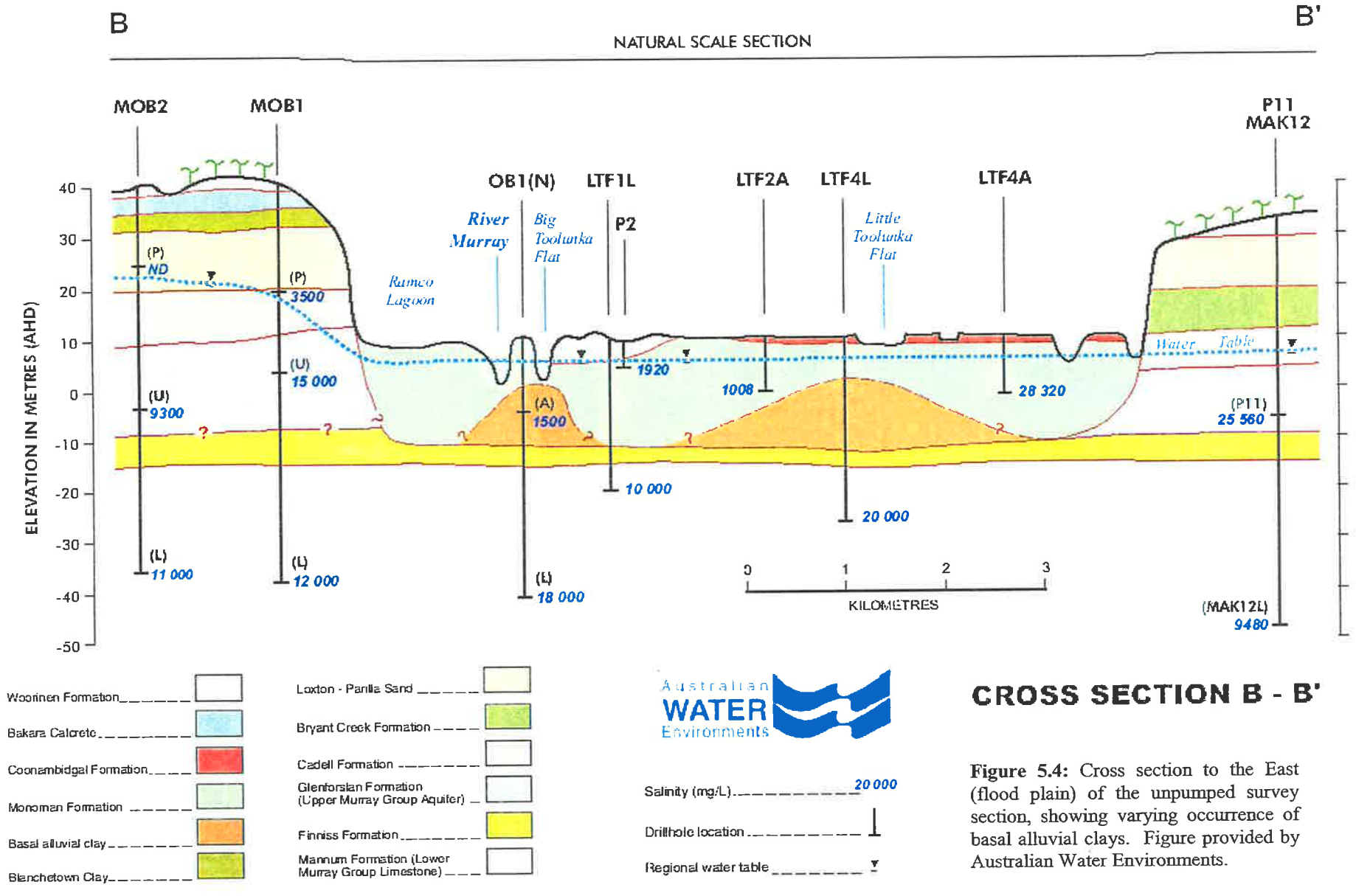

CROSS SECTION B - B'

Figure 5.4: Cross section to the East (flood plain) of the unpumped survey section, showing varying occurrence of basal alluvial clays. Figure provided by Australian Water Environments.

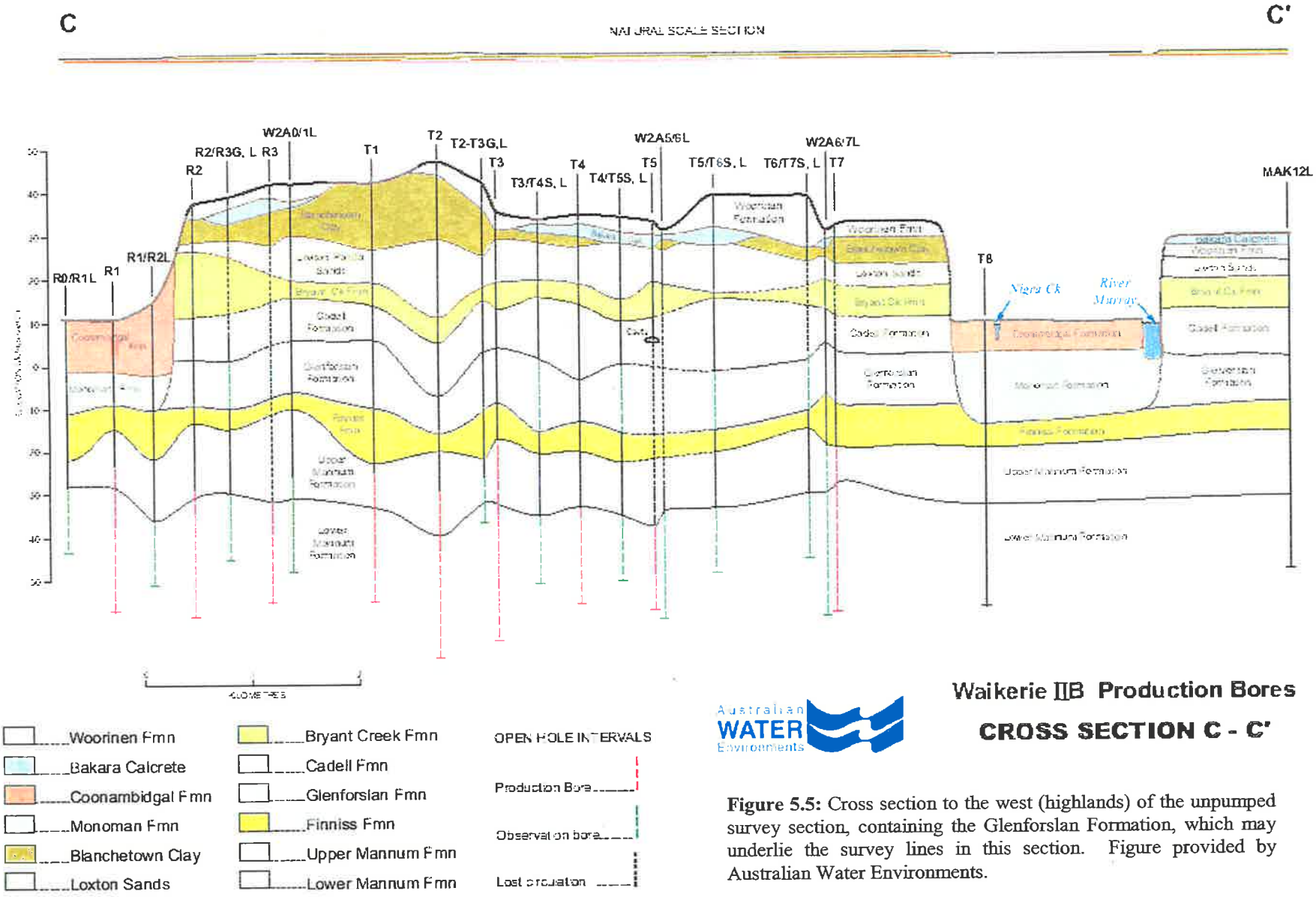

Australian WATER Environments

Waikerie IIB Production Bores

CROSS SECTION C - C'

Figure 5.5: Cross section to the west (highlands) of the unpumped survey section, containing the Glenforslan Formation, which may underlie the survey lines in this section. Figure provided by Australian Water Environments.

Figure 4.14 shows two interpreted major salt-load hot-spots (B and C), and two minor hot-spots (arrowed) in the unpumped survey section. Hot-spot B is a small feature, whereas hot-spot C is larger, extending over more than a kilometre, and occurring on both sides of the river.

Run-of-river surveys detect salt-loads down stream of the location of the source because denser saline water can remain at depth until river bends and/or changes in depth force mixing to occur (Telfer, 1989). Consequently, hot-spot B is considered a major source of saline water accession because it lies about 1 or 2 km upstream of a peak in river salt-load, as indicated by run-of-river surveys. Hot-spot C is also one or two kilometres upstream of a run-of-river determined salt-load peak. Figure 5.6 shows run-of-river salt-load data (as shown in Figure 1.7) with interpreted major salt-load hot-spot locations marked.

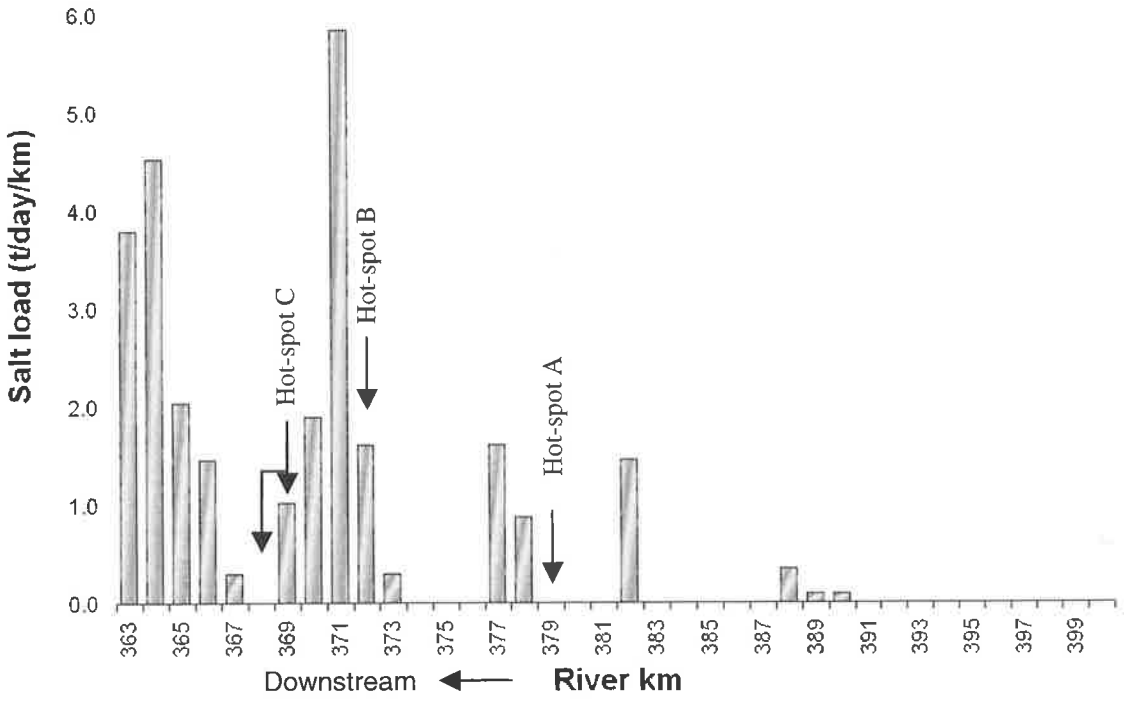

Figure 5.6: Salt-load Hot-spots as determined by run-of-river data with locations of TEM determined hot-spots indicated with arrows. Run-of-river salt-loads are consistently down stream of the hot-spots identified in the TEM data.

5.2.3 Archie's Law Analysis of Results

Archie's Law was introduced in Chapter 2 as a useful method for estimating fluid resistivity (and hence salinity) from the measured bulk resistivity and an estimate of porosity. The equation (2.4) neglects clay conduction, which must be considered as a possible contributor to the resistivity in the recorded data. Below is a list of significant resistivity features from the models presented in this study, with an Archie's Law assessment of fluid conductivity (assuming 55% porosity). For each situation, the impact of clay conduction would be that the fluid resistivity is higher than the following estimates.

Major hot-spots (1 ohm.m): For 1 ohm.m bulk resistivity, fluid resistivity is approximately 0.3 ohm.m (18,200 mg/L TDS). This is consistent with aquifer salinity contours between 15,000 and 30,000 mg/L in the region.

Deep conductive features (0.5 ohm.m): For 0.5 ohm.m bulk resistivity, fluid resistivity is approximately 0.15 ohm.m (36,400 mg/L TDS). This is slightly more conductive than the maximum aquifer salinity in the area, suggesting clay conduction may be affecting the resistivity pattern. Furthermore, as porosity at this depth might be slightly less than at the surface, calculated fluid salinity could be considerably higher than this estimate.

Background resistivity - Between hot-spots and resistive anomalies (5 ohm.m): Five ohm.m could correspond to 1.5 ohm.m (3,600 mg/L TDS) contained fluids. This is more saline than drinkable water, but is fresher than the regional aquifer.

Resistive anomalies at production bores (10 to 15 ohm.m): The resistive anomalies around some production bores could correspond to alluvium with 3 ohm.m to 4.5 ohm.m (1,800 mg/L to 1,200 mg/L TDS). These salinities are close to drinkable water quality.

Resistive section between production bores 10 and 15 (30-50 ohm.m): The resistive section corresponds to 9 ohm.m to 15 ohm.m (600 mg/L to 360 mg/L TDS). This is drinkable, and almost good drinking water (as defined in section 2.1). Recalling that clay conduction has been ignored, if any clay is present in the 30 to 50 ohm.m section between production bores 10 and 15, the water-salinity would be lower than this estimate.

Inversions discussed in Chapter 4 that included the early-time data produced more resistive, plan-view salt-load interpretations. The 30 ohm.m background resistivity could correspond to 9 ohm.m (600 mg/L TDS) fluids in the alluvium.

Inversions using STEMINV are likely to underestimate the resistivity in more resistive areas (Section 2.5.2). Consequently, true fluid salinities are probably lower than estimated in resistive areas. Salinities at resistive anomalies (e.g. at production bores) may be closer to river water salinity (330 mg/L TDS) than the estimated 1200 mg/L TDS.

5.3 Discussion of TEM Inversions

TEM data were inverted using the program STEMINV, which simultaneously minimises the difference between observed and calculated data (model-misfit), and model-roughness. In Chapter 2, STEMINV was used in a forward modelling study. The output of these models suggested the smoothness criterion is useful for preventing over-fitting of the model to the data, stabilising resistivity oscillations with depth. However, it also resulted in a broadening of observed resistivity changes.

Smooth models appear less complicated and are an aid to interpretation because trends are more quickly apparent. Occam's Razor states that "Where there are multiple solutions to a problem, the simplest solution is often the best". In this sense smooth TEM models are preferred over TEM models with no or minimal smoothing applied.

The resistivity of upper most river sediments was not as high as an Archie's Law calculation predicted. There are three possible explanations: the alluvial sediments have significant clay content which introduces clay conduction, making the unit more conductive than otherwise predicted; the sediments fluids are more saline than river water in most locations (see fluid salinity estimates in section 5.2.3); and the sediments are as resistive as original estimates, but their values are underestimated by the smooth modelling code (as predicted by forward models in Chapter 2).

Removal of the first three time windows from the TEM data was done because they did not appear to represent smooth decay. This was justified in Chapter 4 with a number of possible explanations for the behaviour of TEM fields in these early times. These included:

1. Assumption that displacement current (IP effect due to clay conduction) is negligible is inappropriate at early times because these are equivalent to sampling at high frequencies.

2. Current flow in the receiver is assumed to be uniform, but probably has high frequency (early-time) irregularities (noise).

3. The current turn-off ramp is assumed to be linear, but if the turn-off ramp takes a different form, the rate of current change (and hence the size of the magnetic field induced in the Earth) will not be constant.

4. The strength of the field in the early time may be sufficient to produce more current in the receiver than it is capable of measuring (over powering).

Discarding these early time windows means that the earliest data corresponds to signal penetration to approximately 11 m. Consequently, there is no TEM measurement of the resistivity of the river water. The models produced indicate a surface layer of approximately 10 ohm.m, which is more conductive than the known value (from hand held EC meter measurements of surface water). Both conductive-surface and resistive-surface models may fit the data equally well, but the inversion selects the more conductive model based on model smoothness. Parameter fixing should guide the inversion towards a model with the true surface value. However, parameter fixing did not lead to a stable inversion, suggesting that the early time errors discussed above are significant even in the 4th or 5th time window and perhaps cause a constant error in all windows.

5.4 Further work

Deciding on the relative significance of hydrology and geology in the measured resistivity structures is an essential part of interpretation. Permeability variations and variations in the occurrence of the basal alluvial clays and of the Finniss Formation (which act as low permeability barriers) were described as potential influences on hydrology. The occurrence of clay could also affect the measured resistivity through clay conduction, however the measurement of a conductive anomaly at Waikerie production bore 6B where no Finniss Formation was logged and the occurrence of resistive anomalies adjacent production bores suggests that hydrology is dominating the response.

Sediment sampling along a location with a near-surface conductive anomaly could provide a degree of ground truthing for the TEM technique. Measurement of porosity, bulk resistivity, fluid resistivity and clay content of collected samples would be required. Data acquired from such a sampling program could be compared to fluid salinity estimates made in this project using Archie's Law. Verification of the estimates would demonstrate that clay conduction is insignificant compared to hydrological variations, while if fluid salinity varies significantly from the estimates, a better understanding of the measured response could be gained from clay content variation.

Ground truthing could also be achieved with a follow up survey after production bore 6B of the Waikerie SIS commences pumping. If the described conductive anomaly (major salt-load A) is due to hydrology, then pumping from production bore 6B will reduce the size of the anomaly. This is considered the most important requirement for further development of the TEM technique for salt-load monitoring.

The resistive region between production bores 10 and 15 was explained by the occurrence of the Glenforslan Formation adjacent (and perhaps beneath) the Monoman Formation at the edge of the flood plain. The high resistivity is possibly due to the permeable Glenforslan enabling increased production bore draw-down. A TEM survey on the opposite side of the river (further from the production bores) might show less resistivity between production bore locations, which would be consistent with the proposed mechanism.

Finally, it was suggested in section 2.6 that the smoothing condition is more useful at depth, where it reduces over fitting of the data (stabilising oscillations with depth) and that sharp boundaries in the near surface (i.e. the water-sediment boundary) are more sharply defined in models with less smoothing applied. A useful improvement to current inversion techniques would be to utilise a variable smoothing function that allows models to vary more rapidly in the near surface than at depth.

5.5 Conclusions and Recommendations

This study has tested and compared two geophysical techniques for suitability as salt-load detection and monitoring tools on the Murray River. TEM and DC Resistivity both demonstrated the ability to image down to 25m depth, and were each capable of recording tens of kilometres of data per day with high spatial resolution. The TEM technique exhibited advantages over the DC Resistivity method (as discussed in section 5.1) and is the preferred and recommended method for future investigations. However, further development of the TEM array is required before it can be routinely employed as a monitoring technique.

Processing of the TEM data enabled the resistivity of the top 5m of river alluvium in parallel survey lines to be displayed in plan view, providing a map of potential salt-load hot-spots. By comparison with run-of-river salt-load estimates, conductive anomalies were labelled as major or minor salt-load locations.

A conductive anomaly exists between production bores 6 and 7, where an additional production bore (6B) will soon commence operation. The observations from this survey suggest that the location of production bore 6B is appropriate and is likely to result in the reduction of Murray River salt-loads. A follow up TEM survey is recommended to verify this prediction.

Finally, it is suggested that production bores 11 to 14 are operating beyond optimal efficiency, as they coincide with a considerably resistive region. Estimated fluid salinity in this location is approximately 600 mg/L TDS. If the section contains conductive clays, then contained fluid would probably be less saline than this. The volumes of water being pumped by these production bores could potentially be reduced, without introducing significant salt-loads.

APPENDIX A

A.1 Three Dimensional Figure Construction

The program Oasis Montaj (Geosoft Corporation) enables three dimensional presentations of geophysical sections that follow irregular paths. The process for creating such grids is described here.

Initially, it is necessary to consider each survey line as "mostly east-west" or "mostly north-south". For mostly east-west survey lines, the program's coordinate system must be set such that model Easting corresponds to the X-axis and model depth corresponds to the Y-axis. Next two grids are created: a grid of resistivity (e.g. Figure A1) and a grid of the model's northing channel. To display the resistivity grid in three dimensions, the northing grid is set as topography, or relief for the resistivity grid (Figure A.2) The axes are subsequently rotated to give the three dimensional presentation (Figure A.3).

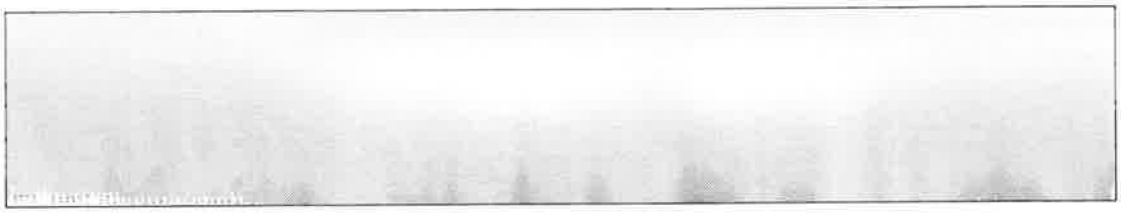

Figure A.1: An example grid of resistivity, with Easting as the x-axis and depth as the North axis. For three dimensional presentations, a similar grid of the northing channel is created

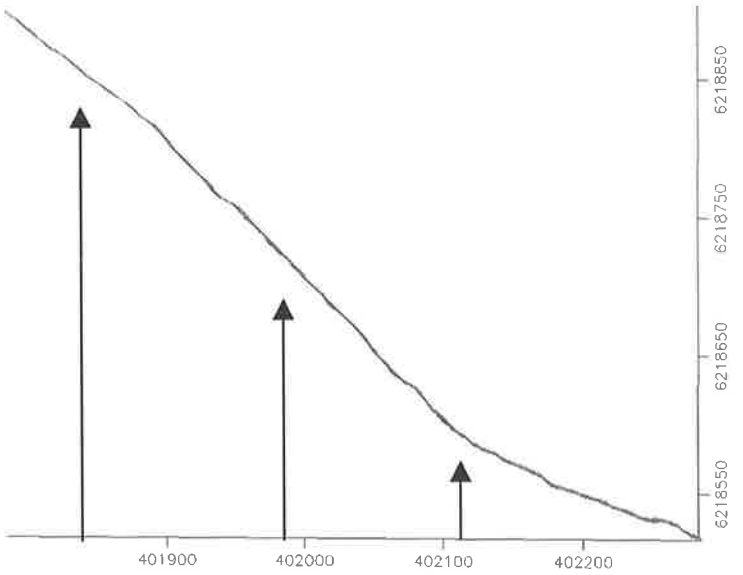

Figure A.2: The Northing Grid is used to define the relief (or topography) of the resistivity grid.

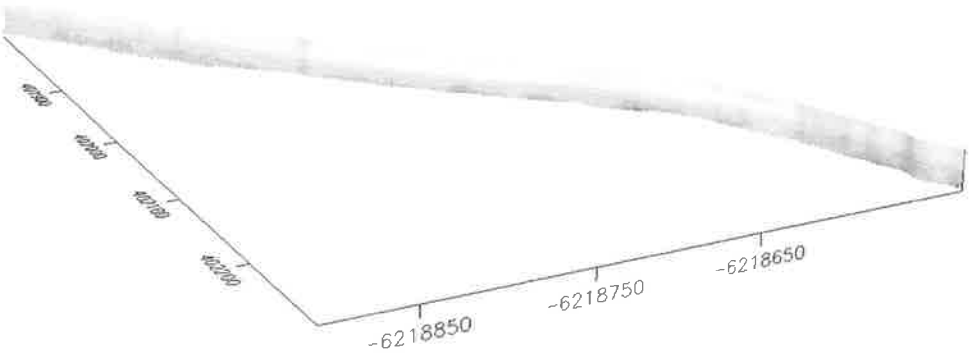

Figure A.3: After rotating the axis, the three dimensional model profile is displayed and can be viewed from different angles.

Slightly different steps are required for mostly north-south survey lines: the model depth should correspond to the program's X-axis and the model Northing should correspond to the Y-axis; instead of creating a grid of northing, a grid of easting is created; and the rotation of the axis is in a different direction.

A.2 Isolation of Upper Five Metres of Alluvium

Isolation of the top five metres of alluvial sediments required an accurate knowledge of river depth. A Fortran code was written to interpolate depth measurements to each model station, and alter the depth of each station so that the riverbed was at zero metres elevation. This enabled the top five metres of alluvium to be isolated.

The code obtains GPS data, depth measurements and the STEMINV model, each of which contain a time field. It first samples the GPS data and assign a GPS location to each depth reading. It then interpolates the depth readings to the model station locations. Depth interpolation is achieved by finding the two closest depth readings for each model station and calculating a weighted average of these two depths. The weights used in the average are the inverse of the squared separation of the station from the depth readings;

$$D_{\text{model station}} = \frac{\left(\frac{1}{R_1}\right)}{\left(\frac{1}{R_1}+\frac{1}{R_2}\right)} D_1 + \frac{\left(\frac{1}{R_2}\right)}{\left(\frac{1}{R_1}+\frac{1}{R_2}\right)} D_2 = \frac{R_2}{R_1+R_2} D_1 + \frac{R1}{R_1+R_2} D_2 \qquad (4.1)$$

where D_1 is the depth at the nearest depth measurement, D_2 is the depth at the second closest depth measurement and R_1 and R_2 are the square of the respective distances between model station and depth measurement location. In this way the profile of the final model is more smoothly varying than if a linear interpolation was used between depth measurements.

Having interpolated depth for each station the code outputs a modified version of the original model, where each station has been shifted vertically by the interpolated depth such that the riverbed is at 0 m everywhere (Figure A.4). Isolation of the upper most alluvium then involves removing all data from depths greater than (the new) 0 m and deeper than (the new) 5 m.

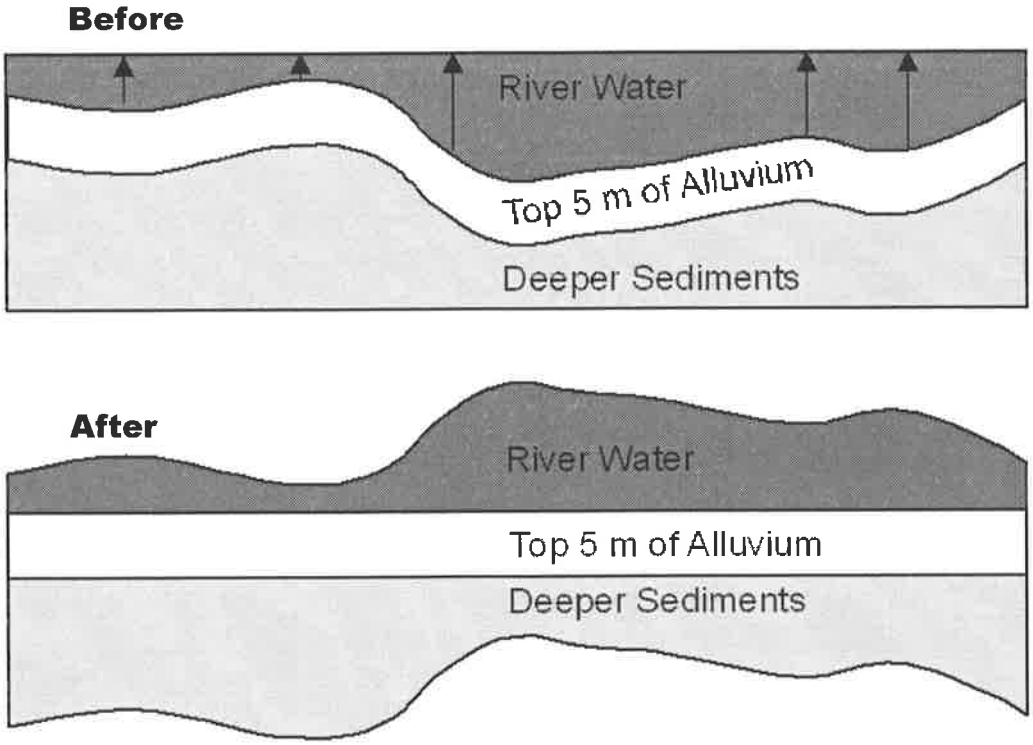

Figure A.4: Top five metres of alluvium were isolated from the data by changing the depth of each station so that the river bed is at zero metres. This figure shows the model section before and after the alteration.

A.2.1 – Fortran Code

```
      program flatsmod

C     this program merges time stamed depth measurements with time stamped GPS data, then finds
C     an appropriate depth (by applying a weighted average of the two nearest depth measuerments) to
C     each station GPS positions. The averaged depth is then use to shift all model cells in the Z
C     direction, giving a "flat river bed" model.

C--------define parameters
      REAL mdepth(500),gpseas(2000),gpsnor(2000),stn(1000),
     +snorth(1000),Zinv(1000),ResInv(1000),Res0(1000),Rerr0(1000),
     +dzW(1000),Rerr(1000),Rsns(1000)
      REAL diff,gap,deast(500),dnorth(500),seast(1000),
     +gap1(1000),gap2(1000),W1(1000),W2(1000),Zinvnw(1000),
     +depth(1000)
      REAL temp,dtime(500),gtime(2000)
      character*100 head1,head2
      integer nd,ng,nm,j1(1000),j2(1000),k

C------------read in data files----------------------------------------
      open(10,file='depth.dat',status='old')
      open(11,file='gps.dat',status='old')
      open(12,file='model.m1d',status='unknown')
C--read headers from model.m1d
```

```
      read(12,'(A100)') head1
      read(12,'(A100)') head2

C--read upto 500 lines from depth.dat
      do 10 i=1,500
      read(10,'(2F)',end=110) dtime(i),mdepth(i)
C--count number of lines as file is read (store as "nd")
      nd=i
   10 enddo
  110 continue
      close(10)

C--read upto 2000 lines from gps.dat
      do 11 i=1,2000
      read(11,'(3F)',end=11) gpseas(i),gpsnor(i),gtime(i)
C--count number of lines as file is read (store as "ng")
      ng=i
   11 enddo
      close(11)

      open(25,file='depthgps.dat',status='unknown')
      open(13,file='outmodel.m1d',status='unknown')
      write(13,'(A100)') head1
      write(13,'(A100)') head2

      k=0
   25 k=k+1
      do 13 i=1,1000

      read (12,'(4F,2E,4F)',end=113)stn(i),seast(i),snorth(i),Zinv(i),
     +ResInv(i),Res0(i),Rerr0(i),dzW(i),Rerr(i),Rsns(i)
C--count number of lines as file is read (store as "nm")
      nm=i
   13 enddo
  113 if (nm.lt.1000) k=25
      continue

C--------------------operate on data-----------------------------------
C------------find closest gpstime for each depth time--------------------
      do 14 i=1,nd       !ie for each depth reading

        diff=0.0003      ! 0.0003 is 26 sec.there should be a gps point
                         ! closer than this for each depth reading

        do 15 j=1,ng     ! ie search every gps reading

        temp=abs(dtime(i)-gtime(j))    ! difference between gpstime and depth time

        if ((temp-diff).lt.0.0) then   ! update diff if temp is smaller
          diff=temp                    ! thus closest gps time is found
          deast(i)=gpseas(j)           ! for each depth reading
          dnorth(i)=gpsnor(j)          ! closest gps easting and northing
                                       ! stored for as easting and northing for depth reading
        endif
   15 continue
   14 continue

C-----------find closest depth reading for each data stn----------------
      do 16 i=1,nm       ! for each model line
        gap=90000.       ! gap is a test paramater
```

```
      gap1(i)=1000.       ! if no close depth reading is found, setting gap1
      gap2(i)=1000.       ! and gap2 to zero ensures no change is made to model

      do 17 j=1,nd     ! search through each depth reading (with new east and north)
      temp=(deast(j)-seast(i))**2+(dnorth(j)-snorth(i))**2 !square of dist between depth reading
                                                           ! location and model station location
      if ((temp-gap).lt.0.0) then   !update gap if temp is smaller
      gap=temp                  !thus closest depth reading found for each model station
      j1(i)=j                 !store j (the line number in depth file)
      gap1(i)=gap               !store gap so waiting can be applied later
      endif
   17 continue

C-----------find second closest depth reading for each data stn---------
      gap=90000.
      do 18 j=1,nd     ! search through each depth reading (with new east and north)

      if (j.eq.j1(i)) goto 19       !dont test j1 (closest depth reading) so only second closest is found
      temp=(deast(j)-seast(i))**2+(dnorth(j)-snorth(i))**2     !square of dist between depth reading
                                                               ! location and model station location
      if ((temp-gap).lt.0.0) then
      gap=temp
      j2(i)=j
      gap2(i)=gap
      endif
   19 continue
   18 continue
   16 continue

C--------------calculate weights and estimate depth for each station----
     !new depth for model will be a weighted sum of two closest depth readings
     do 20 i=1,nm     ! for each model line
     if (gap1(i).ne.0) then
     W1(i)=1/gap1(i)/(1/gap1(i)+1/gap2(i))       !Weighting proportional to inverse of distance squared
                                                 !(normalised by total of all weights)
     else
     W1(i)=0                                !weight is zero if gap1 is zero (therefore no change to model)
     endif

c    if (gap2(i).ne.0) then
     W2(i)=1/gap2(i)/(1/gap1(i)+1/gap2(i))       !Weighting proportional to inverse of distance squared
                                                  !(normalised by total of all weights)
c    else
c    W2(i)=0 !weight is zero if gap1 is zero (therefore no change to model)
c    endif

     depth(i)=W1(i)*mdepth(j1(i))+W2(i)*mdepth(j2(i))    !new depth
     Zinvnw(i)=Zinv(i)+depth(i)                          ! adjusts model cell depths by river depth.
                                                        ! now all river bottom locations align with "0.0"
     write(25,'(4F)') stn(i),seast(i),snorth(i),-1*depth(i)
     write(13,100)stn(i),seast(i),snorth(i),Zinvnw(i),ResInv(i),
    +Res0(i),Rerr0(i),dzW(i),Rerr(i),Rsns(i)
   20 enddo
C-----------write new model file-----------------------------------
     if (k.le.24) goto 25                  ! loop until whole model complete
   100 format(4F,2E,4F)
   999 stop
     end
```

References

Allen, D. and Merrick, N., 2003. A floating electrode array for continuous geoelectrical imaging: Abstract in the 16th Geophysical Conference and Exhibition, Australian Society of Exploration Geophysics, Adelaide February 2003. *In* Preview, 102, 81.

Apparao, A., 1991. Geoelectric profiling: Geoexploration, 27, 351-389.

Archie, G.E., 1942. The electrical resistivity log as an aid in determining some reservoir characteristics: Translations of American Institute of Mineral and Metallurgy, 146, 54-62.

Barrett, B., Heinson, G., Hatch, M. and Telfer, A., 2002. Geophysical methods in saline groundwater studies: locating perched water tables and fresh-water lenses: Exploration Geophysics, 33, 115-121.

Bouwer, H., 1978. Groundwater Hydrology: McGraw-Hill Book Company, 480p.

Brown, C.M., 1989. Structural and stratigraphic framework of groundwater occurrence and surface discharge in the Murray Basin, southeastern Australia: BMR Journal of Australian Geology and Geophysics, 11, 127-146.

Brown, C.M. and Radke, B.M., 1989. Stratigraphy and sedimentology of the mid-Tertiary permeability barriers in the subsurface of the Murray Basin, southeastern Australia: BMR Journal of Australian Geology and Geophysics, 11, 367-385.

Brown, C.M. and Stephenson, A.E., 1991. Geology of the Murray Basin, southeastern Australia: Bureau of Mineral Resources Bulletin, 235, 430p.

Carter, A.N., 1985. A model for depositional sequences in the Late Tertiary of southeastern Australia. *In* Lindsay, J.M. (editor), Stratigraphy, palaeontology, malacology: papers in honour of Dr Nell Ludbrook: South Australian Department of Mines and Energy, Special Publication Series, 5, 13-28.

Edwards, L.S., 1977. A modified pseudosection for resistivity and IP: Geophysics, 42, 1020-1036.

Evans, R.S., 1989. Saline water disposal options: BMR Journal of Australian Geology and Geophysics, 11, 167-186.

Evans, W.R. and Kellet, J.R., 1989. The hydrogeology of the Murray Basin, southeastern Australia: BMR Journal of Australian Geology and Geophysics, 11, 147-166.

Giles, S.D., 1972. Stratigraphic investigations of the Tertiary sequences, western Murray Basin, South Australia: Honours thesis, University of Adelaide, Department of Geology and Geophysics, Adelaide (unpublished).

Griffiths, D.J., 1999. Introduction to Electrodynamics: Prentice Hall International Inc.

Hatch, M., Barrett, B., Bennetts, D., Heinson, G., Telfer, A. and Roberts, C., 2002. Improved near surface mapping in groundwater studies: application of fast-sampling time-domain EM surveying methods: Preview, 96, 25-29.

Hohmann, G.W. and Raiche, A.P., 1988. Inversion of controlled-source electromagnetic data. *In* Nabighian, M.N. (editor), Electromagnetic methods in applied geophysics, 1: Society of Exploration Geophysicists, 131-311.

Jones, B.F., Hanor, J.S. and Evans, W.R., 1994. Sources of dissolved salts in the central Murray Basin, Australia: Chemical Geology, 111, 135-154.

Jupp, D.L.B. and Vozoff, K., 1975. Stable iterative methods for the inversion of geophysical data: Geophysical Journal of the Royal Astronomical Society, 42, 957-976.

Kearey, P. and Brooks, M., 1991. An introduction to geophysical exploration: Blackwell Science.

Keller, G.V. and Frischknecht, F.C., 1966. Electrical methods in Geophysical Prospecting: Pergamon Press Inc.

Kellet, J.R., 1989. The Ivanhoe Block – its structure, hydrogeology and effect on groundwaters of the Riverine Plain of New South Wales: BMR Journal of Australian Geology and Geophysics, 11, 333-354.

Klingner, D.M., 2000. Palaeoenvironmental Reconstruction of Ancient Lake Bungunnia, Murray Basin, Australia: Honours thesis, University of Adelaide, Department of Geology and Geophysics, Adelaide (unpublished).

Knight, J.H. and Raiche, A.P., 1982. Transient electromagnetic calculations using the Gaver-Stehfest inverse Laplace transform method: Geophysics, 47, 47-50.

Lindsay, J.M. and Barnett, S.R., 1989. Aspects of stratigraphy and structure in relation to the Woolpunda Groundwater Interception Scheme, Murray Basin, South Australia: BMR Journal of Australian Geology and Geophysics, 11, 219-226.

Longuet-Higgins, M.S., Stern, M.E. and Stommel, H., 1954. The electric field induced by ocean current and waves, with applications to the method of towed electrodes: Papers in Physical Oceanography and Meteorology, 13, 1-37.

Ludbrook, N.H., 1957. A reference column for the Tertiary sediments of the South Ausralian portion of the Murray Basin: Royal Society of New South Wales, Journal and Proceedings, 90, 174-180.

Ludbrook, N.H., 1961. Stratigraphy of the Murray Basin in South Australia: Geological Survey of South Australia, Bulletin, 36.

Lukasik, J.J. and James, N.P., 1998. Lithostratigraphic revision and correlation of the Oligo-Miocene Murray Supergroup, western Murray Basin, South Australia: Australian Journal of Earth Sciences, 45, 889-902.

McGowran, B., Li, Q. and Moss, G., 1997. The Cenozoic neritic record in southern Australia: the biogeohistorical framework: SEPM special publication, 56.

MacInnes, S. and Raymond, M., 2001a. STEMINV Documentation - Smooth-Model TEM Inversion, version 3.00: Zonge Engineering and Research Organisation Inc.

MacInnes, S. and Raymond, M., 2001b. TS2DIP Documentation - Smooth-Model Resistivity and IP Inversion with topography: Zonge Engineering and Research Organisation Inc.

Macphail, M.K. and Truswell, E.M., 1989. Palynostratigraphy of the central west Murray Basin: BMR Journal of Australian Geology and Geophysics, 11, 301-332.

Merrick, N.P., 1997. A new resolution index for resistivity electrode arrays: Exploration geophysics, 28, 106-109.

Nabighian, M.N. and Macnae, J.C., 1991. Time domain electromagnetic prospecting methods. *In* Nabighian, M.N. (editor), Electromagnetic Methods in Applied Geophysics, Vol. 2A. Tulsa: Society of Exploration Geophysicists, 427-520.

NAP, 2003. National Action Plan for Salinity and Water Quality. <URL:http://www.napswq.gov.au/>

Porter, B., 1997. Run of river salinity surveys – data collection and calculations results and recommendations: Department for Environment, Heritage and Aboriginal Affairs, Natural Resources Division, Murraylands Region, Water Resources report 2/97.

Raiche, A.P., 1984. The effect of ramp function turnoff on the TEM response of a layered ground: Exploration Geophysics, 15, 37-41.

Raiche, A.P., Jupp, D.L.B., Rutter, H. and Vozoff, K., 1985. The joint use of coincident loop transient electromagnetic and Schlumberger sounding to resolve layered structures: Geophysics, 50, 1618-1627.

Reynolds, J.M., 1997. An introduction to applied and environmental geophysics: John Wiley & Sons Ltd.

Roy, A. and Apparao, A., 1971. Depth of investigation in direct current methods: Geophysics, Vol 36, No. 5, 943-959.

Sandburg, S.K., 1990. Microcomputer software for individual or simultaneous inverse modelling of transient electromagnetic, resistivity and induced polarization soundings: New Jersey Geological Survey Open-File Report, OFR 90-1.

Smith, R. and Pain, J., 1999. Three-dimensional transient electromagnetic modelling – A user's view. *In* Oristaglio, M., and Spies, B. (editors), Three-Dimensional Electromagnetics: Australian Society of Exploration Geophysicists, Geophysical Developments No.7.

Snyder, D.D., MacInnes, S.C., Raymond, M.J. and Zonge, K.L., 2002. Continuous resistivity profiling in shallow marine and fresh water environments: Zonge Engineering and Research Organisation, Tucson, Arizona (unpublished).

Stephenson, A.E., 1986. Lake Bungunnia; a Plio-Pleistocene megalake in southern Australia: Palaeogeography, Palaeoclimatology, Palaeoecology, 57 (4), 137-156.

Telfer, A., 1989. Groundwater-riverwater density contrasts: its effect on the pattern of groundwater discharge to the River Murray: BMR Journal of Australian Geology & Geophysics, 11, 227-232.

Telfer, A., Hyde, K. and Schultz, G., 2000. Assessment of Freshwater Lenses in the Vicinity of Stockyard Plains Disposal Basin: SA Water and Australian Water Environments internal report.

Telfer, A. and Watkins, N., 1991. Waikerie Salt Interception Scheme – final design report hydrogeology: Engineering and Water Supply (EWS) Department.

Telfer, A. and Way, D., 2000. Waikerie and Woolpunda Salt Interception Schemes - performance review using in stream data: SA Water and Australian Water Environments internal report.

Telford, W.M., Geldart, L.P. and Sheriff, R.E., 1990. Applied Geophysics 2nd edn. Cambridge: Cambridge University Press.

Vivian, N., Herbert, T., Porter, B. and Couch, S., 1998. Changes in salinity, salinity accessions and salt load accessions in the River Murray in South Australia: Department for Environment, Heritage and Aboriginal Affairs Environment Protection Agency, Murraylands Region, Berri, report 10/98.

Wall, M., 2001. Murray Basin stratigraphy and its relevance to the Waikerie Salt Interception Scheme, Waikerie, South Australia: Honours thesis, University of Adelaide, Department of Geology and Geophysics, Adelaide (unpublished).

Ward, S.H. and Hohmann, W.G., 1988. Electromagnetic theory for geophysical applications. *In* Nabighian, M.N. (editor), Electromagnetic methods in applied geophysics, vol 1: Society of Exploration Geophysicists, 131-311.

White, G., 2000. Geomorphology and origin of sediments of the freshwater palaeolake - Lake Bungunnia, Murray Basin: Environmental, hydrogeological and agricultural implications. Honours thesis, University of Adelaide, Department of Geology and Geophysics, Adelaide (unpublished).

Zhou, B. and Greenhalgh, S.A., 2001. Rapid 2D/3D crosshole resistivity imaging with the analytic sensitivity function: Geophysics, 67, 755-765.

Zonge, K.L., 1992. Introduction to TEM: Zonge Engineering and Research Organisation, Extracted from Practical Geophysics II, Northwest Mining Association.